FACULTY OF SCIENCE
UNIVERSITY OF COPENHAGEN

PhD thesis
Jesper Sjolte

Modeling of present and Eemian stable water isotopes in precipitation

Supervisors:
Sigfús J. Johnsen
Centre for Ice and Climate, Niels Bohr Institute
University of Copenhagen

Georg Hoffmann
Laboratoire des Science du Climat et de l'Environnement
CEA-CNRS-UVSQ-IPSL, Saclay

Submitted: November 30, 2009

Abstract

Two modeling studies were carried out. One using the regional climate model REMO_{iso}, and one using the global climate model ECHAM_{iso}. In the regional study REMO_{iso} was forced with reanalysis data for the period 1959 to 2001 using a domain including Greenland and the surrounding North Atlantic. The model was found to reproduce the observed seasonal variability of temperature and precipitation well. For central Greenland a temperature bias of $+5^oC$ was found, which was most likely caused by a too low surface albedo and the parametrization of the atmospheric boundary layer. A positive bias for central Greenland was also found in the δ^{18}O. This is attributed to the aforementioned temperature bias and an underestimation of vapor transport to cold regions. In comparison with ice core data and observations from coastal stations the model reproduced a significant part of the winter δ^{18}O variability from most sites. A significant impact of the NAO on the main mode of variability of temperature, δ^{18}O and precipitation was found in agreement with ice core data and observations. For inland Greenland the modeled deuterium excess level is overestimated, particularly during winter. This is probably related to the parametrization of the cloud supersaturation during snow formation. For coastal areas the annual cycle of deuterium excess was captured by the model. The global climate model ECHAM_{iso} was used for three time slice experiments for the Eemian interglacial. Present day boundary conditions were used except for the insolation and the SST patterns. The modeled summer temperatures for the Northern Hemisphere were found to match proxy data well, with the large summer insolation anomalies causing warmer summers than present day. The peak summer anomalies are $+6^oC$ for central Greenland. However, the temperature anomalies are considerably lower and only marginally significant in Antarctica. The modeled δ^{18}O for Greenland follows the tendency of the ice core data in the different time slices, but with underestimated amplitude. For Antarctica the modeled isotopes do not agree with ice core data. The discrepancy between the model output and the ice core data is attributed to the boundary conditions, where ice sheet dynamics and vegetation feedbacks have not been accounted for.

Resumé

To modellerings studier er blevet udført. Et med den regionale klimamodel REMO_{iso} og et med den globale klimamodel ECHAM_{iso}. I det regionale studie blev REMO_{iso} drevet af reanalysedata i perioden 1959 til 2001 for et område indeholdende Grønland og det omkringliggende Nordatlanten. Den observerede sæsonmæssige variabilitet for temperatur og nedbør blev reproduceret på tilfredstillende vis af modellen. For central Grønland blev der fundet en positiv temperaturbias på $+5^oC$, sandsynligvis foresaget af en for lav overflade albedo og parametriseringen af det atmosfæriske grænselag. En positiv bias for central Grønland blev også fundet for δ^{18}O. Denne bias forklares ved den førnævte temperatur bias, samt en underestimering af transporten af vanddamp til kolde områder. Sammenlignet med iskernedata og kystobservationer reproducerer modellen en signifikant del af vintervariabiliteten i δ^{18}O for de fleste områder. I overensstemmmelse med iskernedata og observationer blev der identificeret et signifikant aftryk af den Nordatlantiske Oscillation i variabilitets mønstrene for temperatur, δ^{18}O og nedbør. For central Grønland er niveauet for deuterium excess overestimeret af modellen, specielt for vinterhalvåret. Dette er sandsynligvis relateret til parametriseringen af overmætningen i skyen under dannelsen af sne. For kystområder blev den årlige variation af deuterium excess reproduceret af modellen. Den globale model ECHAM_{iso} blev anvendt til tre experimenter for forskellige tidsperioder under mellemistiden Eem. Nutidige grænsebetingelser blev andvendt på nær havoverflade tempereture og solindstråling. Den modellerede sommertemperatur for den nordlige halvkugle stemmer overens med proxydata, hvor den højere sommer temperatur er foresaget af solindstrålings anomalier. Den maksimale sommer anomali er $+6^oC$ for central Grønland. For Antarktis er temperatur anomalierne væsentlig mindre og kun marginalt signifikante. Den modellerede δ^{18}O for Grønland følger tendensen fundet iskernedata for de forskellige tidsperioder, men med underestimeret amplitude. For Antarktis stemmer de modelerede isotoper ikke overens med iskernedata. Uoverenssemmelsen mellem model outputtet og iskerne data tillægges grænsebetingelserne, hvor der ikke er blevet taget højde for iskappe dynamik og

ændringer i vegetation.

Preface

This PhD project was carried out at the Centre for Ice and Climate (CIC), Niels Bohr Institute, University of Copenhagen and at the Laboratoire des Science du Climat et de l'Environnement (LSCE), CEA-CNRS-UVSQ-IPSL, Saclay, with about one year altogether being spent at the LSCE.
The principal supervisor of the project was Sigfús J. Johnsen of the CIC. All of the modeling work featured in this thesis was carried out at the LSCE in collaboration with my external supervisor Georg Hoffmann of the LSCE.

The project was funded by the Faculty of Science, University of Copenhagen, the Danish Council for Independent Research and the Commissariat à l'Énergie Atomique (CEA). All partners contributed to the project with about one third. The computing facility at Deutsches Klimarechenzentrum (DKRZ) was used for the modeling experiments.

Outline

The bulk of this thesis is based on two modeling studies, one using the regional climate model REMO$_{iso}$, and one using the global climate model ECHAM$_{iso}$.
In **Chapter 1** the motivation and aim of the thesis will be given, along with a general introduction to climate modeling with regional and global climate models. The modeling of stable water isotopes in the hydrologic cycle will also be introduced in this chapter.
Chapter 2 presents the results of the work with REMO$_{iso}$. The chapter has three main parts that deals with, validation of REMO$_{iso}$ for Greenland, the modeled and observed climate variability and the deuterium excess.
In **Chapter 3** a modeling study of the previous interglacial period, the Eemian, is presented. An introduction to the Eemian climate is given and the results of three time slice experiments are presented. In addition to the study of the Eemian polar climate an investigation of the monsoon is performed.
Chapter 4 summarizes the main conclusions and gives an outlook on future work. Additionally there are two appendices, where Appendix A is relevant

for Chapter 2 and Appendix B is relevant for Chapter 3.

Acknowledgements

First of all I would like to thank my supervisors. Sigfús was also the supervisor of my master's thesis and I have again had the privilege of benefiting from his wast knowledge and experience. Thanks to Georg for spending many hours introducing me to the world of climate modeling.
During my stay at the LSCE several people contributed to my PhD work, and I would like also to thank them. Special thanks should go to Valérie Masson-Delmotte for giving many helpful suggestions for the analysis of the model output, and for the detailed comments on the draft of this thesis.
Christophe Sturm, who implemented the isotopes in $REMO_{iso}$, has also been of great help during the course of my PhD, especially with respect the handling of $REMO_{iso}$ output.
Thanks should of course also go to the people of the CIC, especially Bo M. Vinther for providing the seasonal ice core and helping with the back-diffusion, as well as Asbjørn Persson and Hans Christian Steen-Larsen for interesting discussions and helpful comments on the thesis.
Last but not least thanks should go to my family and friends. This goes both to the new friends I met in France and to my old friends for being there when I came back.

Copenhagen, November 2009 Jesper Sjolte

Contents

Chapter 1

Introduction

In the early fifties W. Dansgaard discovered the relationship between the abundance of ^{18}O in precipitation and the cloud condensation temperature [Dansgaard, 1953]. With the drilling of the Camp Century ice core in the northwestern Greenland, Dansgaard saw the possibility of using the isotope thermometer in connection with palaeoclimate. This resulted in the first glacial climate record from an ice core [Dansgaard et al., 1968]. Since then, numerous ice cores have been drilled in both Greenland and Antarctica [Johnsen et al., 2001, Jouzel et al., 2007, Petit et al., 1999], providing invaluable knowledge about past climate changes and the nature of the climate system [Johnsen et al., 1992, Fischer et al., 1999, Blunier and Brook, 2001].
The aim of this PhD thesis is, by the means of models of the atmosphere, to further explore the climatic information that can be extracted from the stable water isotopes in precipitation. This is done in two different modeling studies, one for present day, and one palaeoclimatic.
The study for present day focuses on the Greenland climate of the last half of the twentieth century. A high resolution model with isotope diagnostics build into the hydrologic cycle, is used to reproduce the observed weather patterns. The idea is, that by making the model reproduce the actual weather patterns, the modeled isotopic signal can be directly compared to the signal recorded by observations and the Greenland ice cores. Thus enabling an evaluation of our current understanding of the processes governing the isotopic signal.
In the palaeoclimatic study experiments for three different periods during the Eemian interglacial are done with a global model, also fitted with isotope diagnostics. By comparing the model output to ice core data, and other proxy data, the exactness of the climate reconstruction can be evaluated. The warmest periods during the Eemian are believed to have been warmer than the present climate. During these warmer periods the Eemian can thereby be seen as an analogy for a possibly warmer future climate.

1.1 Numerical modeling of the climate

The complex climate models of today are often weather prediction models modified to work as climate models. This is in fact the case for both the General Circulation Model (GCM) ECHAM, and the Regional Climate Model (RCM) REMO, used in this PhD project. The ECHAM and the REMO model will be introduced in Section 1.2 and 1.3, respectively.
The first attempts to calculate changes in the weather was done by L.F. Richardson as described in his book *Weather Prediction by Numerical Process* [Richardson, 1922]. The labor of doing all of the numerical calculations by hand was enormous, and the results were not realistic. Due to high frequency gravity-waves in the initial field, Richardson got a pressure change that was two orders of magnitude too large [Lynch, 1992]. Further more, the time step Richardson had chosen for his calculation was too long. Had he continued the calculation for more than one time step, the solution would have been proved to be unstable. However, Richardson did not know the criteria of stability for finite difference schemes [Lynch, 1992]. Even with these shortcomings Richardson was ahead of his time. By dividing a limited domain of the surface of the Earth into grid boxes, and solving a set of differential equations numerically, Richardson basically did the same as is being done today by climate modelers and weather prediction services.
The revolution of numerical weather prediction did not happen until decades after Richardson's calculations, when the use of electronic computer power became available in the 1940's. In 1950 the first numerical weather prediction carried out using the ENIAC computer [Charney et al., 1950], and later that same decade the Institute of Meteorology at the University of Stockholm was carrying out routine forecasts using the BESK computer [Bergthorsson et al., 1955]. It should be mentioned that these forecasts were barotropic and the quality of the numerical predictions did not surpass the quality of traditional forecasts until later.
As mentioned above certain criteria for the temporal (and spatial) resolution exits for a numerical solution to be stable. The discretization of the continues fields required to perform the numerical solution allows for errors to build up if not a certain relationship between the temporal and spatial resolution is met. Depending on the integration scheme the exact form may vary, but the criterion can be summed up as this: if the temporal resolution is too large compared to the spatial resolution the solution will be unstable. A so called von Neumann analysis must be performed to know the stability criterion of a given integration scheme. This analysis is named after the mathematician John von Neumann, who was an important figure for the development of the field of numerical calculations. The method was first described in Crank and

Nicolson [1947] and Charney et al. [1950]. This limitation on the relation between the temporal and spatial resolution sets the demands on the computing power needed to perform weather forecasts and climate simulations. If higher spatial resolution is needed, the temporal resolution must be higher as well, further increasing the number of operations that must be done by the computer.
The quest for producing weather forecasts raised the question if the weather was indeed predictable. Lorenz was the one to discover the chaotic, or as he put it, nonperiodic, behavior of the solution of a set of relative simple differential equations [Lorenz, 1963]. The *Lorenz equations* are a linearized set of equations derived from a set of equations describing convection in the atmosphere. The work of Lorenz paved the way for our current understanding of the weather and the climate as a deterministic chaotic system.
In modern weather prediction [Buizza et al., 2007], and in predictions of the future climate [Solomon et al., 2007], ensemble forecasting is used, where multiple model runs using slightly different initial conditions are made. The exact initial state of the atmosphere is not known, and slight perturbations in the initial field will due to the chaotic nature of the system produce a diverging solution compared to an experiment with non-perturbed initial conditions. By producing multiple solutions a probability estimate of the range of the solution can be made.

1.1.1 The representation of the atmosphere in climate models

As mentioned above in connection with the work of Richardson the atmosphere in climate models are discretized into a latitudinal-longitudinal and vertical grid. At each node point the prognostic variables (temperature, pressure ect.) are calculated from the governing equations. However, since the resolution of the model grid is usually relative course (several hundreds of kilometers for global climate models) the processes in the atmosphere taking place on a sub-grid scale are approximated using so called parametrizations. Generally, the governing equations of a model are referred to as the dynamics, and the parametrizations as the physics of a model.
In the 1970's the spectral method was introduced for solving the governing equations [Gordon and Stern, 1982]. The spectral method differs from the gridded method in that the variable fields are transformed from the gridded representation to be represented by spherical harmonics, when solving the equations. The spectral method was introduced due to being more computational effective compared to the gridded representation. Since the horizontal

resolution of spectral models cannot be referred to directly as a latitudinal-longitudinal resolution, the wavenumber truncation is used instead. Spectral climate models are often used in a resolution of T42, meaning that the spherical harmonics are truncated at wavenumber 42 and the T refers to triangular truncation. The T42 resolution is equivalent to a grid resolution of $\sim 2.8^o$x2.8^o. Triangular truncation means that the truncation happens at the same wave number in the latitudinal and longitudinal direction, as opposed to rhomboidal truncation [Daley and Bourassa, 1978].
The vertical discretization is done by dividing the atmosphere into a number of layers. Since most of the dynamics of the atmosphere happened in the lower troposphere the resolution is finer near the bottom of the atmosphere than at the top. A common formulation of the vertical levels is the hybrid σ-pressure coordinate system, where the levels follow the terrain near the surface and gradually approach being pure pressure levels at the top of the atmosphere [Modellbetreuungsgruppe, 1993].

1.1.2 Regional models

Motivated by the possibility of locally increasing the spatial resolution regional models, or limited area models, were developed. Since it is very computationally demanding to increase the horizontal resolution globally, to say 0.5^o degrees, it is practical only to do it for a limited area. The nature of regional models of course dictates them to have limited coverage. Regional models must therefore always be coupled with lateral boundary conditions from for example either a global model or observations in form of a reanalysis field. In the case of the REMO regional model featured in this thesis, the lateral boundary conditions are passed on to the model using a relaxation scheme through an 8 grid box wide buffer zone [Davies, 1976].
The direct advantages of the higher spatial resolution is better representation of orographics, and therefore for example orographic forced precipitation, resolution of other regional sub-GCM scale features, but also circulation features such as the formation and life of synoptic systems are better calculated with a high resolution.
Regional models are setup using a rotated grid, such as for example the grid introduced by [Arakawa, 1997]. The grid is defined by choosing a rotated north pole, size of the domain and southwestern corner of the domain. Figure 1.1 shows an example of a rotated grid. A rotated grid has the property of having almost equal area for the grid boxes throughout the domain. Apart form this being convenient for analytical purposes, it also means that the model will have approximately the same numerical stability criteria all over the domain, as the relation between the spatial and temporal model resolu-

tion will be the same.
Similarly to the global models the spectral method has been applied in regional models [Juang and Kanamitsu, 1994]. However, the regional model featured in this thesis is of the grid box type.

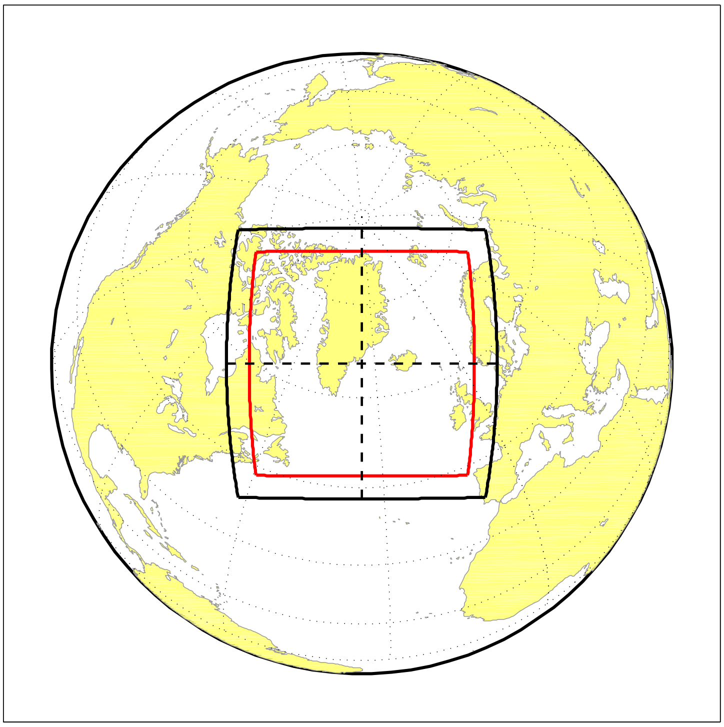

Figure 1.1: Illustration of the rotated grid used for the REMO$_{iso}$ regional model experiment presented in Section 2.1. The full black line marks the limits of the full domain, while the red line marks the domain excluding the 8 grid box buffer zone. Also shown is the rotated prime meridian and Equator (dashed lines), that both go through the center of the domain.

1.1.3 The nudging technique

When modeling tracers in the atmosphere with climate models it can be desirable to have the model follow actual weather patterns. If the model follows the weather in a given period the problem of validation will, in an ideal case, be isolated to the traces. A four-dimensional assimilation scheme was developed for validation purposes of ECHAM, where the prognostic variables vorticity, divergence, temperature, and surface pressure can be relaxed towards the observed fields [Jeuken et al., 1996]. The relaxation (*Newtonian relaxation*) is done by adding a small increment to models own tendency so that the model is forced towards the observed field. Equation 1.1 describes the overall tendency of a prognostic variable x, which is relaxed towards the observed field

$$\frac{dx}{dt} = F_m(x) + G(x)(x_{obs} - x) \tag{1.1}$$

where $F_m(x)$ is the tendency calculated by the model, $G(x)$ is the relaxation coefficient $[s^{-1}]$ and $(x_{obs} - x)$ is difference between the modeled and observed value of x. This technique is called nudging. In order not to cause physical inconsistency in the model, the increment added to the model tendency is always significantly smaller than the tendency itself. Apart from nudging in connection with isotopic tracers, as in this thesis, the method has be applied in a study of methane and hydrogen fluoride done by van Aalst et al. [2004]. A similar technique has been developed for regional models. However, the nudging of regional models are done somewhat differently than for global models in order to take advantage of the high resolution of the regional models. This is called spectral nudging, where the model is only nudged to the large scale features of the observed field [Waldron et al., 1996]. Further more can a height dependence be build into the nudging, so that only the upper levels are affected. This has been done by Storch et al. [2000] for REMO. In the case of REMO the nudging gradually increases in strength above the 850mb level, with no nudging below the 850mb level. This way the better representation of surface processes of the regional model is preserved, while still forcing the model to have the large scale field.
This form of nudging makes sense as it is the large scale patterns, through changes in the vertical component of the relative vorticity, that dictate the development of synoptic systems in the lower troposphere [Holton, 1992].

1.2 Introduction to the global model ECHAM$_{iso}$

The ECHAM model was developed from the global forecast model of the ECMWF to work as a climate model. ECHAM is a spectral model set up to be used with a horizontal triangular truncation of T21 to T106, and 19 vertical hybrid layers. The standard horizontal resolution is T42 with a time step of 24 minutes [Modellbetreuungsgruppe, 1993].
Following the pioneering work of Joussaume et al. [1984] and Jouzel et al. [1987] stable water isotope diagnostics was build into the hydrological cycle of ECHAM-3 by Hoffmann [1995] (see Section 1.4 for details). The model was validated against GNIP observations and found to capture the global

δ^{18}O pattern well [Hoffmann et al., 1998].
ECHAM$_{iso}$ has been run under palaeo-conditions for several studies using different configurations. A monsoon study for the Late Glacial Maximum (LGM) was carried out by Hoffmann and Heimann [1997] using the ECHAM-3 version of ECHAM$_{iso}$. ECHAM$_{iso}$ was then updated to the ECHAM-4 version [Werner et al., 2000]. ECHAM-4 has an improved radiation scheme compared to ECHAM-3, which resolved the problem of excessive solar radiation at the surface [Wild et al., 1996]. In a study focusing on the seasonality of precipitation, where ECHAM$_{iso}$ was run under LGM conditions, Werner et al. [2000] argued that the mismatch between the Greenland (GRIP) borehole temperature and the temperature calculated for the LGM using the isotope thermometer was due to lack of winter precipitation during the LGM. The lack of winter precipitation would give the impression of higher temperatures from the mean annual δ^{18}O compared to a situation with equally distributed precipitation throughout the year. In another study, also for the LGM, Werner et al. [2001] used ECHAM$_{iso}$ in a version which included moisture source diagnostics. They found no significant changes in the regional composition of moisture sources from the LGM to present, but the model did capture the large decrease of precipitation for polar regions. However, the rise in d-excess from LGM to Holocene found in ice core data was not reproduced by the model.
An isotope variability study for Greenland and Antarctica forced by observed SSTs from 1959 to 1994 was carried out by Werner and Heimann [2002]. It was found that one third of the modeled δ^{18}O variability could be explained by local changes at ice core drill sites in central Greenland and Antarctica. An imprint of the decadal NAO variability was found for western Greenland δ^{18}O (a subject treated extensively in Chapter 2.1 and 2.2), while the El Niño Southern Oscillation (ENSO) was found to be of less relative importance for sites in Antarctica. For d-excess no imprint of the NAO or ENSO was found for Greenland or Antarctica. The impact of the temperature in potential moisture source regions on the d-excess was also investigated. Only for sites in Antarctica a correlation between moisture source temperature and d-excess could be found.
Recently, and most relevant to the ECHAM$_{iso}$ study presented in this thesis, ECHAM$_{iso}$ was run under Eemian conditions [Herold and Lohmann, 2009]. However, the focus of Herold and Lohmann [2009] was mainly the monsoon system, whereas the study presented in Chapter 3 has a broader scope. The study of Herold and Lohmann [2009] will be returned to in Section 3.4, where the Eemian monsoon as modeled by ECHAM$_{iso}$ will be discussed.

1.3 Introduction to the meso-scale model REMO$_{iso}$

The REMO (REgional MOdel) climate model was developed from the Europa-Modell forecast model of the Deutscher Wetterdienst [Majewski, 1991]. Initially it was the result of the Europa-Modell being modified to work both in forecast mode and in climate model mode by Jacob and Podzun [1997]. Later on REMO was updated with ECHAM-4 physics parametrizations, and used to study the water budget in the Baltic region [Jacob, 2001]. Most relevant to this study, REMO was also optimized (updated to version 5.0) and validated for use in Arctic regions by Semmler [2002]. The updates for the Arctic include parametrizations of radiation, clouds, atmospheric liquid water, fractional sea ice, snow melt and refreezing, as well as initialization of ground moisture. Besides being able to work both as forecast or climate model, REMO can be run using either the parametrizations of the Europa-Modell or the ECHAM-4 parametrizations. The standard horizontal resolution of REMO is 0.5^o ($\sim$55km) and the model has 19 vertical hybrid-layers.
While the study presented in this thesis will be the first REMO study dedicated to Greenland, have other regional models extensively been used for modeling the Greenland climate. The regional models offer improved performance for precipitation regarding resolution of spatial patterns and temporal variability [Box et al., 2004]. This makes the regional models better suited for surface mass balance studies of the Greenland Ice Sheet, where models with improved surface processes are applied [Fettweis et al., 2008]. Also other small scale features important for ice sheet climate, such as katabatic winds, are being studied with regional models [Bromwich et al., 2001, van den Broeke and van Lipzig, 2003].
A study was made by Tjernstrom et al. [2005], where the performance of six regional models were evaluated with respect to the Arctic boundary layer. REMO was included in this study. The reported biases for REMO was mostly linked to the surface radiation budget, and authors mentioned cloud representation and surface albedo as the causes. This results in a surface temperature bias in REMO of -2^oC during summer and autumn. Also a temperature bias of up to $+2^oC$ in the lower troposphere was reported. This bias is fairly constant above 2km for spring, summer and autumn.

The application and development of REMO$_{iso}$

The isotope version of REMO is based on version 5.0 using the ECHAM-4 parametrizations. The implementation of the stable water isotope schemes were done by Sturm [2005] in a similar fashion as it was done for ECHAM$_{iso}$

[Hoffmann, 1995]. As ECHAM$_{iso}$ REMO$_{iso}$ has three separate hydrological cycles one for each of the three isotopologues $H_2^{16}O$, $H_2^{18}O$ and $HD^{16}O$, where isotopic fractionation is accounted for, for all phase changes. Kinetic fractionation is included during evaporation and during snow formation below -20^oC, as well as mixed phase cloud processes. REMO$_{iso}$ is the first, and only, regional model to have isotope diagnostics build in to the hydrologic cycle.

The first REMO$_{iso}$ experiment was a 2 year study set up with a domain covering Europe, and was validated using both daily and monthly δ^{18}O measurements from a geographical wide selection of sites [Sturm et al., 2005]. In this European study REMO$_{iso}$ was run with two types of boundary conditions for the prognostic variables and the isotope ratios at the lateral boundaries of the domain. First REMO$_{iso}$ was nested in the analysis of the European Centre for Medium-range Weather Forecasts (ECMWF), where the isotopic boundary conditions were calculated using a simple isotope-temperature relation. Secondly REMO$_{iso}$ was nested in ECHAM$_{iso}$, getting all fields from the global model. The results were that in the ECMWF-experiment the δ^{18}O was offset by -4.5‰ and had an overestimated seasonal amplitude, while the ECHAM$_{iso}$ experiment gave correct isotope levels, but with an underestimated seasonal amplitude. The authors concluded that the overall best performance of REMO$_{iso}$ was achieved using the ECHAM$_{iso}$ boundary conditions [Sturm et al., 2005].

The next REMO$_{iso}$ experiment was a 5 year ECHAM$_{iso}$-nested run carried out over South America [Sturm et al., 2007]. In connection with this experiment the performance of REMO$_{iso}$ was compared to that of two ECHAM$_{iso}$ with a resolution of T30 ($\sim$3.75^o) and T106 ($\sim$1.125^o), respectively. In the comparison it was shown, in relation to measured isotope data, that REMO$_{iso}$ out performed the courser resolution ECHAM$_{iso}$ experiments with better representation of precipitation patterns, seasonal isotopic amount effect and the continental depletion of isotopes [Sturm et al., 2007].

A longer experiment for Europe has also been done, where REMO$_{iso}$ was found to capture observed high and low frequency variations of δ^{18}O in precipitation and water vapour [Hoffmann et al., *in preparation*].

1.4 Isotopic fractionation in the hydrologic cycle of climate models

This section describes isotopic fractionation, and how isotope diagnostics are included in climate models. In the hydrological cycle fractionation of the stable water isotopes happens for all phase changes between the vapor, liquid and solid state, with the one exception being the evapotranspiration of plants [Zimmermann et al., 1967]. The three main isotopic components of water are $H_2^{16}O$, $HD^{16}O$, and $H_2^{18}O$, and their abundance are according to Dansgaard [1964] related approximately as

$$997680 : 320 : 2000 \text{ ppm (parts per million)} \tag{1.2}$$

Usually the isotopic composition of a sample is expressed with the δ relationship defined by Craig [1961]

$$\delta = \frac{R - R_{SMOW}}{R_{SMOW}} \cdot 1000‰ \tag{1.3}$$

where R can be the isotopic ratios of either [D]/[H] or $[^{18}O]/[^{16}O]$, and R_{SMOW} is the isotopic standard SMOW (Standard Mean Ocean Water).
Simply put the fractionation happens due to $H_2^{16}O$ being more volatile than the heavier isotopic components. This means that for a closed rainout process, due to for example convection, the heavy components will get progressively more and more depleted relative to $H_2^{16}O$.
For equilibrium conditions fractionation is described through a fractionation factor α, which is defined as the ratio between the vapor pressures of the light (p) and the heavy component (p')

$$\alpha = \frac{p}{p'} \tag{1.4}$$

Using the δ definition from Equation 1.3 equilibrium fractionation the fractionation can be described simply through the following equation

$$\delta_c + 1 = \alpha(\delta_v + 1) \tag{1.5}$$

where δ_c is the isotope composition for the condensate, δ_v is the isotope composition for the vapor and α is the equilibrium fractionation factor, which is dependent on temperature [Majoube, 1971].
For non-equilibrium processes, where dynamics or diffusion is involved in the phase change, the fractionation depends on the turbulent or molecular diffusivities. These non-equilibrium processes are often termed kinetic effects. The fractionation during evaporation over the ocean was incorporated in ECHAM [Hoffmann et al., 1998] using the following equation

$$\delta_e + 1 = \frac{1-k}{1-h}[\alpha(T_{Surf})^{-1}(\delta_{O_c} + 1) - (\delta_v + 1)h] \tag{1.6}$$

where δ_e is the isotopic composition of the evaporative flux from the ocean, δ_v is the composition of atmospheric water vapor, h is the relative humidity and α is the equilibrium fractionation factor, which is a function of the ocean surface temperature T_{Surf}. The factor k accounts for the kinetic effects during turbulent mixing in the atmospheric boundary layer. δ_{O_c} takes into consideration the enrichment of the oceanic surface layer during evaporation [Craig and Gordon, 1965]. This formulation of the evaporative flux is based on the work of Merlivat and Jouzel [1979]. From equation 1.6 it is clear that the modeled composition of the evaporative flux will be a function of T_{Surf} and h.

As a side note it can be mentioned that in simple Rayleigh-type fractionation models, a closure assumption is often made so that δ_v equals δ_e. This is only valid on a global scale and not regionally over the ocean, since the isotopic composition of the vapor at a given location is a mixture of the locally evaporated vapor and the vapor advected from the adjacent regions [Jouzel and Koster, 1996].

Two other non-equilibrium fractionation processes are included in the ECHAM model [Hoffmann et al., 1998]. Both of these processes are related to precipitation. The first process is valid for snow formation for temperatures under -20^oC, and deals with the differential molecular diffusion of isotopes in a supersaturated environment. The process was described by Jouzel and Merlivat [1984], and defined by these equations

$$\delta_c + 1 = \alpha_k \alpha (\delta_v + 1) \tag{1.7}$$

where

$$\alpha_k = \frac{S_i}{\alpha D/D'(S_i - 1) + 1} \tag{1.8}$$

with D being the diffusivity for $H_2^{16}O$ and D being the diffusivity for either $H_2^{18}O$ or $HD^{16}O$ as found by Merlivat [1978]. The combination of the kinetic fractionation factor α_k and and the equilibrium fractionation factor α defines the effective fractionation factor $\alpha_e = \alpha_k \alpha$, and S_i is the supersaturation relative to the saturation vapor pressure over ice. S_i is parametrized by the linear equation $S_i = 1 - 0.003T$, where T is the condensation temperature in ^oC. The exact formulation of S_i is a matter of best estimate and tuning, as it is not a well known quantity.

The second non-equilibrium fractionation process happens during the sub cloud base evaporation from rain drops, where the rain drops are partially evaporated. The formulation of this process is described similarly as the kinetic fractionation during snow formation, except the process goes on under undersaturated conditions [Hoffmann et al., 1998].

One shortfall of the fractionation scheme in ECHAM is that the evaporation from land surfaces is handled non-fractionating in a bucket-type formulation. It is known that fractionation during evaporation of recycled moisture over land does happen, and that it affects the deuterium excess of precipitation over continents [Hoffmann et al., 1998].
The subject of the impact of the kinetic effects on the deuterium excess in precipitation will be a recurring topic in this thesis, especially regarding the kinetic effect during snow formation.

Chapter 2

The REMO$_{iso}$ experiment

The data analysis in the three sections of this chapter will be restricted to time scales of monthly, seasonal and annual resolution. Also it should be mentioned that the focus will be on surface data such as the two meter temperature (T2m), precipitation and the δ^{18}O of precipitation in comparison with observations from meteorological stations, and ice core data.

2.1 Modeling the water isotopes in Greenland precipitation from 1959-2001 with the meso-scale model REMO$_{iso}$

2.1.1 Experiment setup

For the Greenland experiment REMO$_{iso}$ is used in a domain of 91x91 grid points with the standard resolution of 0.5° (longitude/latitude), 19 vertical layers and a time step of 5 minutes. The model domain was zoomed on Greenland and the surrounding North-Atlantic (see Figure 2.1). The experiment is setup in a rotated grid, with the Equator passing through the center of the domain. This means that the high and low latitudes are numerically represented in approximately the same spatial resolution. REMO$_{iso}$ was integrated over 44 years using the meteorological conditions and sea surface temperatures (SSTs) from 1958 to 2001. The first year of the model run is considered a spin up year, and is not used for the analysis. In order to approach to the real weather conditions during that time period as much as possible the model was forced towards the observed wind fields. This nudging technique gave very satisfying results in particular concerning the hydrological cycle, since only the wind fields were modified, whereas all other

prognostic variables were still computed independently.
In a first step the global model ECHAM4 fitted with water isotope diagnostics [Hoffmann et al., 1998] was run, and in a second step the regional model was run again over the same time period using the output of the first simulation. The isotopic GCM ECHAM4 was run in a nudged mode, that means that every six hours the simulated wind fields were slightly modified (the nudging technique is described in Section 1.1.3).

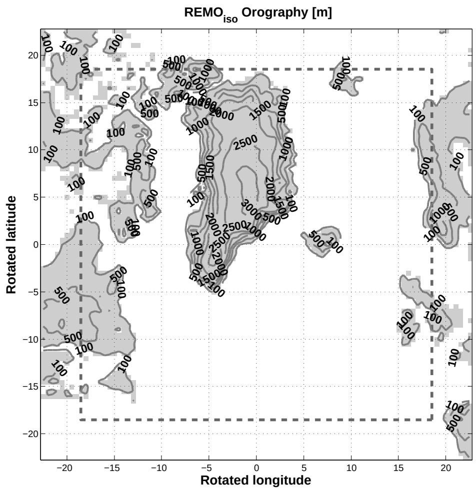

Figure 2.1: Model domain land-sea mask (shaded) and orography [m] for REMO$_{iso}$ in rotated coordinates. The model grid is 91 x 91 grid boxes with 0.5° or ~55km resolution. The dashed line marks the extent of the model domain without the 8 grid box wide buffer zone.

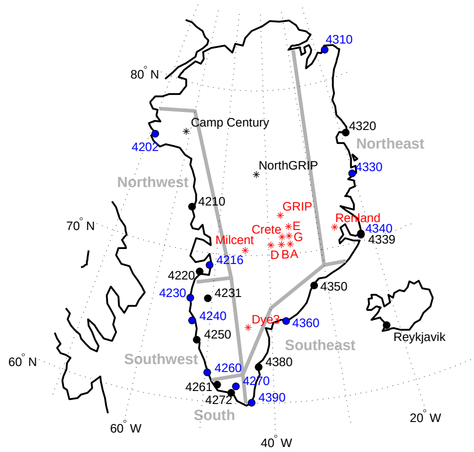

Figure 2.2: Numbered DMI coastal stations marked with blue/black dots. Data are available from http://www.dmi.dk. Ice core sites are marked with asterisks, with the sites used in this section marked in red. Also marked are the areas defining the coastal regions used in Figure 2.3.

Here the wind fields of the reanalysis product ERA-40 [Uppala et al., 2005] of the European Center of Medium-Range Weather Forecasts (ECMWF) is used covering the time period from 1958 to 2001. The global simulation provides the wind fields, which are by construction close to the observed ones, but also with optimised temperature, humidity and water isotope fields. This information is passed on to the regional model in two ways: First, the lateral boundary conditions of REMO$_{iso}$ are prescribed using the corresponding parameters (that is wind, temperature, humidity, water isotopes) from the global simulation. Over a buffer zone of 8 horizontal layers from the outer boundary this synoptical information is introduced into REMO$_{iso}$ (see Figure 2.1). Second, REMO$_{iso}$ itself is nudged in a similar way as the global model [Storch et al., 2000], that is, the simulated upper level wind fields were modified towards the reanalysis ERA-40 winds. Again all other prognostic parameters (temperature, precipitation etc.) of REMO$_{iso}$ including the water isotopes were calculated independently.

2.1.2 Meteorological observations and isotopic ice core data

The monthly meteorological Greenland data used in this study (see Figure 2.2 for the meteorological stations and for major inland ice core drilling sites) are provided by the Danish Meteorological Institute (DMI) [Cappelen et al., 2001, Jørgensen and Laursen, 2003]. The respective temperature and precipitation records have a good temporal coverage for the study period 1959 to 1999, which was simulated by the model. However, there are multiple cases of single missing months or even missing years, and in some cases the meteorological data sets were not complete (for example only T or only P was available). When comparing with REMO$_{iso}$ results the data structure of the observations is imitated, that is, whenever there are missing observations the corresponding model results are excluded from the further analysis.
Seasonal inland δ^{18}O records have been produced for 19 Greenland ice cores from 10 sites [Vinther et al., 2008]. Even at relatively high-accumulation sites the measured seasonal isotope signal does not correspond to the signal in precipitation. Isotopic diffusion in the firn progressively reduces the seasonal amplitude. Therefore, in a first step the original amplitude is reconstructed at most sites by a numerical back-diffusion approach [Johnsen, 1977]. Due to the appearance of melt layers at two sites (Dye3 and Renland) this approach leads to major inconsistencies and a modified technique was applied for these sites (for details see Vinther et al. [2008]). In the next step, winter and summer signals have to be defined in a sensible way. Assuming that the seasonal δ^{18}O maximum/minimum coincides with the maximum/minimum in temperature two reference dates (mid-summer and mid-winter of a specific year) are defined. Vinther et al. then assumed a nearly flat seasonal amplitude in precipitation amount and addressed half of the annual precipitation to each season. This means that summer corresponds to the period May to October and winter to the period November to April. Though this approach depends on the approximate stability of seasonal precipitation Vinther et al. showed that the seasonal isotope records are precise enough to allow for a quantitative comparison with meteorological observations.

To assess the quality of the accumulation on the Greenland ice sheet as calculated by REMO$_{iso}$ the PARCA data set is introduced. The PARCA data [Bales et al., 2001] is an accumulation map based on interpolation of over 200 shallow ice cores, snow pits and meteorological station data producing a high resolution map for the period 1971 to 1990.
The North Atlantic Oscillation (NAO) data was downloaded from the NAO web page of the Climate Research Unit
(http://www.cru.uea.ac.uk/cru/data/nao.htm).

2.1.3 Climatology

In this section the model skill for temperature, precipitation and spatial δ^{18}O is evaluated with respect to the long term observed climatology. As several other climate models REMO$_{iso}$ has a warm bias over the ice sheet [Walsh et al., 2008]. For example, the average temperature for 1959 to 1999 for the data grid point closest to the Summit station is -25.9^oC, while the observed mean temperature is reported to be -32^oC [Johnsen et al., 1992]. This warm bias is similar to the results of a SST forced GCM experiment for 1950 to 1994 by Werner and Heimann [2002] using the same global model (ECHAM4) as in this study. For this study the height difference of 91m between the model and the actual site is relatively small, and other factors are responsible for this significant model bias. The overestimated temperatures are most pronounced at high and intermediate altitude on the ice sheet. This model deficiency is much stronger in the Northern and Central Part of the icesheet and hardly significant in the South. This bias becomes particularly strong during summer time and is approximately $+3^oC$ in Southern Greenland and up to $+7^oC$ in the North. The fact that the model bias peaks during summer times points to possible problems with the computed surface albedo. REMO$_{iso}$ computes a varying snow albedo (fresh snow having a higher albedo) allowing for a maximum albedo of 0.8, whereas most observations indicate higher values of about 0.85 [Box et al., 2006]. Box and Rinke [2003] found as well a warm bias in their simulation with the HIRHAM regional model, and rather than the albedo being the problem, pointed to the importance of a realistic description of the boundary layer over the icesheet. As discussed in Section 1.3 it has been found by Tjernstrom et al. [2005] that REMO indeed has some temperature biases for the Arctic related to the boundary layer. However, the study by Tjernstrom et al. [2005] was carried out over the Arctic ocean, and further investigations are needed to conclude whether this translates to high elevation sites such as the Greenland ice sheet as well.
For the coastal areas the simulated temperature is generally too cold by a few degrees compared to DMI station data, with the largest cold bias during win-

ter. This is not in agreement with the study by Tjernstrom et al. [2005], also mentioned above, where the bias was found to be greatest during summer. For some stations the cold bias can be explained partly by model orography, but the tendency also exists where there are only negligible differences between the model and the observed elevation. Other effects specifically important to the climate on the edge of ice sheets, such as misrepresentation of katabatic winds, might be responsible for this.

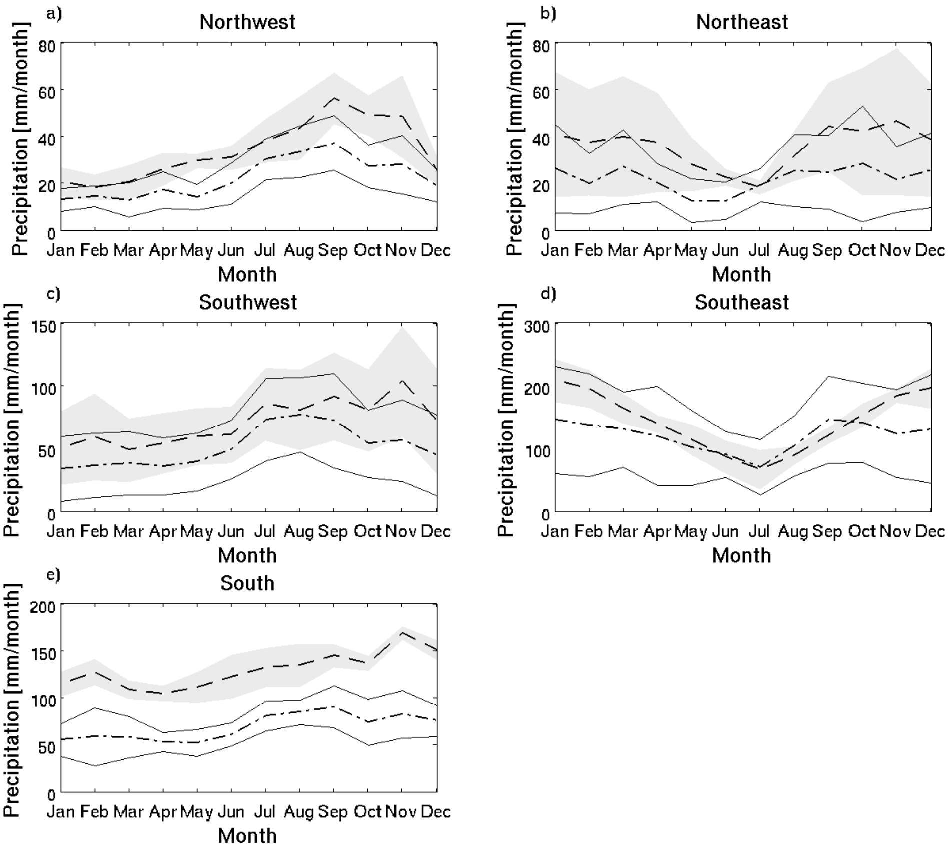

Figure 2.3: Observed and modelled annual cycle for precipitation averaged for 5 coastal regions as defined in Figure 2.2. The time period is 1961-1990. Stations 4210, 4216, 4231, 4240, 4261, 4330, 4340, 4350 and 4380 (see Figure 2.2) have more than 5 years of missing data in the period. Model data is the dashed line with the grey shaded area for one standard deviation and the observed data is the dashed dotted line with the full lines for one standard deviation.

The seasonal cycle for precipitation

In the following the simulated precipitation amount and seasonal cycle is evaluated using observed DMI precipitation data for the period 1961 to 1990. It should be noted that most of the stations have single or multiple missing monthly values in the period 1961 to 1990 and stations 4210, 4216, 4231, 4240, 4261, 4330, 4340, 4350 and 4380 have more than 5 years missing during this period. A systematic deviation towards wet conditions is identified along Greenland's coast possibly due to a generally wet and warm bias imposed by the global climate model (ECHAM).
The water isotopes undergo a pronounced seasonal cycle (in the order of 15‰ in the interior of the ice sheet for δ^{18}O) and each bias in the seasonality of accumulation has a direct consequence on the mean isotope signal. It is therefore important to evaluate the capability of the model to simulate the regionally varying seasonal precipitation cycle. The various meteorological stations were divided in five groups considering geographical placement and similarities in the annual cycle of precipitation (see Figure 2.2). In Figure 2.3 the modeled and observed seasonal cycle for five Greenland regions is plotted. The agreement between the model and the observations is quite good. See in particular the late summer/autumn maximum in the Northwest and the pronounced summer minimum in the Southeast both nicely captured by REMO$_{iso}$.

Greenland accumulation

The spatial pattern and absolute amount of precipitation is important for the surface mass balance of the ice sheet. The modeled accumulation depends on the interplay of many factors such as realistic storm tracks, a well resolved orography, a realistic lapse rate over the ice sheet or a realistic large scale moisture transport which is in our case controlled by the global model ECHAM4. Figure 2.4 shows the model accumulation compared to the climatological PARCA [Bales et al., 2001] accumulation (that is P-E without melting and runoff) map. The PARCA data are based on interpolation of over 200 local estimates from shallow ice core data and station observations. The model reproduces many features of the spatial accumulation such as the large maximum along the south-eastern coast of Greenland and the minor local maximum southwest of Pituffik/Thule (station 4202 in Figure 2.2). These maxima are in fact controlled by the principal entrance points of North-Atlantic storm tracks on the Greenland ice sheet. Also the large very dry area in the central and eastern parts of the ice sheet is captured by the model. The PARCA accumulation map shows a latitudinal gradient calculated over equal areas from 558 mm/yr about 65^{o}N (DYE3) to 194 mm/yr east of Camp Century (77^{o}N), corresponding to a reduction of accumulation over the ice sheet by a factor of 2.9. REMO$_{iso}$ reasonably reproduces this latitudinal structure with 1026 mm/yr for the southern area to 226 mm/yr in the northern area. This is a reduction of a factor of 4.5.

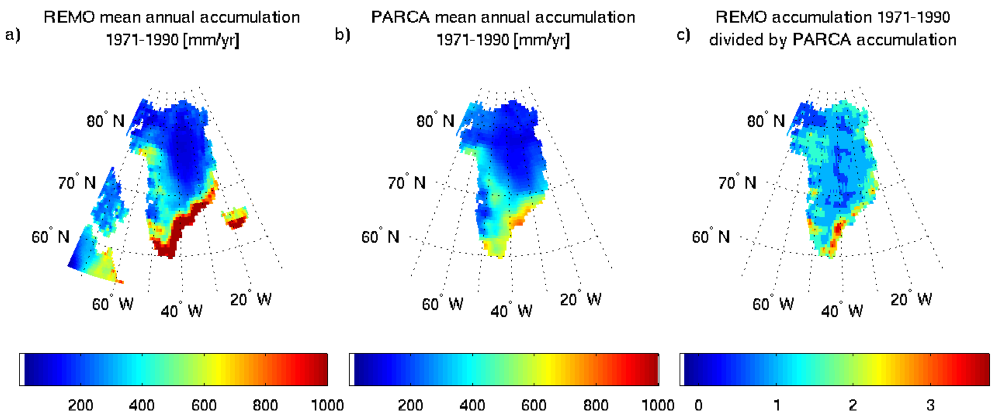

Figure 2.4: Modelled accumulation [mm/yr] compared with the PARCA accumulation map [mm/yr]. Both data sets have been interpolated to a 0.5^{o}x0.5^o geographical grid. The PARCA data was originally in a 5km UTM grid. In figure **a** and **b** the same colour bar is used to ease comparison. In fact the maximum values for figure a is more than 2000 mm/yr, while the maximum in figure **b** only is about 800 mm/yr. The differences in magnitude are illustrated by figure **c** which is REMO$_{iso}$ accumulation divided by PARCA accumulation both annually averaged for the period 1971-1990. Each colour signifies that the model will be within ± 25% of a given multiple of the PARCA data.

The model produces too little precipitation in central regions of the ice sheet, where the precipitation is underestimated by about 25%, while in some areas towards the coast the model overestimates the amount of precipitation by about 50%. This is also seen in the comparison with the observed DMI coastal data (see Figure 2). However, the large overestimation for the southeastern maximum compared to the PARCA accumulation is probably an artifact. The PARCA accumulation is focusing on the interior of the ice sheet and the data set was constructed to better understand ice sheet dynamics. Coastal areas are however not represented in detail [Bales et al., 2001]. When comparing the PARCA data with the DMI weather stations, much

higher accumulation are found for a number of these coastal sites (PARCA maximum in the Southeast: 800mm/yr, DMI station 4390 (see Figure 2.2): 1900mm/yr).
For the total accumulation (that is P-E) over Greenland the IPCC [Church, 2001] gave a best estimate of 225±41 mm/yr considering the standard deviation between about a dozen studies. The PARCA data set gives a total accumulation value of 300±80 mm/yr. Former modeling studies underlined the importance of numerical resolution for matching approximately the correct accumulation. In Kiilsholm et al. [2003] the authors note an improvement in the total simulated accumulation from 421±183 mm/yr (± refers to inter-annual variability in the following) using the coarse coupled ECHAM4/OPYC model configuration to a more realistic 224±35 mm/yr using a nested regional model (HIRHAM) in an approach similar to this study with the REMO$_{iso}$ regional model. Here both models, the global and the regional model, were nudged to guarantee a realistic circulation pattern over the simulated interval. As in many simulations before (see above) this did not solve the problem of a general warm bias of the models and contributes probably to the too wet conditions in particular in some coastal areas. For the period 1960-1990 REMO$_{iso}$ computed a mean accumulation 353 ±78 mm/yr. Although this is less than the value for ECHAM4/OPYC mentioned above, it is still an overestimation of the accumulation compared to PARCA and Church [2001].

Isotope climatology

Comparing the seasonal mean isotope signals for the 19 ice core sites (see Table 2.1) the model computes a positive bias in $\delta^{18}O$ of about 2-3‰ during winter and 5-6‰ during summer resulting in an annually weighted overestimation of 4.4‰. In the case of Renland the positive bias is even greater. This is due to the model orography where the Renland site is almost 1300m too low compared with the actual site elevation.
Looking at the low elevation IAEA [2006] sites the model data is less dependent on latitude compared to the GNIP data, with and gradient of -0.29‰ per degree N for the model and a gradient of -0.59‰ per degree N for the GNIP data. This is essentially an underestimation of the observed northward depletion of ^{18}O.
Spatial isotope/temperature slopes are the modern analogue for the interpretation of deep ice core records. For the land areas shown in Figure 2.5 the model produces an isotope versus temperature slope of 0.70‰$/^oC$, while the observed slope for the combined data from the North Greenland Traverse, ice core sites and IAEA/GNIP stations is 0.81‰$/^oC$. This discrepancy could

be due to the non-negligible temperature bias over Greenland (see beginning of Section 2.1.3), as well as the underestimated northward depletion of ^{18}O mentioned above.

	Summer δ^{18}O (May-Oct)			Winter δ^{18}O (Nov-Apr)		
Site	ice core	REMO$_{iso}$	Anomaly	ice core	REMO$_{iso}$	Anomaly
GRIP stack	-31.9	-26.0	5.9	-37.8	-34.4	3.4
DYE3 stack	-26.9	-21.6	5.3	-28.7	-27.1	1.6
Renland	-26.4	-17.6	8.8	-28.1	-22.2	5.9
Crete	-32.4	-25.6	6.8	-36.0	-33.4	2.6
Milcent	-26.9	-22.3	4.6	-31.2	-29.2	2.0
Site A	-30.9	-25.9	5.0	-35.3	-34.4	0.9
Site B	-31.0	-25.4	5.6	-35.8	-33.5	2.3
Site D	-29.7	-24.5	5.2	-34.6	-32.3	2.3
Site E	-32.0	-26.3	5.7	-37.8	-34.9	2.9
Site G	-31.5	-25.8	5.7	-36.8	-34.5	2.3

Table 2.1: Mean seasonal δ^{18}O for seasonally resolved shallow ice cores compared to the weighted seasonal mean for the nearest point in the model data grid. The time span for the comparison goes from the summer of 1959 (winter 1960) to the time span of the individual (or stacked) cores. The GRIP stack is based on 6 ice cores, while the DYE3 stack is based on 5 cores.

Both the modeled slope of 0.70‰$/^oC$ and the observed slope of 0.81‰$/^oC$ shown in Figure 2.5d differ from the Greenland slope of 0.67‰$/^oC$ given by Johnsen et al. [1989]. However, the slope of 0.67‰$/^oC$ was calculated from observations at ice core sites only, and for a much narrower temperature range than the modeled/observed data discussed here.
To further investigate the spatial isotope/temperature slope the local spatial isotope/temperature gradient considering the adjacent grid points equivalent to a 350km x 350km area around each point was calculated. Regionally the isotope signals do not necessarily correspond to the temperature conditions. Whereas the former is finally controlled by cloud conditions surface temperatures are very sensitive to clear sky radiative cooling and/or sea-ice coverage for nearby coastal areas. The spatial relationship will be a result of physically different mechanisms controlling on one hand the surface temperatures and on the other hand cloud conditions and the water isotopes.
Large differences can be seen across Greenland for the local spatial slope. For example the area of very steep isotope/temperature slopes near the north-eastern and eastern coast of Greenland. This could be connected to the cold East Greenland Current generally cooling this area, as well as damping the

temperature variability, and in this way giving a steeper slope.

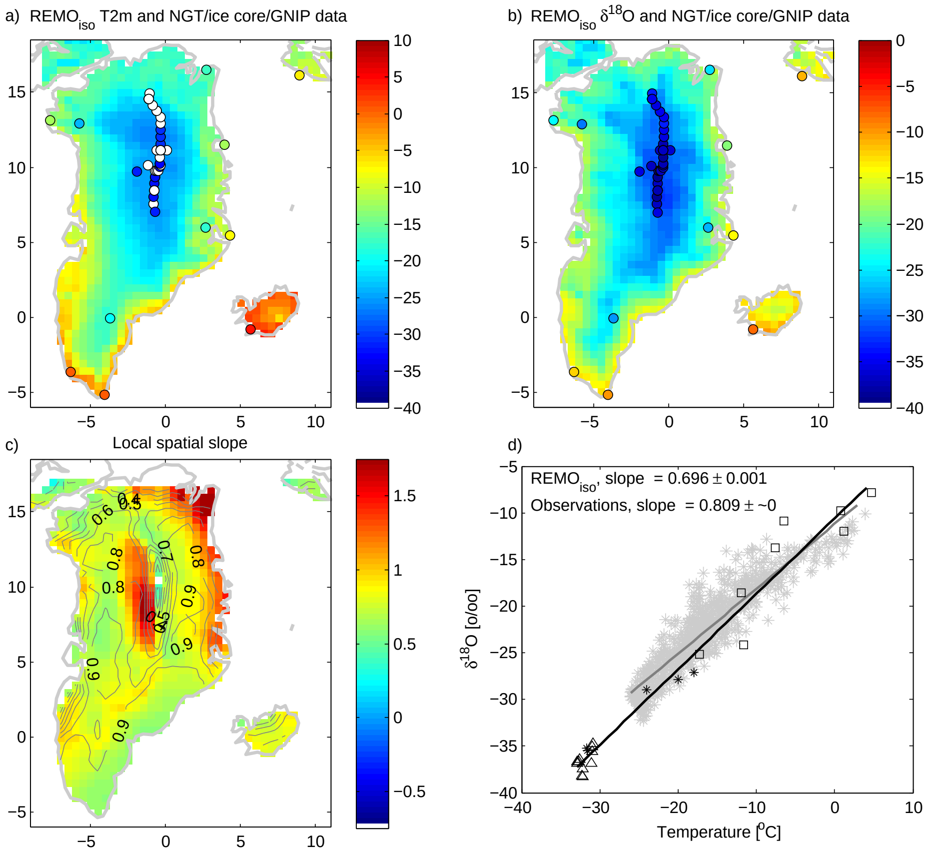

Figure 2.5: a) Annual mean modeled temperature (T2m) in ^oC with observed data from the North Greenland Traverse (where available), ice core sites and IAEA/GNIP stations. b) Annual mean modeled δ^{18}O weighted with accumulation in ‰ with observed data from the North Greenland Traverse [Fischer et al., 1998], ice core sites and IAEA/GNIP stations [IAEA, 2006]. c) The local δ^{18}O versus temperature slope calculated for an approximately 350km x 350km area in the model grid. Also shown in 0.1 step contours is the R^2 for the same data as the calculated slopes. Data is only shown for $p < 0.05$. d) The spatial regression slope of δ^{18}O versus temperature for Greenland, including points from Iceland and Svalbard. Model data is the light grey markers, while North Greenland Traverse data is marked with triangles, ice core date with asterisks and IAEA/GNIP data with squares.

A similar pattern can be seen in Central Northern Greenland with a relatively rapid change from a steep isotope/temperature gradient west from the centre to a flatter gradient east from the centre. It is assumed that this pattern is mainly controlled by orography and its impact on both surface and cloud processes.

2.1.4 Inter-annual variability of seasonal data

Vinther et al. [2008] demonstrated the fundamentally different behaviour of inter-annual climate variability over Greenland for summer and winter season. Therefore the authors put much effort into a more proper separation of seasonal isotope signals deduced from different Greenland ice cores (see above in Section 2.1.2). Similarly, here the seasons are defined by taking the period from May to October as summer season and the period from November to April as winter season. This division of the year goes against the traditional four season division of the year, however the division of the year in just two seasons is more robust when comparing with the isotopic signals in the seasonal ice core data.

Temperature and precipitation

The DMI stations for this analysis of inter-annual seasonal variability of temperature and precipitation have been selected for the best temporal and spatial comparison with the model data. Seasonal means are only calculated when all of the six months are present in the observed data. The common variability between the model data and the observations is calculated here as the square of the linear correlation between the two data sets, thereby giving the percentage of common variability.
Before analysing the ice core records the model skill will be estimated by comparing the inter-annual variability of temperature and precipitation at the coastal weather stations. For temperature the model/data correlation is systematically higher during winter times than during summer. Studies of the south western Greenland temperatures show that the winter temperature has more than twice the variability of the summer temperature Vinther et al. [2006]. The higher winter variability is more strictly controlled by large scale circulation features such as the NAO.
Since the nudged model is forced to reproduce the circulation patterns winter temperatures are quite closely matched. In fact for the coastal stations the model explains between 5% and 81% of the inter-annual winter variability. During summer the model performs significantly worse (0-65% explained variability), when local effects poorly constrained by the large scale wind field (such as sea breezes) are of relative more importance due to the weaker synoptic activity.

The skill of the precipitation simulation is in general worse than for the temperature field (between 2% to 61% explained variability). Overall the simulated inter-annual precipitation variability is in only slightly better agreement with observations during winter than during the summer season, and does not strictly follow the pattern of good/bad performance of the temperature variability.

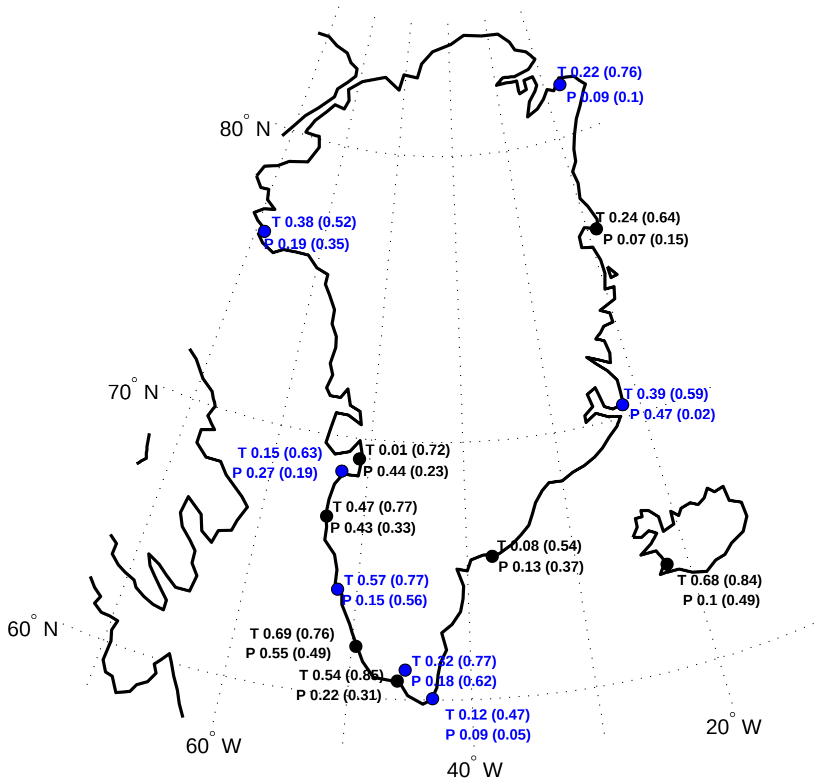

Figure 2.6: R^2 for seasonal model data versus observations for temperature (T) and precipitation (P) plotted at each station location. The first number is the result for summer while the number in parenthesis is the result for winter.

One thing to note with respect to the precipitation observations is the difficulty of collecting samples in Greenland. Due to the often strong wind and solid precipitation, blowing snow will cause the precipitation amounts to be unreliable, even though measures have been taken to avoid these effects [Cappelen et al., 2001]. The quality of the precipitation observations can therefore also be a factor for the evaluation of the model skill.

In general South and Southwest stations correlate best to the simulated pre-

cipitation signal, probably since most of radiosonde and weather stations of Greenland that enter the ERA-40 data set are situated there [Uppala et al., 2005]. The information of these stations together with marine automatic weather buoys largely improve the reanalysis wind fields, and therefore better constrain the regional weather patterns. In the Northeast of Greenland very few observations are available and used in producing the re-analysis fields. The increasing number of degrees of freedom produced by the model's dynamics degrades the quality of the simulated precipitation signal for the regions in question. In other words, the local biases are thereby stronger in precipitation compared to temperature. In Section 2.2.1 the variability of temperature, $\delta^{18}O$ and precipitation in the $REMO_{iso}$ experiment will be discussed in general, as well as the relation between summer and winter variability.
The model performance for temperature is relatively bad at two western stations, 4216 and 4220, which is due to extremely low SST values in the reanalysis during the first couple of years of the simulation. Local deviations such as this are probably due to a bias in sea ice in ERA-40 for the respective fjords. Additionally, there is in the case of station 4360 and 4390 a stronger long-term warming trend in the model output compared to the DMI observations. This is responsible for the relatively low correlation at these two stations.

Isotope variability

Here the simulated isotope signal will be evaluated by comparing to observed data from three sites, which have been selected with respect to the quality of the observations. The observed isotope data include $\delta^{18}O$ from the Dye 3 and GRIP drilling sites, both corrected for post-depositional processes, and also the monthly IAEA/GNIP observations from Reykjavik, Iceland. The resolution of both ice core records is sub-annual and allows proper construction of a summer and winter record (see Section 2.1.2 for details). Also, it is very important to improve the signal to noise ratio of the ice core signal by stacking individual cores when comparing to the model output. Surface effects, as for example sastrugi, can cause large differences between individual ice cores from the same drill site.
The simulated isotope signal deviates by $+1.6‰$ ($+5.3‰$) at DYE3 for winter and summer respectively and by $+3.5‰$ ($+6‰$) for GRIP and have been corrected by this amount for the representation (see Figure 2.7 and 2.8). It should be noted that these simulated isotope biases follow the same pattern as the temperature bias mentioned above (see section 2.1.3). The simulated isotopes deviate most from the observations during summer time, as it was

the case with simulated temperatures.

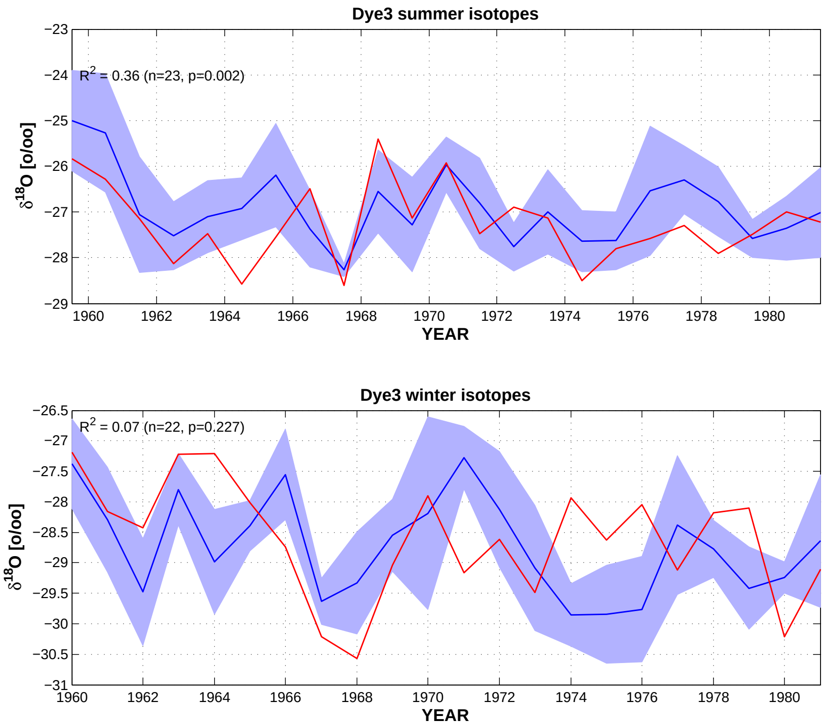

Figure 2.7: Stacked summer (upper) and winter (lower) δ^{18}O values for Dye3 (solid blue) compared with weighted (solid red) modeled δ^{18}O. Model output has been offset with the mean difference between model and observations. The light blue shading is the standard deviation for the stacked data. Not all ice cores span the full length of the stacked record. The Dye3 data is based on 5 cores.

The stacked GRIP winter data and DYE3 summer data show reasonable correlation with the model, while the GRIP summer and DYE3 winter show relatively poor correlation. It should be noted that these records are quite short (n=22 for the DYE3 winter data) and just one misrepresented year (by either the model or in the seasonal definition of the ice core data) has a major impact on the correlation. For instance in Figure 2.7, the DYE3 winter record shows a maximum in 1971 whereas the model shows a similar maximum one year before in 1970.
The ice core dating is done using numerous tie points (volcanic or radioactive markers), which avoid that possible dating errors propagate easily throughout the entire record. However, the standard deviation for both sites show

that there is a significant spread in the ice core data, even though the stack of 5 records in the case of DYE3 and 6 records in the case of GRIP certainly improved the signal to noise ratio.
Nevertheless, the model captures some aspects of inter-annual isotope variability and uncertainties exist both for the observations as for the model performance. For instance the simulated isotope signals show significantly larger winter variability than summer variability at the DYE3 and GRIP sites (Simulated: σ_{win}=1.58‰ and σ_{sum}=1.0‰ for the GRIP site and σ_{win}=1.09‰ and σ_{sum}=0.84‰ for the DYE3 site) in agreement with observed temperature variability from coastal meteorological stations and with a detailed analysis of Greenland isotope signals over the last 1400 years [Vinther et al., 2008].

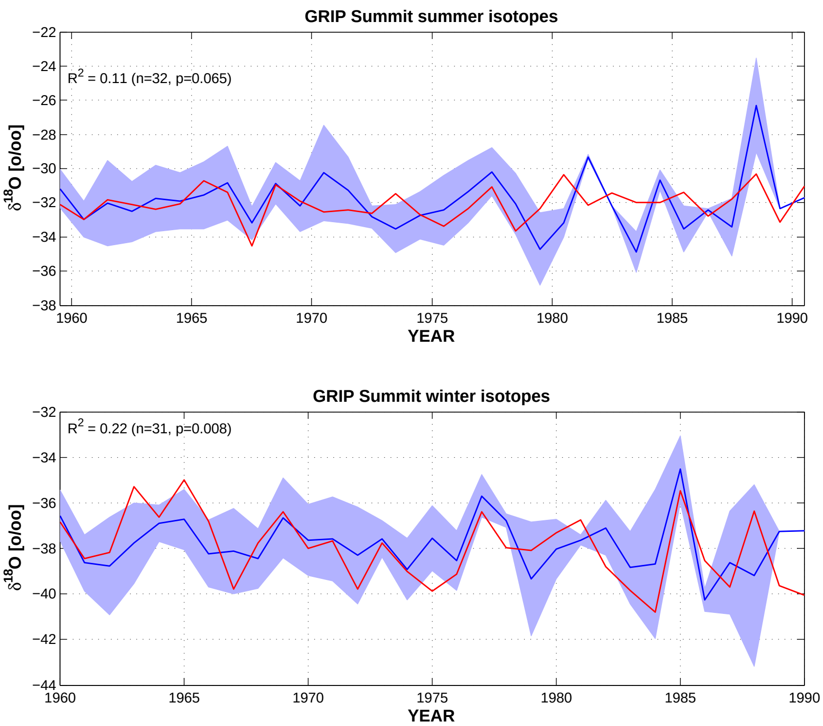

Figure 2.8: Same as Figure 2.7 but for GRIP. Here the data is based on 6 cores, and as for DYE3 not all the ice cores span the full length of the stacked record.

The two stacked records from Dye3 and GRIP, however, give a different seasonal signal, and GRIP actually show larger summer than winter variability (observed: σ_{win}=1.15‰ and σ_{sum}=1.61‰ for the GRIP site and σ_{win} =

0.8‰ and σ_{sum}=0.78‰ for the DYE3 site). Several problems could contribute to this difference: 1) The statistics of the observations is relatively short (23 years for DYE3 and 32 for GRIP). 2) Post-depositional noise obviously not considered in the model can disturb the stacked record considerably. In 1988 the stacked GRIP record consisted only of two individual cores which then contributed considerably to the remarkable summer peak in the isotope record. 3) The definition of a winter and summer signal in the individual ice core records is based on the assumption of equally distributed precipitation over the year. This assumption might fail in certain years and winter precipitation might have been added to the summer signal (or vice versa).

Modeled and observed Reykjavik δ^{18}O

Since the 1960s, precipitation was collected at several weather stations on a regular basis in Greenland and was subsequently isotopically analysed. The quality of the early data however is not always satisfactory and continuous data are not available for the Greenland weather stations. Therefore a comparison is made here of the observed and simulated isotope signals at Reykjavik, which has good quality continuous δ^{18}O monthly data covering the period 1992 to 2001 [IAEA, 2006]. Reanalysis data forcing the model runs are also better in the 1990s than in the earlier part, and it is expected that the model results to be close to observations.
For the period shown here, and in general, REMO$_{iso}$ captures the monthly and seasonal variations in temperature quite well, with a R^2 of 0.76 and 0.84 for summer and winter, respectively. The model does a fair job of reproducing the precipitation, with a R^2 of 0.10 and 0.20 for summer and winter, respectively.
For Reykjavik there is an isotopic offset of 2‰ for the summer season, while the winter data show an offset of about 0.5‰. There are no clear biases in temperature that could explain these off sets.
The summer data show considerably lower variability compared to the winter data, and only spurious correlation between the model and the observations. As opposed to the summer data, the observed and simulated winter data show a correlation of R^2=0.3 (however, due to the small number of degrees of freedom this results is not significant, p=0.13) and higher inter-annual variability (see Figure 2.9). It is however clear, when reviewing the monthly data, that the model often fails to capture the winter minima of particularly negative δ^{18}O values. For the monthly temperatures and precipitation amounts the model shows no clear signs of not being able to capture cold temperatures, or precipitation amounts, during winters with low δ^{18}O val-

ues (see Appendix A.1 for plots of monthly temperatures and precipitation). However, this could be due to processes happening on a sub monthly time scale, and a review of the model performance on event time scales, that is days and hours, is needed to understand this further.
In summary these results for the Greenland ice core sites and Reykjavik imply, that for a proper calibration of the annual isotope signal one mainly needs a proper understanding of winter circulation over Greenland.

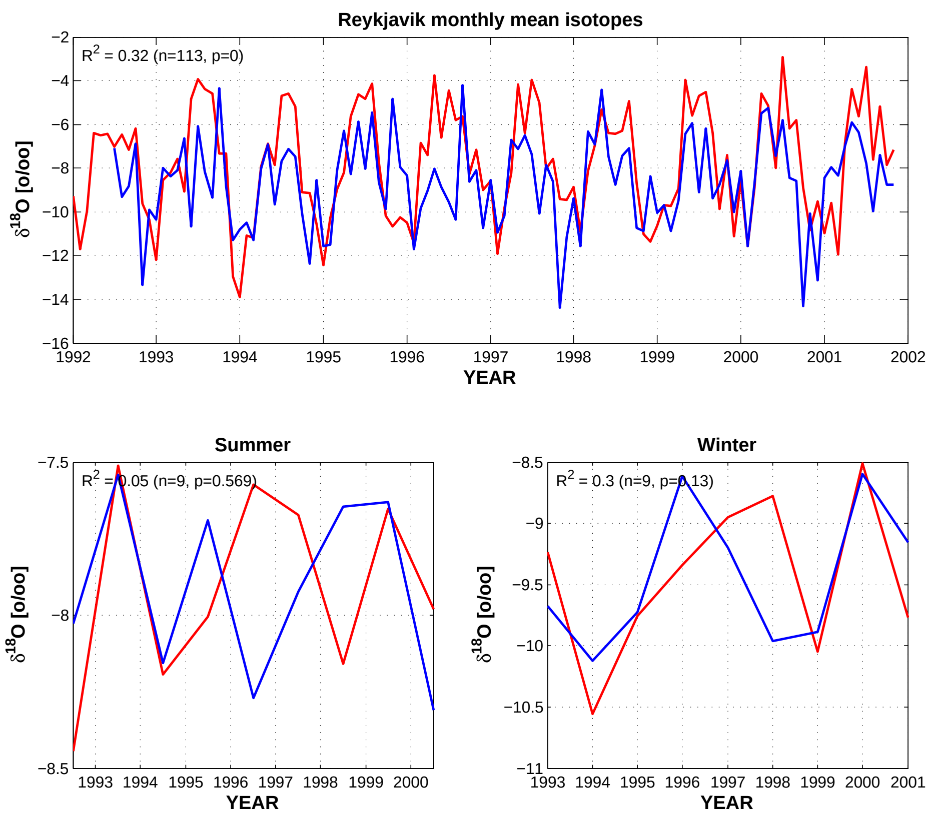

Figure 2.9: Modeled δ^{18}O and measured δ^{18}O for Reykjavik. Full blue lines are the GNIP Reykjavik data, and the dashed red lines are modeled data. The upper panel is the monthly mean values, while the two lower plots show averaged summer and winter values. For the seasonal plots the mean offset between the observations and the model output has been subtracted from the model output.

2.1.5 NAO and Empirical Orthogonal Functions

In the following the drivers of the inter-annual variability over Greenland is studied, as well as the impact of these mechanisms on the water isotopes. For this purpose a Principal Component Analysis (PCA) of modelled seasonal temperature, δ^{18}O and precipitation was performed for the entire period of 1959 to 2001 (see Appendix A.2 for details on the PCA method). As a part of the PCA procedure the data were centred and normalized. This guarantees that the loadings on the Principal Components (PCs) actually show a true pattern of variability and not only the difference in absolute variability between continental and coastal areas [Slonosky and Yiou, 2001]. Here the common practise of using the term Empirical Orthogonal Functions (EOFs) for the spatial patterns of the loadings on the PCs, and using the term PCs for the time series of the PCs is adopted.
To be sure not to include EOFs that might be mixtures of different variability patters (that is, having *effectively degenerated* eigenvectors) the uncertainty of the size of the eigenvalues of the EOFs were estimated using the "rule of thumb" suggested by North et al. [1982]. In the PCA results presented here the focus will be first and foremost on the first EOFs, as only the eigenvalues of first EOFs have been found not to be possibly effectively degenerated for all tree variables: temperature, δ^{18}O and precipitation (see Appendix A.2 for details).
The NAO is one of the leading circulation modes in high northern latitudes, and it is defined as the normalized pressure difference between Reykjavik, Iceland, and Ponta Delgada, Azores [Walker, 1928]. Since the model was forced to agree with the observed wind fields it is not surprising that the model reproduces the atmospheric circulation and pressure shifts linked to the NAO. Over the 50 year period the simulated pressure variations at Reykjavik were in close agreement with the observed ones (R^2 Winter=0.77 and R^2 Summer=0.7). The general and well-known impact of the NAO is a varying strength of the meridional versus zonal circulation over the North Atlantic. As a consequence, colder (NAO positive) and warmer (NAO negative) temperatures hold in Greenland, with the opposite being true for Western Europe.
The NAO is largely an unpredictable atmospheric circulation phenomenon. With this being said Hurrell [2003] listed three things that could be major influences on the NAO. Firstly, the NAO is sensitive to tropical heating, and might be influenced by persistent SST changes in the tropics. Secondly, the interaction between the stratosphere and the troposphere could be important, when coupled with solar or anthropogenic forcing. This can impact the polar vortex during winter, which in turn affects the NAO. Finally, changes

in the heat exchange between atmosphere, ocean, sea ice and land might be important for tendencies in the NAO.

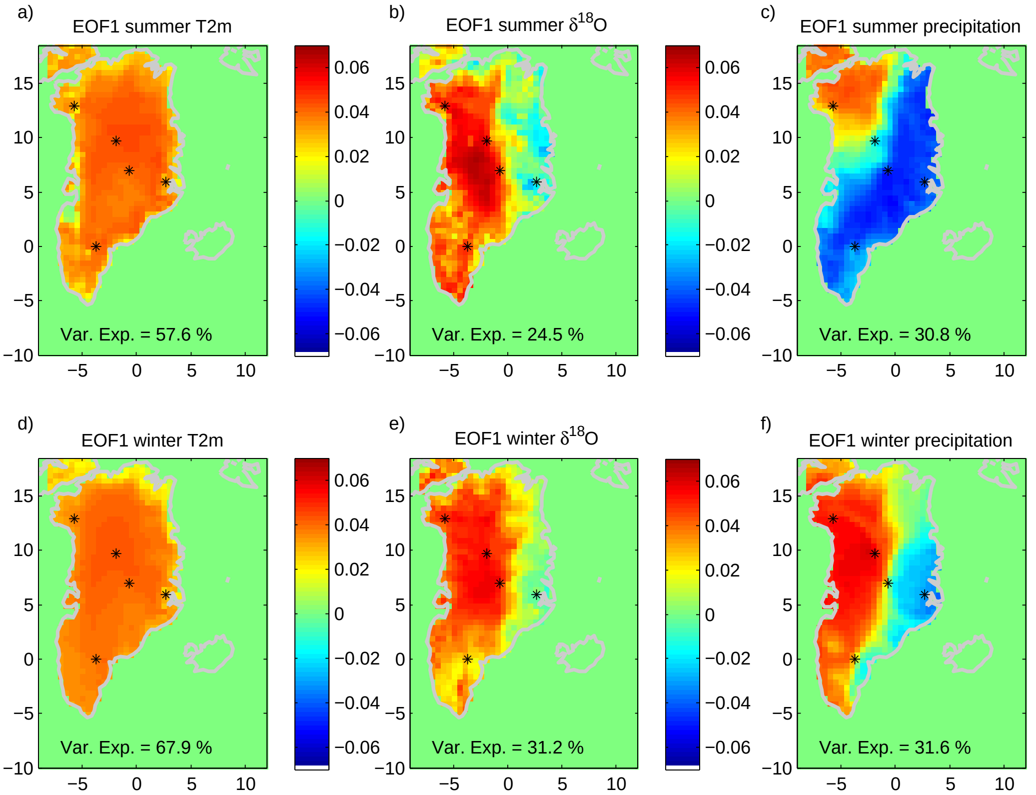

Figure 2.10: This figure shows the loadings on PC1 for temperature, δ^{18}O and precipitation for summer (figure a, b and c) and winter (figure d, e and f). The explained variance of the pattern is noted, as well as the position of important ice core drilling sites.

The loading on the first principal components

In the following the focus will be on the EOF1 for all three variables (temperature, water isotopes and precipitation), which later will be shown to be linked to the NAO. In agreement with the analysis of winter versus summer variability (in Section 2.1.4) the explained variability of the EOF1 of each variable is systematically lower in summer than in winter time. In fact EOF1 for temperature explains a large part of the inter-annual variability (58% and 68% for summer and winter respectively), whereas both precipitation and the water isotope pattern explain a comparable fraction of the total variability of about 20-30%. The winter and summer EOFs for temperature are uniform over entire Greenland, with the exception of the relatively weak loadings on the eastern coast of Greenland.

	Variance explained		R^2 with NAO **p<0.05**	
T2m	Summer (May-Oct)	Winter (Nov-Apr)	Summer (May-Oct)	Winter (Nov-Apr)
EOF1	0.58	0.68	**0.19**	**0.44**
EOF2	0.13	0.12	0.02	0.03
$\delta^{18}O$	Summer (May-Oct)	Winter (Nov-Apr)	Summer (May-Oct)	Winter (Nov-Apr)
EOF1	0.24	0.31	**0.12**	**0.21**
EOF2	0.11	0.15	~0	~0
Precipitation	Summer (May-Oct)	Winter (Nov-Apr)	Summer (May-Oct)	Winter (Nov-Apr)
EOF1	0.31	0.32	0.03	**0.25**
EOF2	0.19	0.22	**0.10**	0.01

Table 2.2: The first two columns contain the explained variance of the first two EOFs for mean seasonal Ts, $\delta^{18}O$ and precipitation, while the last two columns are the common variance of the first two PCs with the seasonally averaged NAO. The significant correlations with NAO are in **bold**.

To confirm that the model's first mode of inter-annual temperature variability is linked to the NAO the running mean correlation for NAO is calculated with PC1 using an 11 year window. The significance of the running correlation is estimated using bootstrap resampling. It is seen from Figure 2.11 that for the winter PC1 the correlation is strongly negative and significant for the entire period, with only a brief interval of weaker correlation during the 1970s. For entire period from 1959 to 2001 the temperature PC1 correlation with the NAO is significantly higher in winter (R^2=44%) than in summer (R^2=19%). From a number of studies [Slonosky and Yiou, 2001, Vinther et al., 2003] it is already known that the impact of the NAO on temperature variability is strong in the entire circum North Atlantic region. Next the same analysis for precipitation and $\delta^{18}O$ is repeated.

The precipitation EOF1 has a strong dipole structure over Greenland in winter, while the summer EOF1 has a structure more oriented towards a northwest-southeast pattern. However, as it will be discussed in the next section the summer EOF2 of precipitation strongly resembles the pattern of the winter EOF1. The running correlation in Figure 2.11 between the PC1 of winter precipitation and NAO shows that the correlation is negative for the entire period but only periodically significant with a marked shift to strongly significant negative correlation during the 1990s. The maximum winter loadings on PC1 in the western part of Greenland include NorthGRIP, Camp Century, and the new NEEM deep drilling sites.

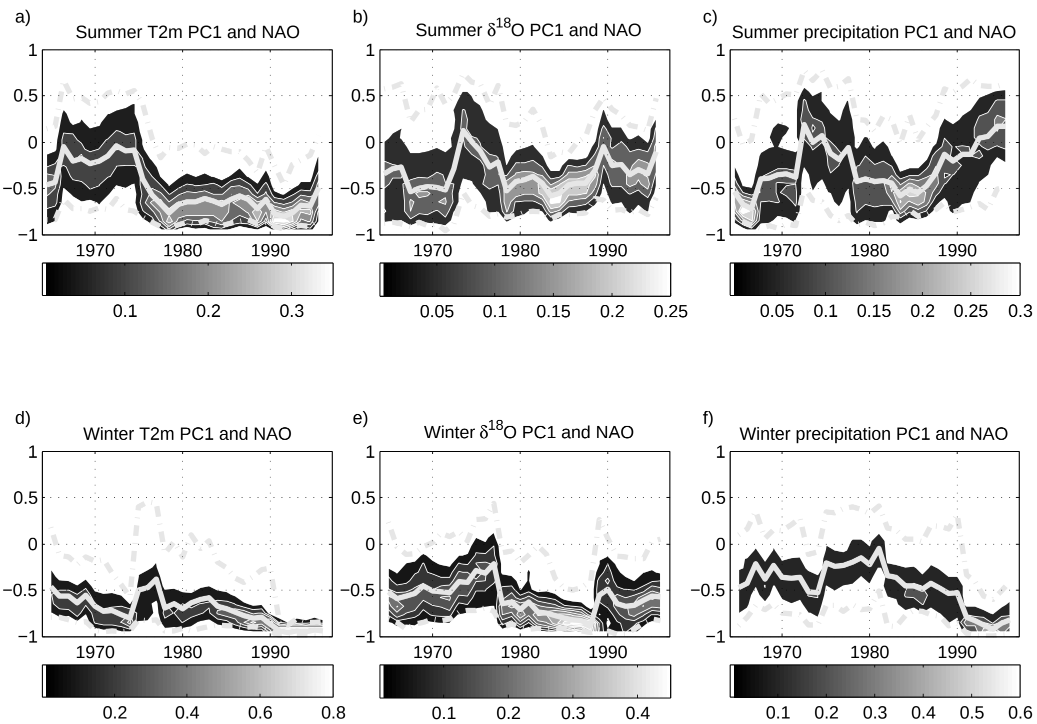

Figure 2.11: The 11 year running correlation (full grey line) between the seasonal mean NAO and the first PCs of seasonal temperature, δ^{18}O and precipitation. The significance of the correlation is estimated using bootstrap resampling [Efron, 1983] with 1000 samples for each collection of 11 data pairs (see also Appendix A.3). The contour shades give the density of the bootstrap correlation with the colorbar indicating the percentage of bootstrap correlations marked by the colours. Marked with the dash-dotted grey lines is the upper and lover limits of the 95% confidence intervals also calculated using the bootstrap method.

As for the case of temperature and precipitation the winter PC1 of δ^{18}O is negatively correlated with NAO during the whole model run (see Figure 2.11e). The shift in correlation for δ^{18}O towards more negative values in the late 1970s coincides with the shift for the temperature PC1 ending the brief period of weak correlations. Other than this shift, the PC1 of temperature,

δ^{18}O and precipitation have little in common in terms of temporal changes in the running correlation with the NAO.
The water isotopes are locally affected by both temperature and precipitation. They are also controlled by the same circulation patterns as these two climate parameters. In fact the winter EOF1 for δ^{18}O resembles the EOF1 of the temperature, but with a less broad maximum in central Greenland, slightly shifted to the west. The pattern explains 31% of the isotope variability. In the eastern part of Greenland the loadings are weak, and locally even negative. The simulated isotope EOF1 (summer and winter) next to the ice core drilling site Renland for instance (see Figure 2.10b and 2.10e), has little common variability with the central Greenland sites such as GRIP and NorthGRIP. This loss of common variability between Renland and the Central Greenland isotope records is supported by a similar study based on ice core data [Vinther et al., 2008].
In general the water isotopes follow the temperature signal, which is in agreement with the classical temperature effect in high latitudes. However, in western Greenland the isotope signal seems to be reinforced by the positive precipitation anomalies, while in eastern Greenland the negative part of the precipitation dipole pattern attenuates the isotope pattern. This effect of the precipitation could be due to the precipitation weighting of the isotopes on a sub seasonal timescale.
Sodemann et al. [2008b] did a back trajectory study based on the ERA-40 reanalysis, which demonstrated the differences in cyclone tracks for Greenland under positive and negative phase of the NAO during winter. The authors showed that during the positive phase the cyclones will enter Greenland from the east, while the preferred trajectory for the negative phase is entering the ice sheet from the south-southwest.
This change of the distillation path, the dipole pattern in precipitation and the uniform temperature variability is probably the explanation for the EOF1 pattern of the winter δ^{18}O. For the negative phase of the NAO the temperature will have uniform warm anomalies over most of Greenland, while the precipitation will have positive anomalies in the west and negative anomalies in the east. The opposite sign of the temperature and precipitation anomalies in east Greenland could, due to precipitation weighting, lead to the attenuated variability for δ^{18}O seen in the EOF1.
In summary for the winter analysis: All three PC1 (temperature, water isotopes and precipitation) are clearly correlated to each other (R$\sim$0.7). The reason for this common variability is in fact the NAO to which all three are negatively correlated (see Figure 2.10d, 2.10e, 2.10f and Table 2.2). Basically, when the NAO is in its negative phase Greenland enters into a warm mode with a dipole precipitation pattern. Influenced by both temperature

and precipitation the water isotopes show a mixed signal. The NAO explains about 44% of the temperature PC1, 25% of the precipitation PC1 and 21% of the water isotope PC1 during winter for the period 1959 to 2001. The results for the PCA are summarized in Table 2.2.
In a study by Vinther et al. [2003] the authors did a PCA of the isotopic winter signal in 7 Greenland ice cores. The study showed a correlation between the NAO and the PC1 for the ice cores of R=-0.51 (R^2=0.26) for the period 1824 to 1970. The authors also performed a running correlation, using a 30 year window, which showed varying correlations between ~ R=-0.3 to R=-0.6. The limited overlap between the time period for the $REMO_{iso}$ experiment and the ice core study, does not allow for a direct comparison of the two. However, the temporal variations of the correlation between $\delta^{18}O$ and NAO is very similar in the study of Vinther et al. and the analysis shown here. The correlation for the period 1959 to 2001 $REMO_{iso}$ is R^2=0.21 for the PC1 winter $\delta^{18}O$, as also stated in the paragraph above, which it is slightly lower than the R^2=0.26 from the ice core study (1824 to 1970). This could be due to the variations in the relation between the $\delta^{18}O$ and the NAO found both in the model output and for the ice cores. However, the data selection of for the PCA is also a factor, and it could be important for the analysis that the model covers the entire ice sheet, while the ice core study only has 7 ice cores from east, vest, south and central Greenland.
For summer temperature and $\delta^{18}O$ the EOF1s exhibits similar spatial pattern as the winter patterns albeit more noisy. For temperature weaker loadings are apparent along the west coast and in the south compared to winter, while the loadings are more positive in the northeast. This pattern explains 58% of the variability. As for winter the PC1 of summer temperature is correlated to the NAO, but the correlation can only be said to be significant for the period after the late 1970s (see Figure 8d).
The EOF1 for $\delta^{18}O$ shows clearly negative loadings around and north of Renland. Compared to winter there is a regional maximum for the loading west of summit, and the loadings south of DYE3 are stronger. This pattern explains 25% of the variability. Also for summer $\delta^{18}O$ the PC1 is negatively correlated with NAO with an increase in significance for the period from the late 1970s to 1990 similarly the winter $\delta^{18}O$.
The EOF1 pattern for precipitation found in winter is no longer the primary mode of variability during summer. The EOF1 for summer is northwest-southeast oriented with the largest area of negative loadings towards the south. This pattern explains 31% of the variability. However, as mentioned above the EOF2 (explaining 19% of the variability, EOF2 not shown) of summer precipitation strongly resembles the EOF1 of winter precipitation. This means that the main variability pattern of the winter still exists during

summer, but is of less importance to the total variability. Furthermore the PC2 of summer precipitation does show negative correlations with the NAO, but only significant for the last half of the model run (not shown). The correlation between the first PC of summer temperature and summer δ^{18}O is R=0.6, while the PC1 of summer precipitation is not significantly correlated to either of the other first PCs.

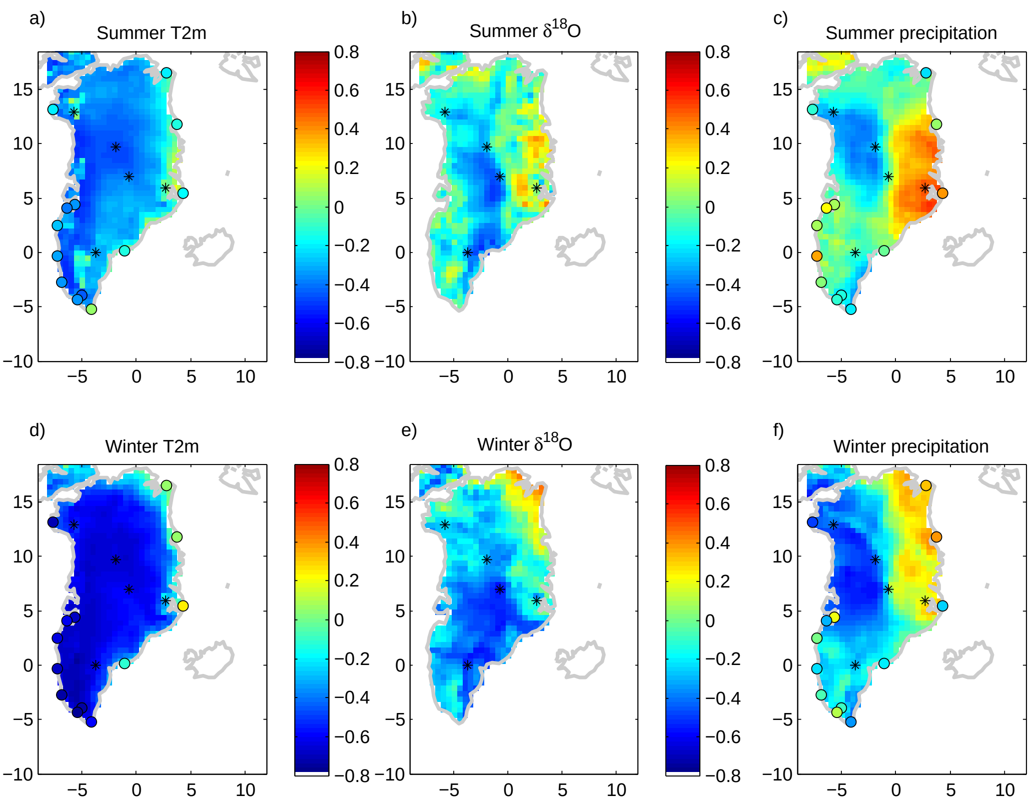

Figure 2.12: Pointwise correlation maps between the seasonal mean NAO and the modeled summer (upper) and winter (lower) temperature, δ^{18}O and precipitation. The coloured dots in the temperature and precipitation maps indicate the correlation between observations and the seasonal mean NAO.

The influence of the NAO is still significant during summer and the common variance with PC1 for temperature is 19%, with PC1 for δ^{18}O 12% and with PC2 for precipitation 10%, which is considerably less than the results for the winter season.

The differences between the results for the summer and winter PCA clearly shows that winter variability indeed is a result of the constraints of large scale circulation, while the summer variability is less structured more influenced

by spurious local events (as also found in Section 2.1.4).
The PCA is very instructive to identify the leading modes of variability. A direct comparison of this highly condensed gridded information with the relative few point measurements remains difficult. The pointwise regression of temperature, δ^{18}O and precipitation with the NAO was therefore calculated, and the results for temperature and precipitation were compared with the correlation between the NAO and the coastal observations by DMI (see Figure 2.12). These results confirm the important role of the NAO for the considered climate variables, and gives additional confidence in the model's capacity to reproduce the influence of the circulation both on the principal climate parameters and on the most important proxy quantity. On one hand there is a striking resemblance between the correlation pattern in Figure 2.12 and the corresponding PC1 (Figure 2.10). This is of course to be expected since in particular the NAO related (see Figure 2.11) temperature PC1 explains a very large part of the inter-annual variability. On the other hand, the comparison with the meteorological data (colored dots in Figure 2.12) gives strong empirical support for the computed NAO correlation pattern.
For both climatological variables (P and T) higher correlation during winter time than during summer is found again, which is in agreement with the concept of the NAO principally as a winter pattern. The dipole pattern in precipitation with positive precipitation anomalies in Western Greenland associated with a low NAO phase and negative anomalies in Eastern Greenland is in fact reproduced by the model. Also, and very surprisingly, the small band of low and disappearing correlation between temperature and NAO on Greenland's East coast is in fact confirmed by the meteorological observations (see Figure 2.12 a and d). The role of the NAO for Greenland will be discussed further in Section 2.2.

2.1.6 Summary

The regional climate model REMO$_{iso}$ was run over a 44 year period forced by the SSTs and the upper level wind field from the ERA-40 reanalysis. The lateral boundary conditions for all prognostic variables was supplied by the global model ECHAM$_{iso}$, which was forced by the ERA-40 reanalysis in a similar manner as the regional model. The domain of the regional model covers Greenland and the northern part of the Atlantic.
The model was found to reproduces the mean annual temperature patterns well, except for a warm bias over central Greenland of about 5^oC. The warm bias was found to be greatest during summer, and therefore thought to be linked to a too low surface albedo. Other possible causes was mentioned to be misrepresentation of the boundary layer temperature inversion or biases

introduced by the reanalysis or ECHAM$_{iso}$.
For precipitation the model was found to have a wet bias for the coastal regions, while the central ice sheet was too dry. However, the model was reported to reproduce the east-east contrast in the annual cycle of precipitation very well, as well as the over all accumulation pattern of the Greenland Ice Sheet. Compared to ice core data the model was found to have a bias in δ^{18}O of +4.4‰. As for temperature the bias was most pronounced during summer. The spatial slope between temperature and δ^{18}O was found to be well reproduced, despite the biases found in temperature and δ^{18}O.
A study of the seasonal variability was carried out for temperature, δ^{18}O and precipitation, where the REMO$_{iso}$ output was compared to coastal observation and ice core data. For temperature the model was found to reproduce the winter variability very well, while less so during summer. This was explained by the fact that winter variability is to a larger extend controlled by large scale variability, which the model was forced to follow. Additionally the winter variability is larger than the summer variability for temperature, which also should be taken into account as a larger signal is easier for the model to capture.
The precipitation variability was not captured as well as for temperature, and the contrast between the performance during summer and winter was also less pronounced.
In comparison with ice core data significant correlation in δ^{18}O was found during summer for the DYE3 site and during winter for GRIP. It was speculated that the uncertainties in the dating of the ice cores could have introduces errors that degraded the correlation. REMO$_{iso}$ was also compared to observed δ^{18}O from Reykjavik and was found to match the winter data quite well, while no correlation was found for summer data. Due to the short data series the match for winter data was not significant.
As a last part of this chapter a Principal Component Analysis was carried out for the seasonal mean temperature, δ^{18}O and precipitation. The first principal components (PCs) for winter temperature, δ^{18}O and precipitation were found to be periodically correlated with the NAO, with the strongest connection found for temperature. During summer the correlation of the PCs with NAO was found to be much less pronounced. The correlation of the NAO was further verified through comparison with observed temperature and precipitation.
This study underlines the importance of the fundamentally different seasonal variability regimes that governs the Greenland climate, as well as the usefulness of regional models in modeling of the isotopic of precipitation.

2.2 The climate variability over Greenland and the NAO

The North Atlantic Oscillation (NAO) is generally viewed as a winter signal. This is explored further here, where details on the significance of the NAO for Greenland will be shown dealing with both modeled data and observations. The analyses in this section are based on the same model experiment and observations as presented in Section 2.1.1 and 2.1.2, and the focus here will be to elaborate on the subjects of the NAO and climate variability.

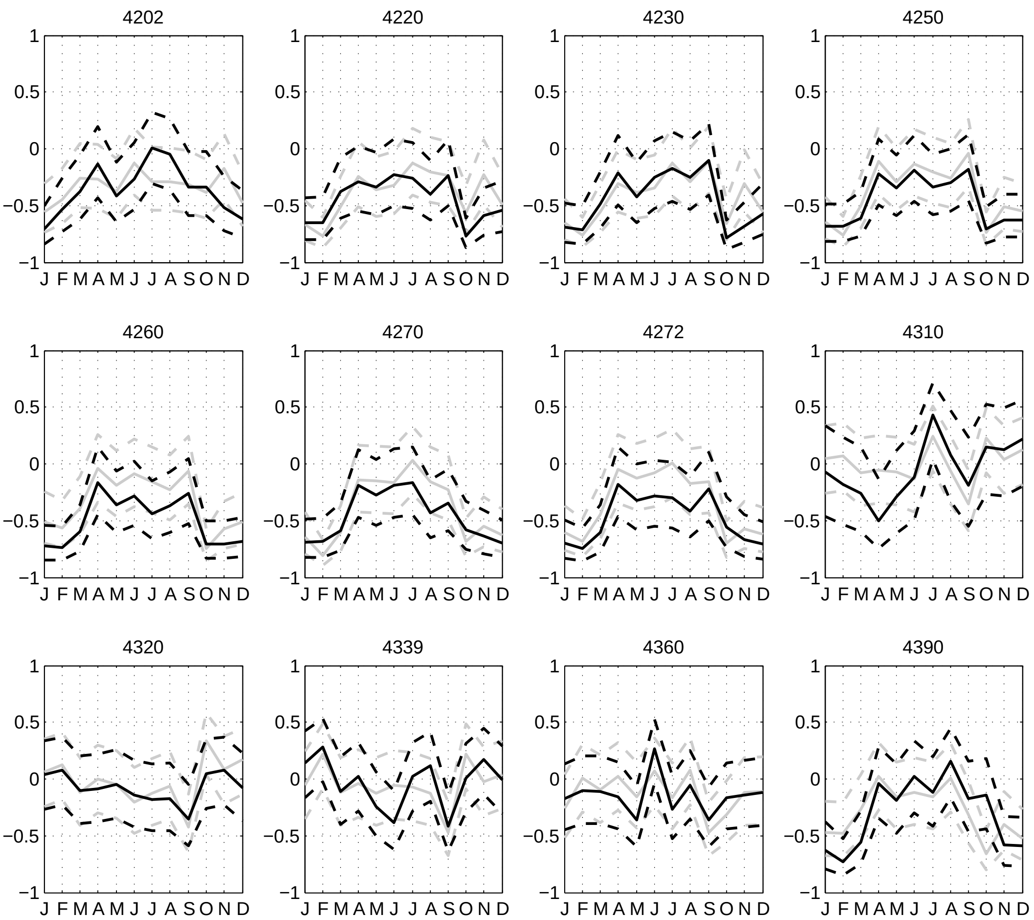

Figure 2.13: Modeled (light gray) and observed (black) monthly correlations between T2m and NAO for coastal stations. The dashed lines mark the upper and lower limit of the 95% confidence interval.

In Section 2.1 only seasonal data was analyzed in relation to the NAO, using the summer/winter definition dictated by the seasonal ice core data. The plots of the monthly correlations in Figure 2.13 shows that the view of NAO as a winter signal can indeed be justified for temperature. For stations on the west coast (Station 4202 to 4272) and to the south (Station 4390) a significant correlation is in general found for the months October to April, which does not perfectly match the winter definition of November to April, but the one month difference does not alter the general picture. The shift in monthly correlations happens quite markedly around March/April and September/October.

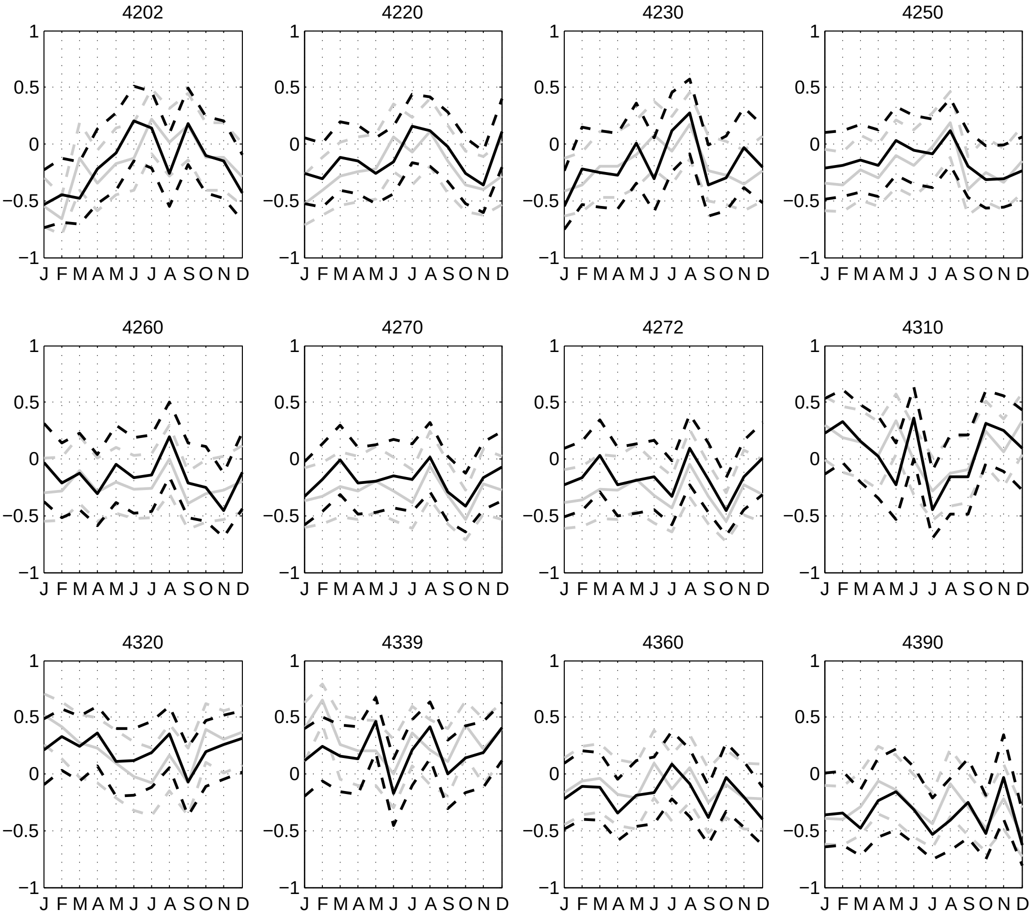

Figure 2.14: Modeled (light gray) and observed (black) monthly correlations between precipitation and NAO for coastal stations. The dashed lines mark the upper and lower limit of the 95% confidence interval.

In general the correlation coefficients goes from $R \sim -0.7$ during winter

to $R \sim -0.2$ during summer, with the summer values only being marginally significant. The strength and abruptness in the shift of correlation coefficients underlines the fundamentally different variability regimes in two seasons. Also to be noted is that the model correlations between temperature and NAO is very close to the observed, both regarding the timing of the shifts in correlation and the correlation levels.
From Figure 2.14 it is seen that the relation between precipitation and NAO is not as clear as it is for temperature. The first thing is the tendency for a east-west dipole pattern with station 4202 to 4250 showing negative winter correlations ($R \sim -0.5$) and station 4310 to 4339 showing positive winter correlations ($R \sim 0.3$). Secondly, the shift between summer and winter correlations is not very clear and does not cover as many stations as for temperature. Also, some stations do not show the same kind of summer-winter contrast that has been discussed here, that is there is no clear seasonal cycle in the correlation relation to the NAO. For example station 4390 has periods of significant correlations with $R \sim -0.5$ during both summer and winter.

Seasonal correlation between REMO$_{iso}$ temperature, δ^{18}O, precipitation and the NAO

The data displayed in this section is the same as in Figure 2.12 (see Section 2.1), with the exception that the values where $p>0.05$ has been masked out. In this way the significance of the correlation patterns is more clear while the connection with the observations is better seen in Figure 2.12.
The seasonal correlation patterns for temperature tells the same story as shown in Figure 2.13 for the monthly data, with the exception of the extra spatial information from the modeled data. The negative correlation between NAO and temperature extends to most of Greenland with the exception of the eastern coast line. For the summer δ^{18}O the areas of significant correlation are confined to a streak in the central and southern central Greenland, while the winter pattern is broader for the southern half of Greenland including the area around the GRIP drilling site.
The most marked shift in correlation pattern between summer and winter is seen for precipitation. The east-west dipole maintained during summer largely disappears during winter, with only scattered positive correlations to the east. The seasonal shift is supported by the observed correlation patterns.
As also discussed in Section 2.1.5 the cyclone tracks will during winter enter Greenland from the east when the NAO is in the positive phase, and predominantly from south-southwest for the negative phase [Sodemann et al.,

2008b]. However, there is also a certain frequency of cyclones from the east in the NAO negative phase. This could explain why it is mainly the western part of Greenland that is sensitive to the NAO, as cyclones will pass east Greenland during both the positive and negative phase of the NAO. Sodemann et al. [2008b] did not study the storm tracks during summer, so for the moment it is inconclusive what drives the shift in the correlation patterns from summer to winter.

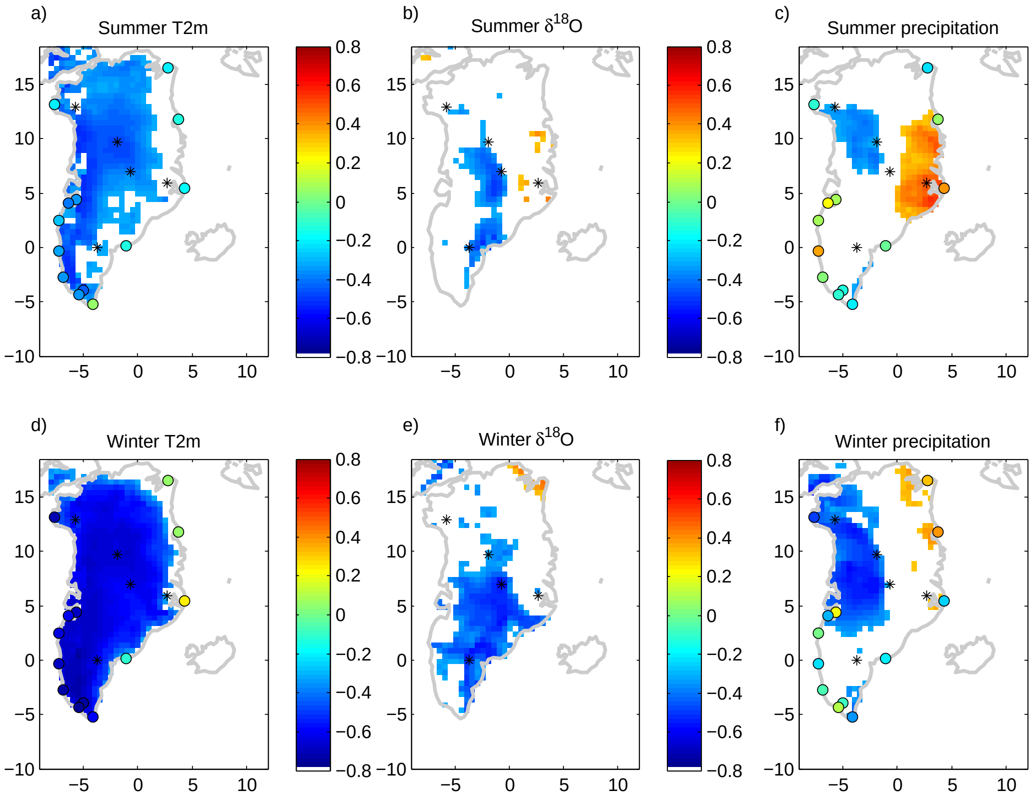

Figure 2.15: NAO point correlation maps for modeled summer (upper) and winter (lower) temperature, δ^{18}O and precipitation. The coloured dots in the temperature and precipitation maps indicate the correlation between observations and the NAO. All correlations with p>0.05 has been masked out.

In another study Sodemann et al. [2008a] included isotope diagnostics in a back trajectory analysis based on 30 winter months from the ERA-40 reanalysis. Here the authors found the δ^{18}O values to be lower (by 3.8‰ in average) during the positive phase of the NAO compared to the negative phase. That is, essentially the Greenland δ^{18}O was found to be negatively correlated to the NAO. The largest sensitivity was found to by from the central to the southern part of Greenland. This is in agreement with correlation pattern in Figure 2.15e. Sodemann et al. found the δ^{18}O correlation with the NAO to be caused equally by temperature, which is also negatively correlated with the NAO, and shifts in source conditions, with higher source temperatures during negative NAO.

2.2.1 The connection between variability of REMO$_{iso}$ temperature, δ^{18}O and precipitation

In the previous two sections, as well as in Section 2.1, the variability of temperature, δ^{18}O and precipitation was investigated in relation to the NAO. From Section 2.1 the conclusion was that the δ^{18}O was a mixed signal, not surprisingly, influenced by both temperature and precipitation. To begin with a correlation analysis between temperature, δ^{18}O and precipitation is carried out using monthly data to investigate the spatial pattern of the modeled common variability between these three parameters. To better reflect the correlation of short term variability, and not simply similarities in annual cycle, the mean annual cycle has been subtracted from the data before calculating the correlation.

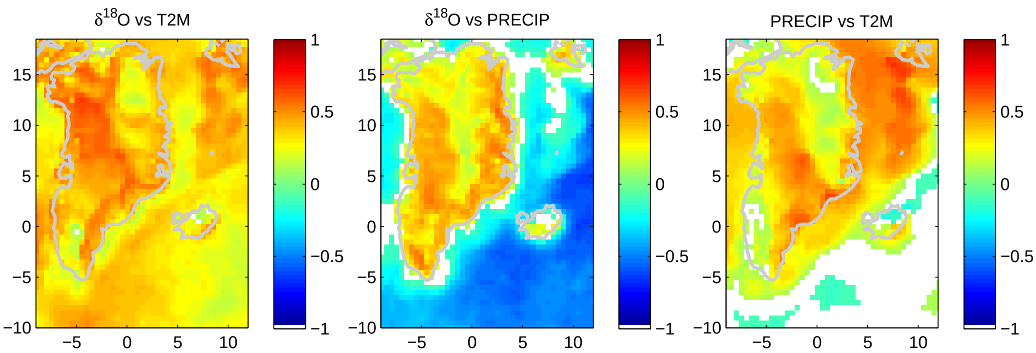

Figure 2.16: Correlation maps for the monthly δ^{18}O, T2m and precipitation anomalies, where the mean annual cycle has been removed and values where p>0.05 has been masked out.

In Figure 2.16 the results of this correlation analysis are displayed. All three maps show large regional differences in correlation levels. The main conclusion from the correlation patterns is, that the correlation between monthly anomalies in temperature and δ^{18}O is greatest in areas where temperature and precipitation also are highly correlated. This means that the

temperature correlation with δ^{18}O is strongest where the basic assumption of Rayleigh-distillation processes holds, namely that colder temperatures equals drier conditions.
A similar correlation analysis has been carried out for the mean seasonal data. From Figure 2.17 it is seen that the correlation patterns for the monthly anomalies are dominated by the winter correlation. Furthermore, when comparing with the pattern of loadings on the winter EOF1 for δ^{18}O shown in Figure 2.10, there is an overlap between this and the winter temperature-precipitation correlation pattern. Areas of no significant correlation in the southern and in the northeastern part of Greenland both coincide with areas which have low loading on the winter δ^{18}O EOF1. While the overlap is not complete, this does provide the insight that the areas where the temperature-precipitation correlation is low also lie outside the domain of the main δ^{18}O variability pattern.

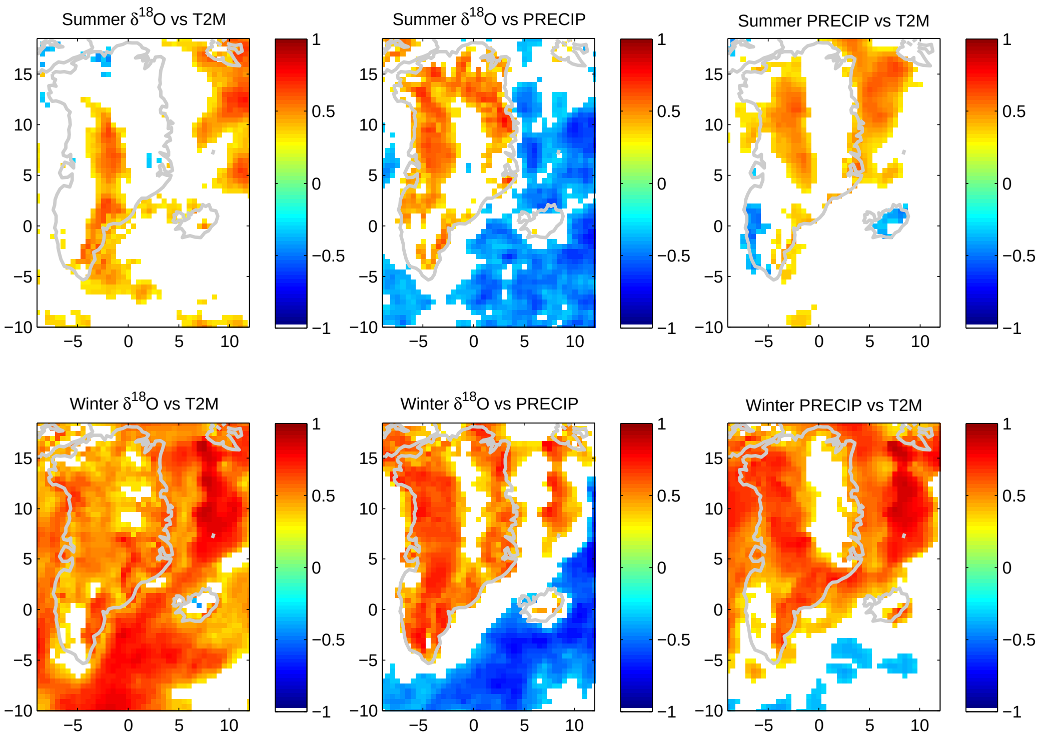

Figure 2.17: Correlation maps for the seasonal mean δ^{18}O, T2m and precipitation, where grid points with values of $p>0.05$ has been masked out.

The standard deviation of seasonal means for temperature, δ^{18}O and precipitation

In previous section the connection between temperature and precipitation anomalies was mentioned with the Rayleigh-distillation as an example. Physically the connection between higher temperatures and more precipitation can be explained by the Clausius-Clapeyron relation. If we assume that the precipitation anomalies are proportional to the temperature anomalies, then the temperature-precipitation correlation will be strongest where the variance of the temperature is highest. This is true under the assumption that a background noise level will cloud the correlation in areas where the temperature variance is low (see also the example in Appendix A.4).
To go further into this, as well as exploring the seasonal differences in variability, the summer and winter standard deviation of the REMO$_{iso}$ T2m, δ^{18}O and precipitation is calculated.

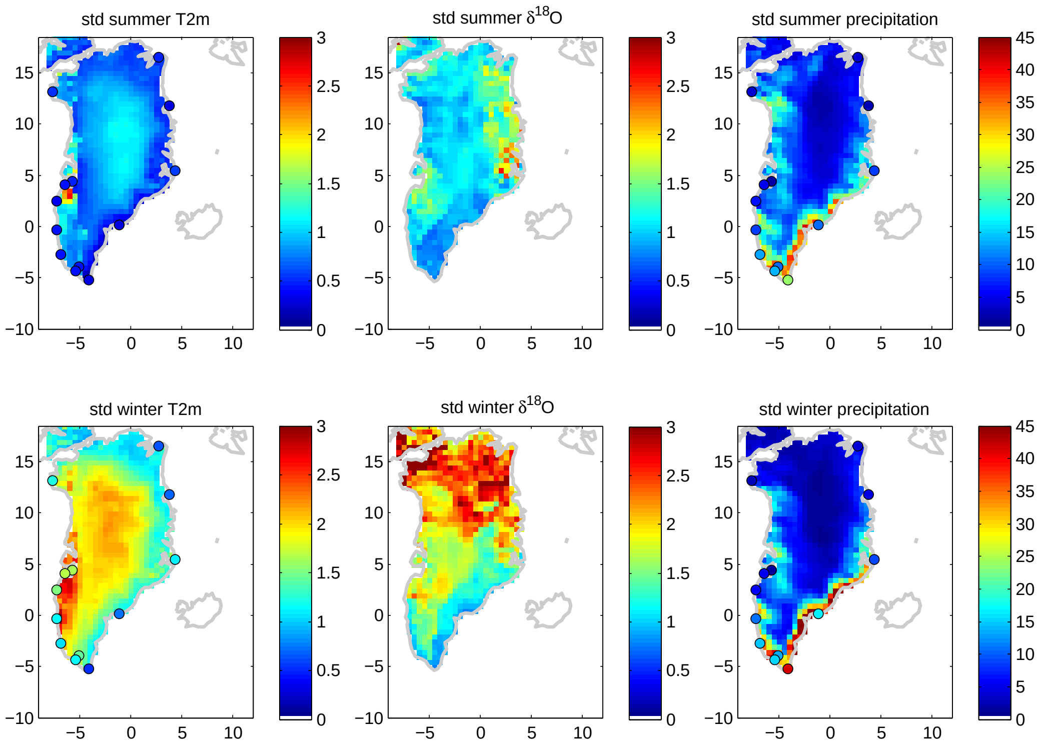

Figure 2.18: The summer standard deviation (upper panel) and the winter standard deviation (lower panel) for T2m [^oC], δ^{18}O [‰] and precipitation [mm/month]. For temperature and precipitation coastal observational data in included and marked by the colored dots.

It can be seen from Figure 2.18 that the modeled spatial patterns for the standard deviation of T2m, δ^{18}O and precipitation are distinctly different. The effect of larger inland variability can be seen for both summer and winter temperature, while the low variability of the winter temperature along the east Greenland coast could be related to the persistent flux of sea ice carried by the East Greenland Current [Rudels et al., 1999]. The δ^{18}O variability pattern cannot be said to strongly resemble either the temperature pattern or the precipitation pattern, although the δ^{18}O pattern does loosely follow the temperature pattern in southern Greenland during winter. For precipitation the pattern is strongly related to the amount of precipitation, and the variability pattern is very close to the REMO$_{iso}$ accumulation map shown in Figure 2.4.

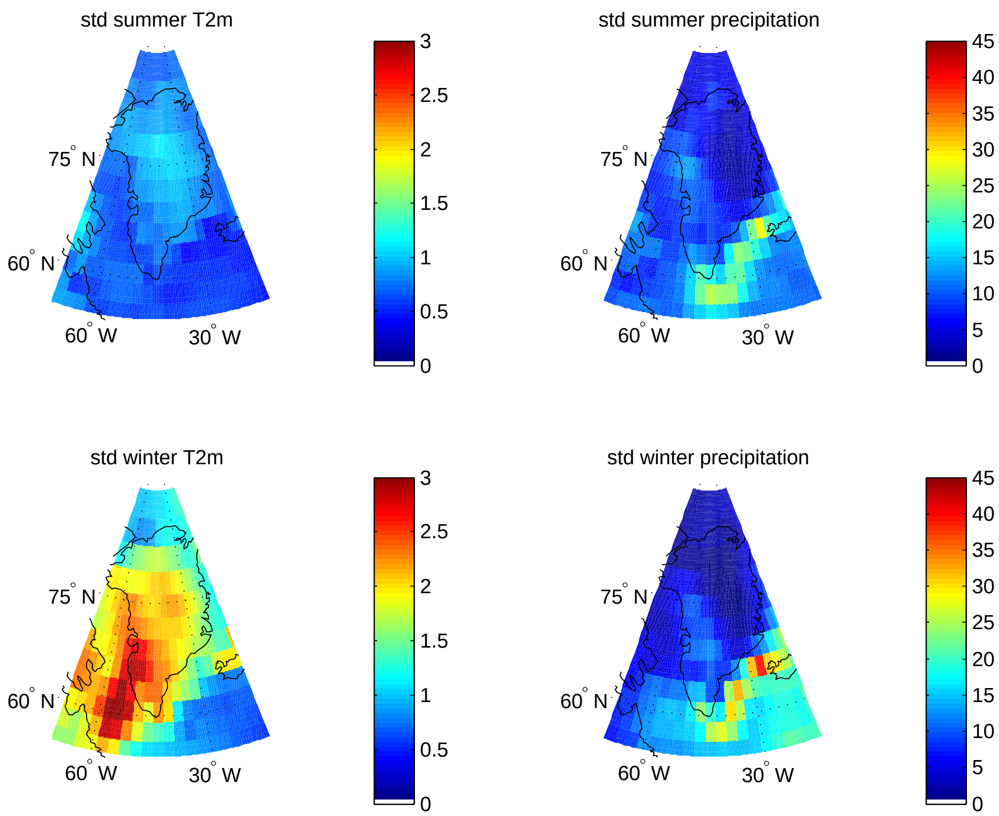

Figure 2.19: The ERA-40 summer standard deviation (upper panel) and the winter standard deviation (lower panel) for T2m [^oC] and precipitation [mm/month]. The data is in T42 resolution and is available on the ECMWF website (http://www.ecmwf.int/research/era/do/get/era-40).

In relation to the discussion in the beginning of this section, then the pattern of the summer and winter temperature variability does not explain the correlation pattern between temperature and precipitation shown in Figure 2.17. This means that at least on a seasonal time scale the temperature-precipitation correlation is not mainly controlled by a simple thermodynamic relation between these two parameters.
The strong δ^{18}O winter variability in the northern part of Greenland could be related to a lack of winter precipitation in this area (winter/summer precipitation is shown later in Figure 2.21). The lack of winter precipitation means that the δ^{18}O signal will be based on a few precipitation events, with a large scatter between the individual events. However, a detailed study on sub monthly time scale is needed to quantify this properly.
There is a qualitative match between the observed and modeled standard deviations for temperature and precipitation both shown in Figure 2.18. Overall it looks like the model overestimates the standard deviation, in particular for the west coast temperature and the east coast precipitation.
As described in Section 2.1.1 the REMO$_{iso}$ is nudged to follow the circulation of the ERA-40 reanalysis. In Figure 2.19 the standard deviation of the ERA-40 temperature and precipitation is plotted for comparison. The summer and winter temperature variability pattern is very similar in ERA-40 and REMO$_{iso}$, both with respect to magnitude and spatial distribution. For precipitation the variability patterns for REMO$_{iso}$ and ERA-40 are also quite similar. The higher resolution of the REMO$_{iso}$ is more apparent for precipitation, and the spatial and temporal variability is stronger than for ERA-40.

Winter versus summer variability

The different nature of the variability during summer and winter has been mentioned numerous times so far in this study, not only in relation to the NAO, but in general terms as well. As it already can be seen in Figure 2.18, there are differences in both the pattern and magnitude between the summer and winter variability, especially for temperature and δ^{18}O.
In general the standard deviation for temperature is about twice as large during winter compared to summer (see Figure 2.20). This is fairly uniform all over Greenland. While the variability for δ^{18}O also is greater for winter than for summer there is a big north-south gradient, mainly because of the north-south difference in winter variability. For precipitation the picture is somewhat turned with the summer variability being larger than the winter variability, in particular for central and northern Greenland. The only place where larger winter than summer precipitation variability can be found is for some coastal areas, as for example the southeastern coast.

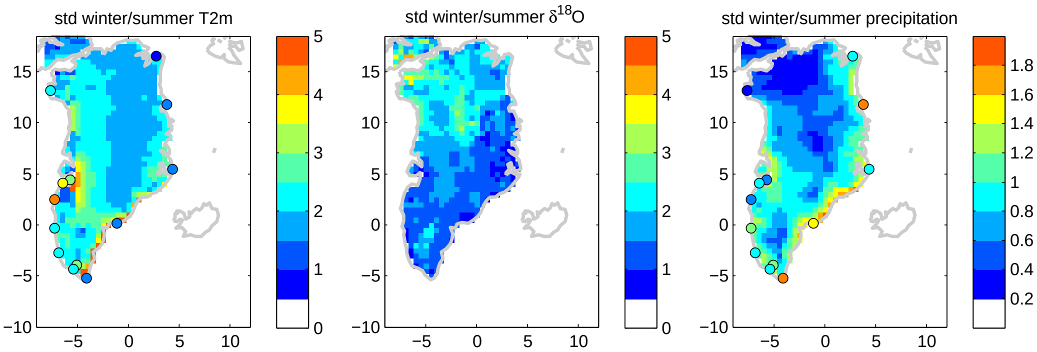

Figure 2.20: The winter standard deviation divided by the summer standard deviation for T2m, δ^{18}O and precipitation. For temperature and precipitation coastal observational data in included and marked by the colored dots. Note that the scale for precipitation is different from the scale for T2m and δ^{18}O.

It was found in connection with Figure 2.18 that the standard deviation of the precipitation was basically proportional to the amount of precipitation. This also explains the winter/summer pattern for the standard deviation of precipitation. The mean winter precipitation divided by the mean summer precipitation is plotted in Figure 2.21. It is evident that the winter/summer standard deviation resembles this figure.
There is a fairly good agreement between the coastal data and the model output in Figure 2.21. For sites on the ice sheet not many observations of

the annual cycle of precipitation exits. However, Shuman et al. [1995] reported and approximately equal amount of summer and winter precipitation for Summit. This agrees with the modeled winter/Summer ration found here. The winter versus summer precipitation ratio of precipitation is also interesting from an isotopic view point, as changes in this ration due to climate changes will bias the annual mean isotope signal as recorded by ice cores. Changes in the seasonality of precipitation has in a modeling study by Werner et al. [2000] been pointed out, as being important for the isotope thermometer in connection with glacial-interglacial climate shifts.

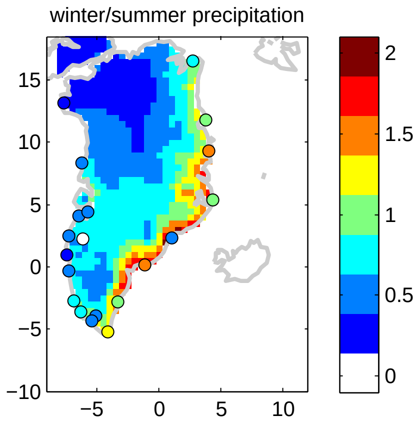

Figure 2.21: The modeled winter precipitation divided by the summer precipitation. Coastal observational data in included and marked by the colored dots. Also coastal stations with only climatological mean annual cycle available are included in the plot.

2.2.2 Summary

In this section further details on the role of the NAO for Greenland and general variability of temperature, δ^{18}O and precipitation was investigated in relation to the findings in Section 2.1. The seasonal imprint on observed and modeled temperature and precipitation was investigated. In agreement with the observations the model showed a strong seasonality in the correlation with the NAO for temperature, where the winter months were found to be strongly influenced by the NAO for western and southern regions. For precipitation a less clear seasonality was found. However, for regions covered by the east-west NAO dipole pattern (for details see Figure 2.10, 2.12 and 2.17) stronger influence during winter is indeed seen. This confirms the role of the

NAO as primarily being a winter signal. Further more the significance of the spatial correlation patterns of NAO and temperature, δ^{18}O and precipitation was discussed. One result was that the correlation of δ^{18}O and NAO was found to be most important for southern Greenland during winter.
The correlation patterns between modeled monthly and seasonal temperature, δ^{18}O and precipitation were also calculated. Temperature and δ^{18}O was found to be most correlated for areas where temperature and precipitation was correlated. This correlation pattern over laps with the EOF1 of δ^{18}O shown in Figure 2.10. The correlation was found to be higher for winter time. In connection with the correlation analysis a study of the magnitude of the seasonal variability was made by calculating the seasonal standard deviation. For temperature and δ^{18}O the variability was found to be significantly larger during winter, while for precipitation winter variability was only larger for some coastal areas. This is in agreement with observations. The variability of seasonal temperature and precipitation was found to be quite similar to the variability of the ERA-40 data set, with more detailed regional patterns due to the higher resolution of the REMO_{iso} output.

2.3 Modeling the Greenland d-excess with REMO$_{iso}$

The second order stable water isotope parameter the deuterium excess, hereafter simply d-excess, is widely used in isotope glaciology as an indicator of moisture source conditions [Johnsen et al., 1989, Masson-Delmotte et al., 2005, Steffensen et al., 2008]. The d-excess is defined by Dansgaard [1964] as

$$\text{d-excess} = \delta\text{D} - 8\delta^{18}\text{O} \tag{2.1}$$

and the value of the d-excess depends strongly on non-equilibrium fractionation during phase changes in the water cycle. The definition of the d-excess has its origins in the observed relation between δD and δ^{18}O, known as the Global Meteoric Water Line (GMWL), which is was defined by Craig [1961] as

$$\delta\text{D} = 8\delta^{18}\text{O} + 10 \tag{2.2}$$

The d-excess is a measure of how much a sample deviates from the GMWL, with the standard d-excess value being 10‰.

The non-equilibrium fractionation, or kinetic fractionation, during evaporation was investigated by Craig and Gordon [1965], Merlivat and Jouzel [1979] and it depends on the relative humidity in the boundary layer over the evaporation site. The link to the source temperature is caused by the temperature dependence of the equilibrium fractionation factors. It can be difficult to separate the temperature effect from the effect of the relative humidity, which is one of the problems that makes the d-excess hard to interpret.

It should be mentioned that the dependence on source conditions mentioned above rely on the closure assumption for water vapor (see also Section 1.4). This closure assumption is often used for initializing simple Rayleigh-type isotope models. According to Armengaud et al. [1998] this can lead to an underestimation of 3 to 4‰ in the d-excess. Armengaud et al. found that the simple models reproduced the d-excess of GCMs better when initialized with the temperature, relative humidity and isotopes from a GCM.

The second main kinetic effect happens during snow formation and it was described by Jouzel and Merlivat [1984]. It depends on the supersaturation in the cloud, and has strongest effect when dealing with low δ^{18}O values, that is under $\sim$ -30‰. The kinetic effect during snow formation increases the δD-δ^{18}O slope, which keeps the precipitation values closer to the GMWL, compared to pure Rayleigh distillation.

2.3.1 Mean temperatures, δ^{18}O and d-excess

As a first part of this d-excess modeling study the mean modeled d-excess is evaluated together with the modeled temperature and δ^{18}O for the Greenland area. The data used in this section is coastal data from IAEA/GNIP stations on Greenland, Iceland and Svalbard [IAEA, 2006], and data from the North Greenland Traverse [Fischer et al., 1998]. The locations of where the data was collected can be seen in Figure 2.22.

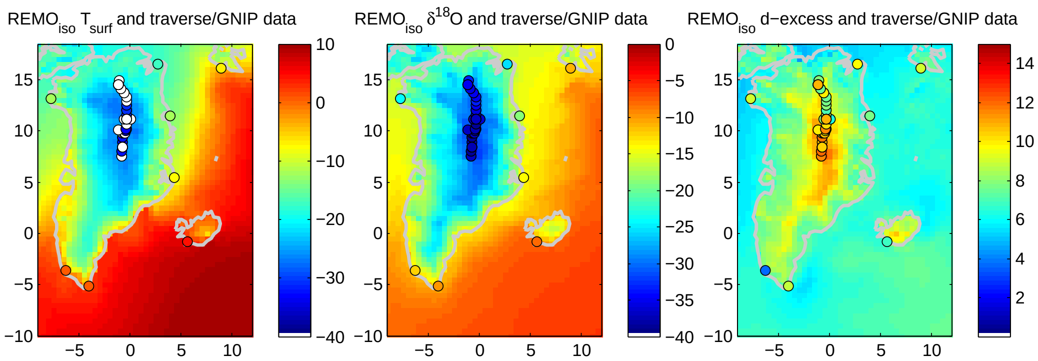

Figure 2.22: Modeled and measured annual mean surface temperature, δ^{18}O, and d-excess. The isotope values have been weighted with precipitation. Data for coastal IAEA/GNIP stations and for the North Greenland Traverse are marked with colored dots.

The GNIP and North Greenland Traverse δ^{18}O and temperature data was also presented in Section 2.1.3. This data is revisited here in greater detail in relation to the d-excess data.
In this section the warm bias ($\sim +5^oC$) for the center of the Greenland Ice Sheet (GIS) and the over estimated δ^{18}O values ($\sim +5‰$) has to be kept in mind.
In general the elevation of the inland traverse sites are too low in the model. For most sites the under estimation of elevation is about 100 meters, so in theory this can only account for 0.6-0.9^oC of the warm bias, which is the range of the temperature lapse rate per 100m depending on the relative moisture content of the air. However, when reviewing the correlation between temperature and elevation in the modeled traverse temperature data, the data only shows a R^2 of 0.26 for the 42 sites. This is because of the large latitudinal spread of the traverse data. The lapse rate calculated from the slope of these 42 points is 0.72^oC per 100m, which is in the range of the theoretical lapse rate.
As also mentioned in Section 2.1.3 the mean δ^{18}O values in southern Greenland and Iceland are well captured, while the model has trouble reaching the low values found to the north and in the center of the ice sheet. For

the traverse the elevation effect is dominating the gradient in δ^{18}O. Here the modeled elevation gradient is -0.39‰ per 100m, which is quite close the result for the traverse data (-0.34‰ per 100m).
The d-excess in the GNIP data is sparse and noisy, so this has to be kept in mind for the comparison. The modeled d-excess is relatively close to the observations at the southern GNIP sites. The exception is the very low d-excess found in the Prins Christians Havn (PRCH) observations, which is not matched by the model. This could very well be due to the mean PRCH d-excess being based on very few samples. In the northern parts the modeled levels are too low, which could be expected from the underestimated latitude effect in δ^{18}O, considering the inverse relation between d-excess and δ^{18}O found in polar regions. The relation between δ^{18}O and d-excess will be returned to when discussing Figure 2.23.
For the traverse data the model matches the levels quite well for the southern half of the traverse while the shift in data to the lower d-excess values of the northern half of the traverse is not captured by the model.

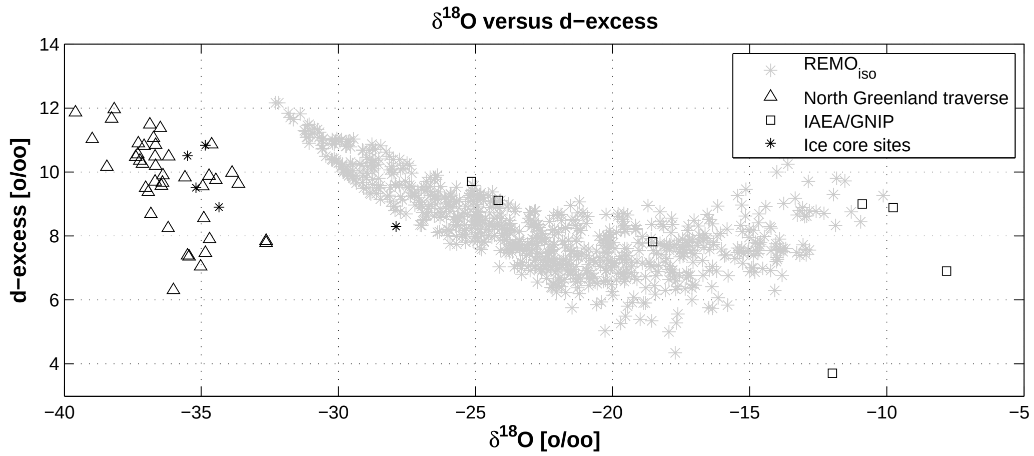

Figure 2.23: Modeled annual mean weighted δ^{18}O plotted against d-excess. Also plotted is observations from IAEA/GNIP, major ice core sites, and the North Greenland Traverse.

In Figure 2.23 the modeled mean annual d-excess has been plotted against δ^{18}O along with measured data from GNIP stations, ice core drilling sites and the North Greenland Traverse. The behavior of the model d-excess in relation to δ^{18}O for Greenland shows a decrease in d-excess for δ^{18}O values from -10‰ to -20‰ and an increase in d-excess for values lower than -20‰. For the δ^{18}O values lower than $\sim$ -20‰ the differences in the temperature dependent fractionation factors gives a decrease in the δD versus δ^{18}O slope which causes the d-excess to rise. This mechanism is dampened by the kinetic fractionation during snow formation, which diminishes the difference between the effective fractionation factors. The modeled δD-δ^{18}O slope for Greenland is indeed slightly lower than the observed (see Figure 2.24). The changing δD versus δ^{18}O slope for very depleted isotope levels, and its relation to d-excess, will be discussed further in Section 2.3.2.

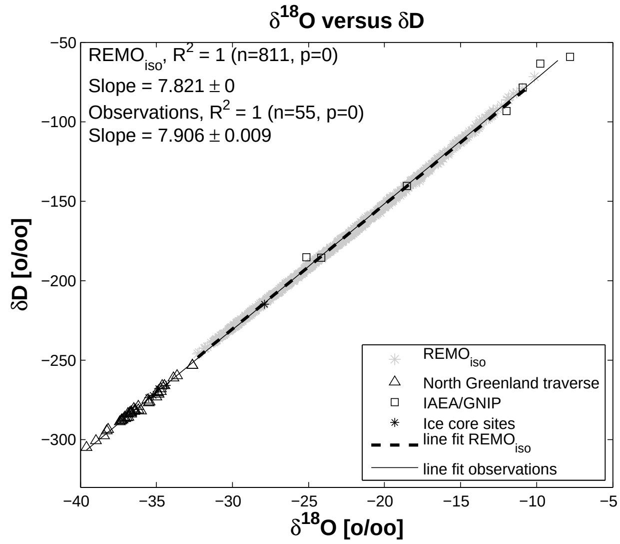

Figure 2.24: Modeled annual mean weighted δ^{18}O plotted against δD. Also plotted is observations from IAEA/GNIP, major ice core sites, and the North Greenland Traverse.

The data coverage of observations and ice core data is not good enough to reject or verify the over all d-excess versus δ^{18}O relation for Greenland, but a similar pattern of d-excess versus δ^{18}O has been found in observations for Antarctica [Petit et al., 1991, Masson-Delmotte et al., 2008]. For the most depleted modeled data the d-excess levels are as high as for the most depleted measured data, even though the modeled δ^{18}O does not reach the low levels of the traverse data. Clearly the model seems to over estimate the d-excess in relation to the δ^{18}O.

2.3.2 The d-excess annual cycle

The annual cycle of the d-excess from ice cores data has been used to identify the source area for precipitation at ice cores drilling sites [Johnsen et al., 1989]. The characteristic 3 month lag found in the ice core data is attributed to the thermal inertia of the ocean, which causes the annual cycle to be off set with three months due to the dependence of the d-excess on conditions in the the source area. As it also will be shown here this is not seen in the coastal sites, even in the Arctic.

Comparison with GNIP data

The observed data used in this section is from the IAEA/GNIP data base [IAEA, 2006]. In the course of this analysis it has been found that the noise level in some parts of this data is exceedingly high, especially when looking at the d-excess. Therefore it has been necessary to perform a selection of the data. Since it is difficult to reject the data on the basis of sampling procedure, as many of the measurements where done many years ago, the rejection of data must be done on statistical grounds. This is not optimal since many of the data series are short, and do therefore not offer solid statistics to base the rejection on. However, it is in this case the only sensible way of rejecting possibly faulty data.
The data is subjected to *Chauvenet's criterion*, which is a well established method that rejects suspect data based on the statistical properties, that is mean and standard deviation, of the time series in question [Taylor, 1997].
Figure 2.25 shows the modeled and measured mean annual cycle of the δ^{18}O for several meteorologic stations along the coast of Greenland and also from Reykjavik and Ny Ålesund. The measured data clearly has a larger standard deviation compared to the modeled data, and the annal cycle is not very clear for example at Ny Ålesund (nyal). For Thule (thul), Scorsbysund (scor) and Reykjavik (reyk) the model captures the δ^{18}O annual cycle quite well both with respect to levels and amplitude. For the largest data collection from Reykjavik the observations have a quite flat response during summer, which seem to be quite solid in the data. Compared to the observations the model has a more clear summer peak in July.
Compared to the δ^{18}O the GNIP d-excess is much more noisy. For example Grønnedahl (gron) and Station Nord (nord) have kinks in the annual cycle probably more due to measuring noise and sample treatment than anything else. However, in general it can be said that the d-excess cycle is in anti-phase with the δ^{18}O, both in the modeled and in the measured data. For some stations the model captures the d-excess cycle well, as it is the case

for Thule and Ny Ålesund. Reykjavik stands out as the location where the model best matches the measurements.

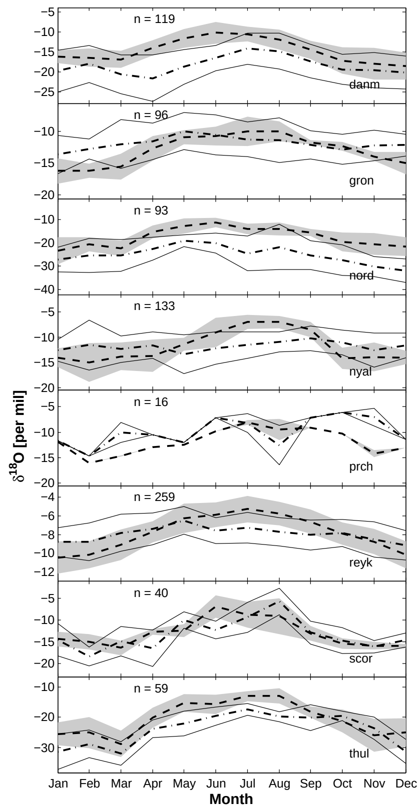

Figure 2.25: The mean annual cycle of δ^{18}O for GNIP data (dashed-dotted line with thin lines for one standard deviation) and modeled (dashed line with light gray shading for one standard deviation).

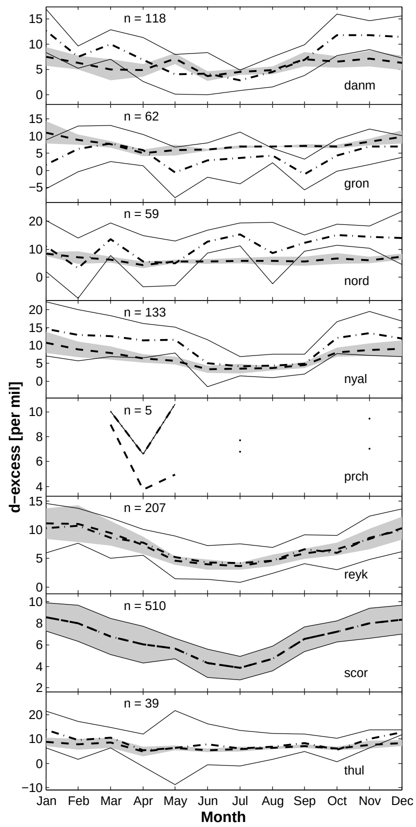

Figure 2.26: The the same as Figure 2.25, but for d-excess. For Scorsbysund (scor) only the modeled d-excess is plotted as no δD data exist.

The modeled annual cycle versus 'the three month lag'

The three month lag in the d-excess annual cycle compared to the δ^{18}O annual cycle found the Greenland ice cores is not found in the modeled d-excess for the ice core sites. Figure 2.27 is an attempt to map of the spatial variation in the d-excess annual cycle for Greenland. This is done by characterizing the annual cycle by only one number, namely the summer d-excess divided by the winter d-excess. By looking at areas with different summer/winter rations you get an idea how the d-excess annual cycle varies regionally. Sites in the central parts of the ice sheet have a summer/winter d-excess ratio of about 0.7. This results from a high excess during winter of about 15‰ with summer values around 8‰, as seen for Site # 2 in Figure 2.28. Regions on the slope of the ice sheet, between the coast and the interior of GIS, have a summer/winter d-excess ratio close to 1.2. These regions are characterised by a double peak in the annual cycle, with peaks in July-August and December-January and maximum values around 8‰ for both peaks. This can be seen in Figure 2.28 for Site # 1, 3, 4, 6 and 8.

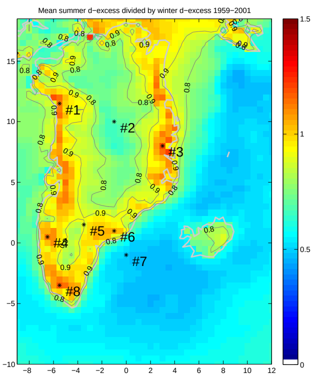

Figure 2.27: Mean summer d-excess divided by mean winter d-excess, with contour lines for values of 0.8 and 0.9.

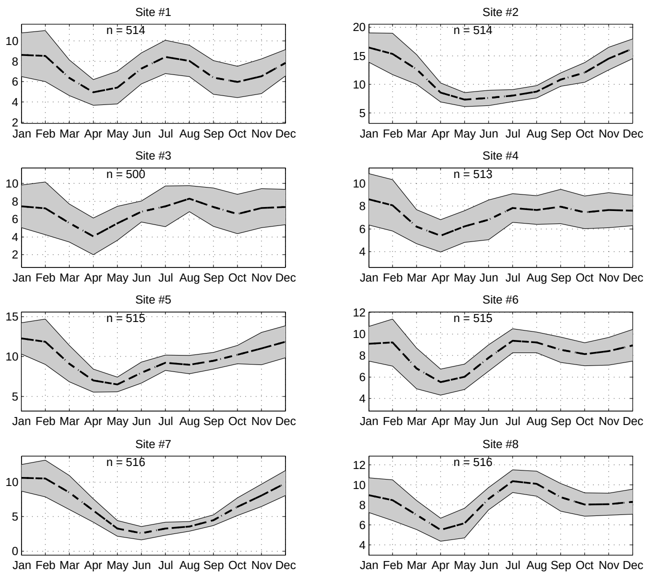

Figure 2.28: The mean d-excess annual cycle [‰] at the 8 sites indicated in Figure 2.27. The shaded area is ± one standard deviation for the monthly values.

The influence of the moisture source areas on the modeled d-excess annual cycle must remain speculative for the moment, as there is no algorithm in connection with REMO$_{iso}$ to directly trace the moisture source areas. However, it can be investigated which relations are causing the shape of the modeled annual cycle. A starting point is the d-excess-δ^{18}O relation shown in Figure 2.23. Basically, when the δ^{18}O is below -20‰ d-excess values are inverse proportional to the δ^{18}O. This will mainly be effective during winter in the interior of the ice sheet where the lowest δ^{18}O values are seen.

By looking at the summer d-excess levels for the different regions it is seen that the values are around 8‰ for both the interior of the ice sheet and towards the coast. So, the difference in annual cycle mainly lies in the elevated September to April d-excess levels for the interior of GIS. One explanation is that only d-excess levels in the interior of the ice sheet is dominated by the inverse relation to the δ^{18}O for the September to April part of the year, as the isotopes for the rest of Greenland are simply not depleted enough for the inverse relation to have effect.

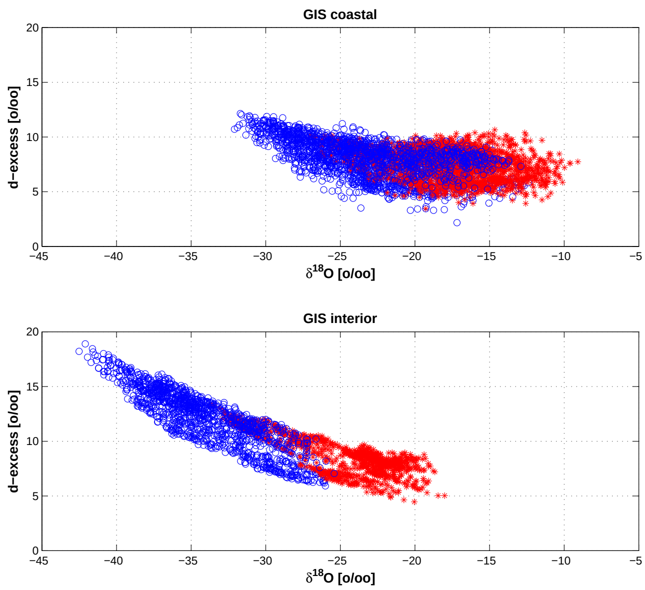

Figure 2.29: Monthly mean d-excess plotted against δ^{18}O for coastal areas (top) and interior areas (bottom) of GIS. The red markers are data for May to October and blue markers are data for November to April. The upper panel is for areas which have a summer/winter d-excess ratio above 0.9, while the lower panel is for the interior of GIS with a summer/winter d-excess ratio less than 0.8. The exact areas can be seen in Figure 2.27.

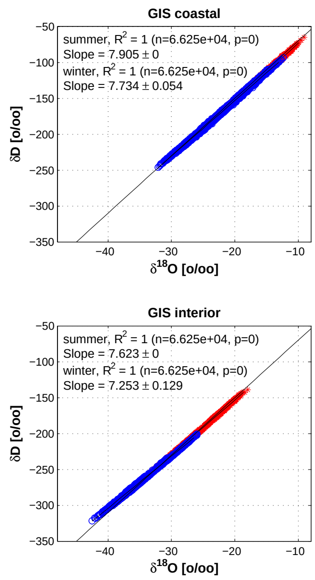

Figure 2.30: Monthly mean δD plotted against δ^{18}O for the same data as in Figure 2.29. Also plotted is the Global Meteoric Water Line $\delta D = 8\delta^{18}O + 10$.

This is clearly seen in Figure 2.29, where the d-excess values for the interior GIS follow a negative slope with respect to the δ^{18}O, while the areas towards the coast have a more flat response. Even for the winter values the increase in d-excess for the coastal areas is quite small when compared to the interior. If any moisture source effects are disregarded, the increasing

d-excess can be explained by the following. The equilibrium fractionation factors for $H_2^{18}O$ ($\alpha_{^{18}O}$) and HDO (α_D) depend differently on temperature, so that α_D increases faster with lower temperatures compare to $\alpha_{^{18}O}$. For low temperatures this causes the δD values in precipitation to be relatively enriched compared to δ^{18}O. This is seen for the δD-δ^{18}O slope for the GIS interior in Figure 2.30, where the data points for very depleted isotopes bend of the GMWL. Further deviation from the slope of 8 automatically causes the d-excess to rise for progressively depleted isotope values. This points out that the differences in the modeled d-excess annual cycle for the coastal and interior do not have to be a moisture source effect.
The question of the influence of the moisture source on the d-excess raises some issues for this REMO$_{iso}$ simulation. Firstly, the main moisture source area for Greenland lies outside the model domain, in which case the main moisture pickup is dealt with in the course resolution of the global model. Secondly, there is the question of how the moisture sources vary regionally for sites across Greenland. The first question raises the issues of how well the course resolution global model, in which REMO$_{iso}$ is nested in, captures the moisture uptake during cyclogenesis, and how well the moisture source information translates from the global to the regional model.
These issues regarding the input from the global model are hard to quantify and beyond the scope of this study. For the second question we can turn to a study made by Sodemann et al. [2008b,a]. Here the authors use a back trajectory method, specifically designed for moisture, coupled with a Rayleigh-type isotope distillation model to determine the moisture source regions [Sodemann et al., 2008b] and isotopes in precipitation [Sodemann et al., 2008a] for Greenland based on the ERA-40 re-analysis. The study was focused on the winter season and the influence on the NAO. Since the ERA-40 re-analysis is the same basis as for the REMO$_{iso}$ and ECHAM$_{iso}$ simulations the overall circulation patterns must be very close, which gives the best basis for dealing with the lack of specific source diagnostics in REMO$_{iso}$ and ECHAM$_{iso}$. Sodemann et al. reported more southern source areas for the interior of GIS compared to coastal areas [Sodemann et al., 2008b], and therefore $\sim 5^oC$ higher source temperatures [Sodemann et al., 2008a]. Although the authors reported that the back trajectory method coupled with the simple isotope model overestimates the observed δ^{18}O values with 13-14‰ , the back trajectory part of the study is still the best 'guess' for source areas for Greenland.
In Figure 2.31 the results of a simple Rayleigh-type model including kinetic effects [Sjolte, 2005] is reviewed in comparison with the REMO$_{iso}$ output. For simplicity the simple model was run using the closure assumption for the initial water vapor, although this is know to under estimate the d-excess with

3 to 4‰ [Armengaud et al., 1998]. By underestimating the d-excess the simple model will overestimate the source temperature, since they are positively correlated. However, the simple mode should still give a good estimate of the relative response in the d-excess for a change in source temperature. For the simple model an increase of 5^oC in moisture source temperature, as found by Sodemann et al. [2008b], can give an increase in d-excess of around 3‰ for δ^{18}O values in the -30 to -40‰ range. This points to that the $\sim$ 10‰ difference in REMO$_{iso}$ d-excess for coastal versus inland areas, as seen for winter δ^{18}O values, is mainly caused by the temperature dependence of the fractionation factors.

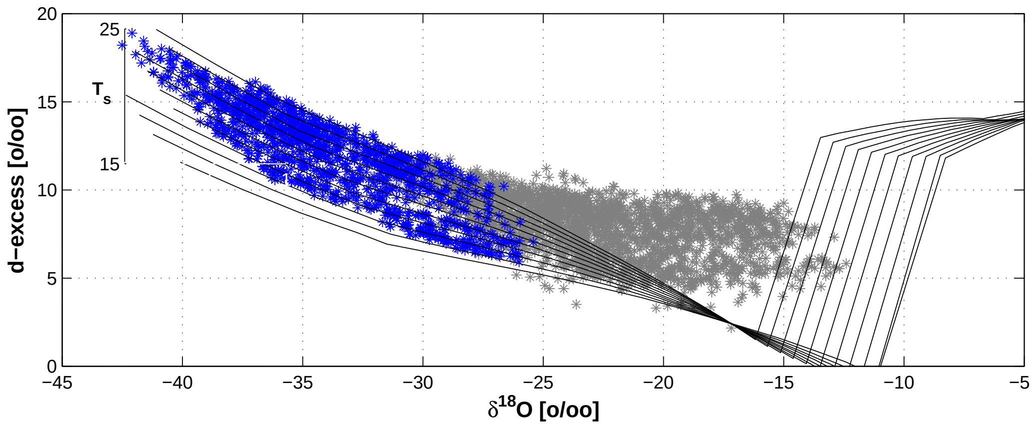

Figure 2.31: Monthly mean δ^{18}O plotted against d-excess for November to April modeled by REMO$_{iso}$. The blue markers are for the interior GIS and gray markers are for coastal areas. Also plotted are results from 11 runs with a Rayleigh-type fractionation model with source temperatures (T$_s$) ranging from 15^oC to 25^oC in steps of 1^oC and relative humidity held constant at 70%.

To capture the same range of d-excess values as REMO$_{iso}$ the Rayleigh-type model was run with different source area conditions. The relative humidity was held constant at a typical value of 70%, while the source temperature was varied from 15 to 25^oC in steps of 1^oC. From Figure 2.31 it is seen that a source temperature of 17^oC to 25^oC is needed to cover the REMO$_{iso}$ d-excess range. Even with the bias of the simple model, which maybe would reduce the source temperature estimate to the range 12 to 20^oC, this is considerably warmer than the findings of Sodemann et al. [2008a], where the mean source temperatures were found to be between 5^oC to 10^oC. Since the ECHAM$_{iso}$ and REMO$_{iso}$ model runs are nudged to the ERA-40 re-analysis and the back

trajectory is calculated using same re-analysis, it is to be expected that the moisture advection, and thus the moisture sources, would be of more similar origin than depicted by the difference in source temperature mentioned above.
Another, and more likely possibility, is that the δ^{18}O - δD relation for low temperatures is not calculated correctly by REMO$_{iso}$. As discussed above, the temperature dependence of the equilibrium fractionation factors $\alpha_{^{18}O}$ and α_D causes the δ^{18}O - δD slope to decrease for very depleted isotopes. However, it is the effective fractionation factors that finally decides the fractionation process. The effective fractionation factors accounts for both $\alpha_{^{18}O}$ and α_D, as well as the effects of diffusive processes during snow formation, which is controlled by the cloud supersaturation. The effect of including the supersaturation is to counteract the effect of the temperature dependence of the fractionation factors, which in turn damp the decrease in δ^{18}O - δD slope [Jouzel and Merlivat, 1984] and increases the d-excess.
If indeed the handling of the supersaturation is incorrect the d-excess signal modeled by REMO$_{iso}$ cannot be seen as an indicator of moisture source temperature for the very depleted δ^{18}O values found in interior of the GIS. This goes for both for the annual mean levels and the annual cycle.
To answer the question regarding the tuning of the REMO$_{iso}$ supersaturation experiments must be made where the supersaturation is varied. Since REMO$_{iso}$ is a very demanding model in terms of computing resources, this has not yet been done. Before initiating future experiments with REMO$_{iso}$ the effects of changing the supersaturation parametrization could be studied with a Rayleigh-type model including kinetic effects. In Appendix A.5 examples of running with different supersaturation parametrizations in a simple model are shown.
Other processes not directly related to the isotope fractionation scheme of the model could be causing the overestimated d-excess values. This could be mechanisms controlling the rain out of precipitation, convection schemes or other related processes. It has for example been shown that in a Rayleigh-type model the d-excess-δ^{18}O relation is affected by the dew point [Johnsen et al., 1989, Sjolte, 2005], which is essentially controlling the onset of the distillation process.

Model and ice core δ^{18}O and d-excess for Site G

As shown in the comparison with the GNIP data the anti-phase behavior with respect to to the δ^{18}O cycle of low altitude coastal sites is well correlated with the modeled annual cycles. However, the 2-3 month lag in annual cycle between δ^{18}O and d-excess as reported by Johnsen et al. [1989] is not found

in the modeled annual cycle for sites further inland. Originally the 3 month lag in d-excess annual cycle was found in ice core data from DYE 3 and Site G by comparing high resolution δ^{18}O and d-excess series. Here the Site G ice core data is reviewed and compared to REMO$_{iso}$ data.
In Figure 2.32 the 11 years of Site G δ^{18}O and d-excess is plotted along with δ^{18}O and d-excess modeled by REMO$_{iso}$. Also plotted is the back-diffused ice core data. The back-diffused data was provided by Bo M. Vinther of the Centre for Ice and Climate in Copenhagen (*unpublished*). The back-diffusion method is a mathematical way of restoring the amplitude of the isotope signal which is lost due to diffusion in the firn [Johnsen, 1977, Johnsen et al., 2000].

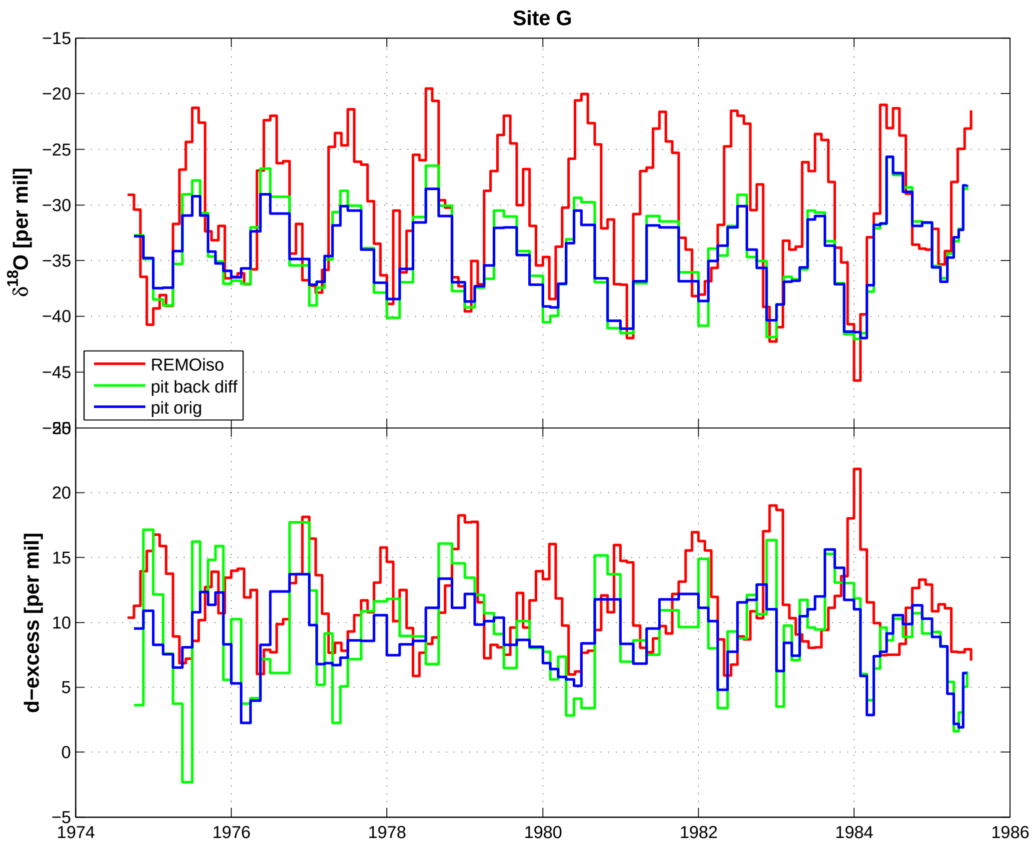

Figure 2.32: Site G original (blue) and back-diffused (green) δ^{18}O and d-excess, along with δ^{18}O and d-excess modeled by REMO$_{iso}$. The dating of the ice core was done by matching up maxima and minima in the ice core δ^{18}O with the modeled δ^{18}O.

The first thing to be noted is that the modeled annual δ^{18}O amplitude is about 50% higher than in the ice core data. This is the case for both

the original and back-diffused data. It could look like the model is simply overestimating the level of summer δ^{18}O values, but most likely this is due the to the overestimated amplitude and a positive bias all year round. The mean annual temperature of Site G is -30^oC while the modeled temperature is -24^oC, which explains the positive bias in δ^{18}O. The model elevation of Site G is only 25m too low, so the temperature bias due to the general warm bias for Greenland discussed in Section 2.1.3.
In terms of variability the model captures the winter δ^{18}O variability very well. There is less variability during summer, but there still seem to be some agreement between the model and the ice core data. This is basically what we also saw in general for temperature and isotopes in Section 2.1.

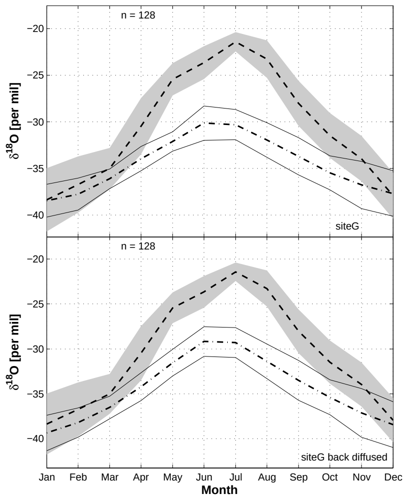

Figure 2.33: Mean annual cycle for Site G: original ice core data (dash-dotted upper panel) and back-diffused ice core data (dash-dotted lower panel) δ^{18}O, along with δ^{18}O modeled by REMO$_{iso}$ (dashed).

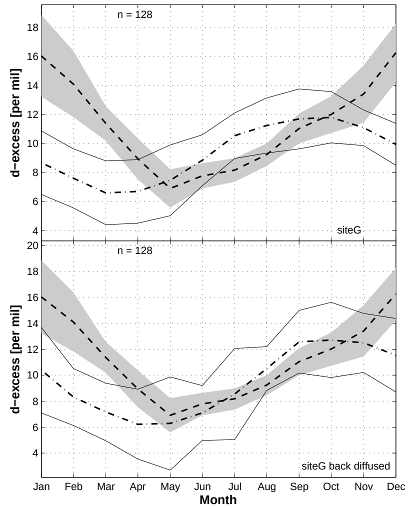

Figure 2.34: Mean annual cycle for Site G: original ice core data (dash-dotted upper panel) and back-diffused ice core data (dash-dotted lower panel) d-excess, along with d-excess modeled by REMO$_{iso}$ (dashed).

For the d-excess there is not the same agreement between model and data, with respect to timing of the annual cycle and variability. The model does seem to fit the back-diffused data better than the original data, both in terms of amplitude and timing of peaks. If we turn to Figure 2.33 and Figure 2.34, where the mean annual cycles are plotted, this becomes more clear. For the original ice core data the 3 month lag between d-excess and δ^{18}O is clearly seen, with the δ^{18}O peaking in June-July and the d-excess peaking

in September-October. In the back-diffused d-excess data the phase of the annual cycle appears to be shifted one month later in the year compared to the original data. The significance of this can be debated as the back-diffused d-excess is quite noisy and based on a relatively short time series. However, the back-diffusion does marginally improve the agreement between the ice core data and the model output.
The largest discrepancy between the model and the ice core data is found in the months November to April, where the model consequently gives too high d-excess values. For these months the δ^{18}O is below -30‰ , which means that the modeled d-excess is dominated by the decrease in δ^{18}O-δD slope discussed in relation with Figure 2.29 and 2.30. In the light of this the main reason for the discrepancy between the ice core d-excess might be the tuning of the super saturation parametrization.

2.3.3 Time series for Ny Ålesund, Reykjavik and Danmarkshavn

As mentioned in Section 2.3.1 recorded isotope data from Greenland weather stations is not abundant, and not many continuous records of more than a few years exist, especially if the both δ^{18}O and δD are needed. δ^{18}O data from Reykjavik were already discussed in Section 2.1. Here time series of δ^{18}O and d-excess from Ny Ålesund, Reykjavik and Danmarkshavn are discussed. The data for these three locations is starting in the early 1990s and is fairly complete until the end of the REMO$_{iso}$ model run in 2001.

Location	R^2 T2m	R^2 precipitation	R^2 δ^{18}O	R^2 d-excess
	sum/win	sum/win	sum/win	sum/win
Reykjavik	0.76/0.84	0.10/0.20	0.05/0.30	0.01/0.50
Ny Ålesund	0.66/0.58	0.22/0.32	0.13/0.87	0.15/0.02
Danmarkshavn	0.08/0.53	0.40/0.13	<0.01/0.12	0.24/0.02

Table 2.3: The square of the linear correlation between observations and REMO$_{iso}$ output for seasonal means for Reykjavik (1992-2001), Ny Ålesund (1990-2001) and Danmarkshavn (1991-2001). Summer is defined as May to October and winter is defined as November to April.

In Table 2.3 R^2 between observed and modeled data for seasonal t2m, precipitation, δ^{18}O and d-excess is listed. Since the time series only span about 10 years the statistics are only significant ($p<0.05$) when R^2 is above 0.4. The best fit for δ^{18}O is found for Ny Ålesund winter data with a very good agreement of R^2=0.87, while the best fit for d-excess is for Reykjavik winter data. There is not a good match for the Ny Ålesund d-excess in spite of the well reproduced δ^{18}O. This could be due low quality d-excess data, as the R^2 between the measured Ny Ålesund δ^{18}O and δD only is 0.93, while the R^2 for Reykjavik and Danmarkshavn is 0.98 for both sites.

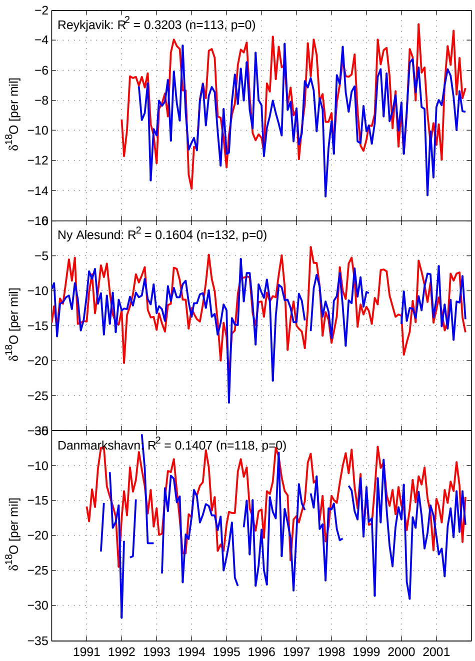

Figure 2.35: Modeled (red) and observed (blue) monthly mean δ^{18}O for Reykjavik, Ny Ålesund and Danmarkshavn.

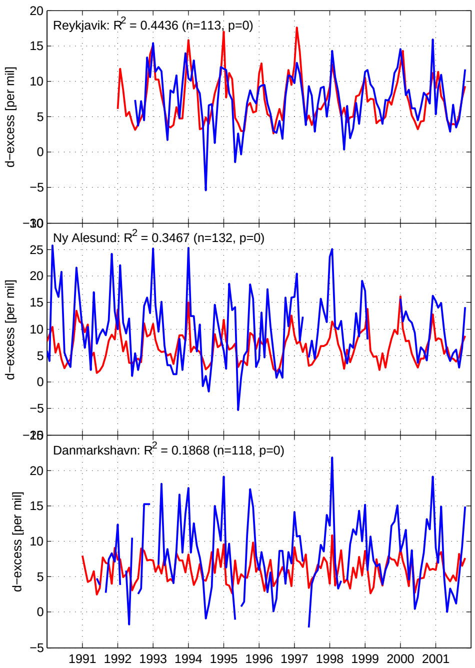

Figure 2.36: Modeled (red) and observed (blue) monthly mean d-excess for Reykjavik, Ny Ålesund and Danmarkshavn.

For Reykjavik the winter d-excess R^2 of 0.5 is notable higher than the δ^{18}O R^2 of 0.3. This is surprising since the d-excess is a second order parameter. There can be multiple causes for this. Firstly, if the model has a bias in both the δ^{18}O and the δD, the difference between the two could cancel out these biases. Secondly, as the d-excess is thought to be strongly related to the evaporative conditions at the vapor source, it could be that the model is better at producing this rather than processes like rain and snow that involves cloud processes. Thirdly, in the GNIP data the d-excess is calculated from two measured data series which have some level of noise. By subtracting the two series you are effectively stacking the data and thus canceling out some of the noise, which could result in a better correspondence between model and data.
To turn to the monthly data the time series for δ^{18}O and d-excess time series

for Reykjavik, Ny Ålesund and Danmarkshavn are shown in Figure 2.35 and 2.36. In all three cases the R^2 is higher for the d-excess, which is most probably because the measured d-excess shows a clearer annual cycle than the δ^{18}O. The measured δ^{18}O looks quite noisy during summer compared to the modeled data.
As for the mean annual cycle and seasonal means the model achieves the best fit to the measured d-excess for Reykjavik. The match is quite convincing and encourages the further use of REMO$_{iso}$ to study the d-excess.

2.3.4 Summary

Using the ERA-40 based experiment REMO$_{iso}$ was evaluated in terms of the d-excess for Greenland and the North Atlantic area. For central Greenland REMO$_{iso}$ was found to overestimate the mean annual d-excess, while the match was better for coastal regions. Next the model was compared to the mean annual cycle of δ^{18}O and d-excess for coastal GNIP/IAEA data in from Greenland, Iceland and Svalbard. The model was found to match the δ^{18}O fairly well, although the amplitude of the modeled annual cycle had a tendency to be overestimated. For the d-excess the modeled annual cycle was found to exhibit the same anti-phase behavior with the δ^{18}O as in the observations. Especially the match between the Reykjavik data and the model was found to be very good.
The REMO$_{iso}$ output was also compared to back-diffused isotope data from Site G. The model was found to replicate the winter variability of δ^{18}O very well. For the mean d-excess annual cycle the match between the model and ice core data was marginally better for the back-diffused data than the original ice core data, although the model overestimates the winter d-excess.
The overestimated winter d-excess for Site G, as well as the overestimated d-excess for central Greenland, was found to be caused by a model bias for the δ^{18}O-δD slope for δ^{18}O values below $\sim$ -30‰. By comparison with a simple Rayleigh-type model and a back trajectory study by Sodemann et al. [2008b,a] it was argued that it is likely that the parametrization of the supersaturation chosen for the REMO$_{iso}$ experiment is causing the overestimated d-excess. However, other sources causing the model bias could not be excluded.
As a last part of the d-excess study the model was compared with the most recent time series overlapping with the modeled time period. This included data from Ny Ålesund, Reykjavik and Danmarkshavn. REMO$_{iso}$ proved to preform very well for Reykjavik, with a R^2 of 0.50 for the mean winter d-excess, while no convincing correlation was found with Ny Ålesund and Danmarkshavn. The mismatch between model and observations for Ny Åle-

sund could be related to measurement noise in the data.
It has been shown in this section that, while there is room for improvement, the REMO$_{iso}$ study did give some very promising results, and with some refinements REMO$_{iso}$ could aid with the interpretation of the d-excess in future studies.

2.4 Discussion of the REMO$_{iso}$ experiment.

This REMO$_{iso}$ experiment has shown that the model captures the importance of the NAO for the Greenland climate variability very well. Also the main features of spatial patterns and annual cycles of temperature, precipitation and δ^{18}O are well reproduced. However, there are a number of biases of which the most pronounced are listed below.

- For inland Greenland there is a bias for temperature, which is about $+5^{o}C$ in mean annual. The bias is stronger towards the north, and for both southern and northern regions strongest during summer.
- In the northern central Greenland the accumulation is underestimated by about 25%.
- Compared to ice core data there is a bias in annual mean δ^{18}O of +4.4‰. Seasonally this bias is as the temperature bias strongest during summer.
- Finally, there is a bias in the d-excess, which spatially shows as overestimation of the d-excess when then δ^{18}O values are below ~-30‰. The d-excess bias also shows in the annual cycle for the Site G ice core, where the winter d-excess is overestimated.

While the causes for the temperature bias was discussed in Section 2.1.3, the accumulation bias will be discussed further here. Too dry conditions in cold regions is not something unique to REMO$_{iso}$ as a climate model. In a study by Masson-Delmotte et al. [2008] a dry bias in three GCMs (ECHAM4, MUGCM, GISS-E) was found for inland Antarctica. This was attributed to an underestimation of the vapor transport to the cold regions. Kiilsholm et al. [2003] showed similar accumulation rates as REMO$_{iso}$ for inland Greenland, using the HIRHAM regional model in a 50km resolution, while Box et al. [2006] did not report a dry bias for the Polar MM5 regional model in a 24km resolution. This could suggest that even higher resolution than the ~55km used in this REMO$_{iso}$ simulation is needed to reach proper accumulation rates in cold regions.
The seasonality of the δ^{18}O and temperature bias suggests that at least part of the δ^{18}O can be explained by too high temperatures. However, the northward depletion of ^{18}O and the temperature-δ^{18}O slope was in fact also underestimated, which means that the δ^{18}O bias is not only caused by temperature. In the study by Masson-Delmotte et al. [2008] mentioned above, the GCMs were also fitted with isotope diagnostics. The authors report a positive bias in δD, which they attribute to the cold regions dry bias also mentioned above.

A dry bias for cold regions means that there will be even less snow during cold periods, creating a precipitation weighting towards more positive mean δ^{18}O values. With the REMO$_{iso}$ dry bias in mind, this and the temperature bias could explain the overestimated δ^{18}O values for inland Greenland. However, a study on short time scales resolving individual precipitation events is necessary to quantify this.

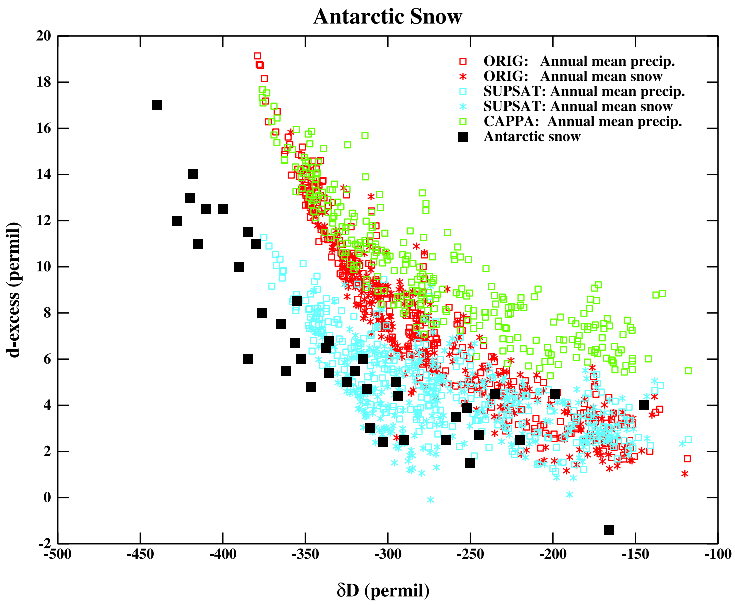

Figure 2.37: Figure adapted from Schmidt et al. [2005] showing the d-excess for Antarctic snow plotted against δD. The data to note is the output for the control run (ORIG) (red), the SUPSAT run (cyan), and the observations (black). The ORIG data was produced using a supersaturation of S$_i$=1-0.003*T[^{o}C], while the SUPSAT data was produced using S$_i$=1-0.004*T[^{o}C]. It is clear that the SUPSAT run matches the observations better.

In Section 2.3.2 it was argued that the main cause of the overestimated d-excess was the parametrization of the supersaturation. Again from the study by Masson-Delmotte et al. [2008] already mentioned twice, the ECHAM4 and the MUGCM showed an overestimated d-excess for low δD in Antarctica very similarly to the output of REMO$_{iso}$ for Greenland. However, for the GISS-E model Schmidt et al. [2005] showed that for a parametrization of the supersaturation with higher supersaturation for low temperatures a very good agreement with observations is found (see Figure 2.37).
The same standard supersaturation of S$_i$=1-0.003*T[^{o}C] [Hoffmann et al., 1998] was used for the REMO$_{iso}$ experiment and the GISS-E control run

(ORIG) shown in Figure 2.37. As the isotopic scheme of REMO$_{iso}$ and GISS-E basically are the same a more realistic d-excess versus δ^{18}O relation would probably also be obtained by changing the supersaturation to S$_i$=1-0.004*T[^{o}C] in REMO$_{iso}$.
With respect to the overestimated modeled winter d-excess for Site G, it is likely that the new tuning also here would diminish the discrepancy with the ice core data. From Figure 2.38 it can be seen that the spatial relation between d-excess and δ^{18}O also holds temporally as the monthly model output for Site G follows the same trend as the spatial distribution of mean annual data. This means that the d-excess versus δ^{18}O relation is general for REMO$_{iso}$ both temporally and spatially. It is not obvious that this relation should hold generally as the d-excess through the supersaturation parametrization strongly depends on the cloud condensation temperature.

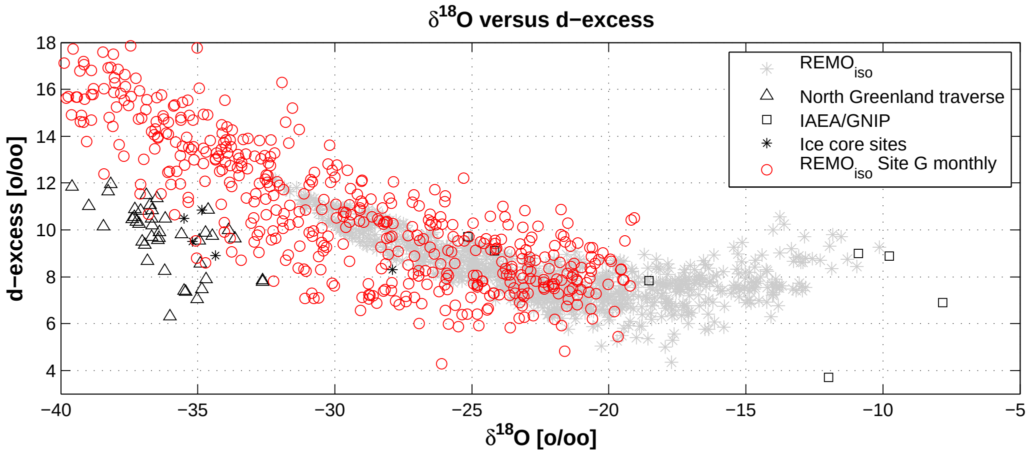

Figure 2.38: Modeled annual mean weighted δ^{18}O plotted against d-excess, as well as the modeled monthly data for Site G. Also plotted is observations from IAEA/GNIP, major ice core sites, and the North Greenland Traverse.

Fujita and Abe [2006] presented the isotopic composition of one year of daily snow samples from Dome Fuji, Antarctica. They showed that also here the d-excess versus δ^{18}O relation is valid both temporally and spatially, as the daily data followed the same curve as the spatial data from Petit et al. [1991]. While the same has not been tested for Greenland the findings by Fujita and Abe [2006] do suggest that the general nature of the d-excess-δ^{18}O relation shown for REMO$_{iso}$ is realistic.

Chapter 3

Modeling stable isotopes in precipitation during the Eemian

3.1 The Eemian interglaciation

Before we go on to the model results this section gives an introduction to the Eemian climate, and why this period is of interest in our particular time frame.

3.1.1 Geologic evidence of the Eemian interglaciation

In marine and ice cores the Eemian is defined as Marine Isotope Stage 5e (MIS 5e). In terms of δD values from the Dome C ice core it is characterized by having the highest values during the last 800kyr. At Dome C the Eemian levels are about 30‰ less depleted in δD compared to the present level, while the values for the NGRIP core are 3‰ less depleted in δ^{18}O (see Figure 3.2). At both sites this is estimated to translate into a warm anomaly for the Eemian of about $+5^{o}C$ [Jouzel et al., 2007, Andersen et al., 2004].
The CAPE Last Interglacial Project has collected material from a number of studies on the Eemian in an effort to quantitatively map the Eemian warming based on various geologic evidences [Anderson et al., 2006]. The data used counts isotopic proxies from marine cores, ice cores and lake sediments as well as biotic proxies from lakes, peat and river beds. From this data the conclusion is that at the height of the Eemian warm period summer temperatures in the higher latitudes of the Northern Hemisphere were about $5^{o}C$ higher than present (see Figure 3.1).
Moreover the global sea level is believed to have been 3-5 meters higher than present [Stirling et al., 1998, Israelson and Wohlfarth, 1999]. In the CAPE

study [Anderson et al., 2006] the global sea level, or minimum of terrestrial ice, is used for defining the duration of the Eemian. The sea level was higher than present in the period from 130kyr BP to 116kyr BP, thus defining the duration of the Eemian. There is some evidence that the sea level did not reach its peak until after 121 kyr BP where a sudden jump in sea level might have occurred [Blanchon et al., 2009].

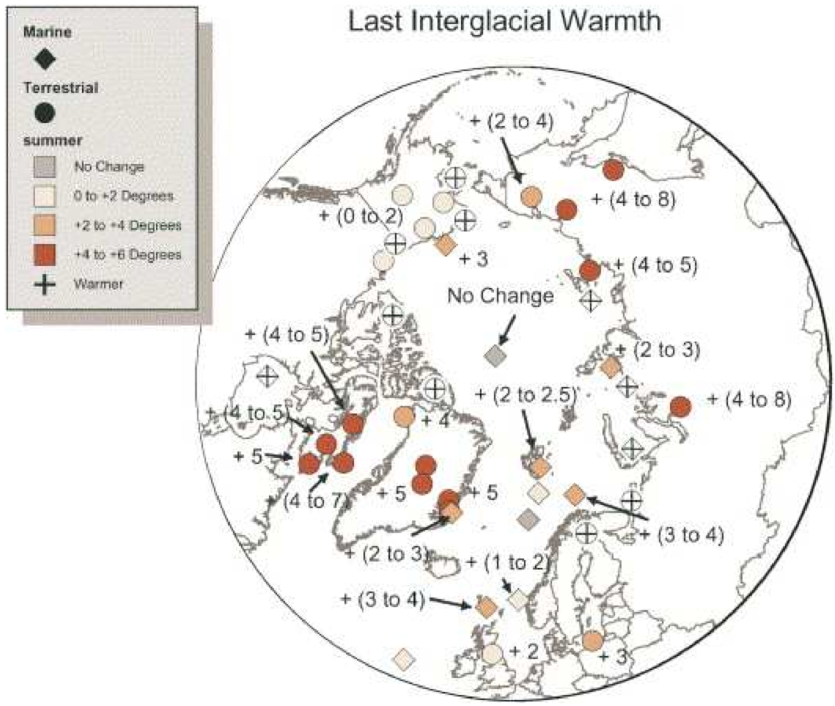

Figure 3.1: Maximum Eemian summer temperature anomalies relative to today derived from palaeotemperature proxies. The figure is adapted from Anderson et al. [2006].

A sea level 3-5m higher than present can only be explained by a reduction of the ice sheets in Greenland and Antarctica. It is disputed where the largest contribution to the sea level rise came from. Otto-Bliesner et al. [2006] suggest that the southern dome of the Greenland ice sheet was melted away during the Eemian contributing 2.2 to 3.4m to the sea level rise, while Cuffey and Marshall [2000] suggested an even more dramatic reduction of GIS contributing 4 to 5.5m. However, the elevated δ^{18}O values found in the silty ice at the bottom of the DYE3 ice core, drilled on the southern dome summit, suggest Eemian ice is present in the core [Johnsen et al., 2001].

Furthermore DNA studies point towards that the DYE3 site has not been ice free for the last 450kyr [Willerslev et al., 2007].
In Antarctica the western part of the ice sheet is believed to be very sensitive to changes in sea ice [Rignot and Jacobs, 2002]. Warmer waters around Antarctica could have led to instability of the West Antarctic Ice Sheet, and a collapse of WAIS could explain a sea level rise of the order of magnitude as that of the Eemian [Oppenheimer, 1998].

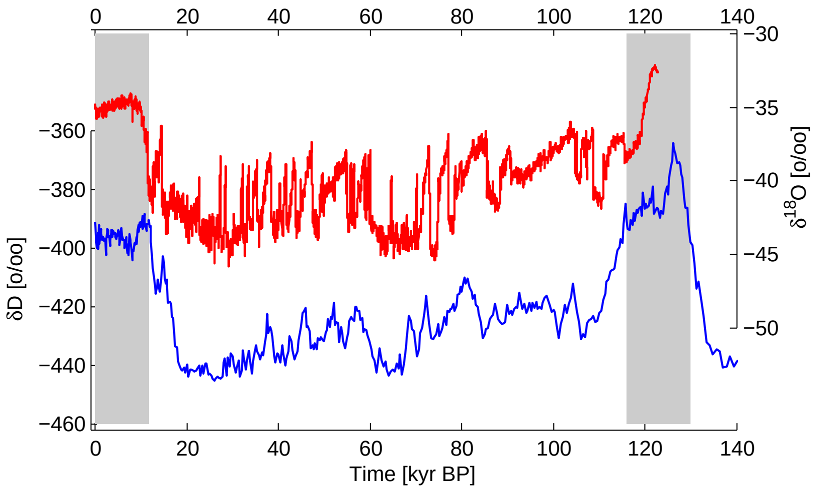

Figure 3.2: δ^{18}O from the NGRIP (red) ice core [Andersen et al., 2004] and δD from the Dome C (blue) ice core [Augustin et al., 2004], covering the period from the present back to the previous interglacial, the Eemian. The grey shadings mark the duration of the Holocene from present back to 11.700 BP and the Eemian from 116kyr BP to 130kyr BP.

The exact timing of the climatic optimum of the Eemian is not well defined, and did not take place synchronously across different geographical regions [Zagwijn, 1996]. This spatial asynchrony in the optimum, as well as dating uncertainties [Anderson et al., 2006] in the proxy data, makes the assessment of the climate development during the Eemian difficult.

3.1.2 Causes for the Eemian interglaciation

The Eemian interglacial is one of several warm periods occurring about every 100kyr for the past 1myr. The general view is that this is caused by the changes in insolation accounted for by the Milankovich theory [Berger, 1988]. The mechanism behind deglaciation is that increased summer insolation is amplified by a number of feedback mechanisms such as the degassing of CO_2 from the ocean due to increasing ocean temperatures [Monnin et al., 2001], the ice-albedo feedback [Hall, 2004] and the water vapor feedback [Langen and Alexeev, 2007, Dessler et al., 2008]. Also a vegetation feedback is believed to have been important in connection with the Eemian as there is evidence for the spreading of boreal forest in for example northern Siberia. This caused an decrease in albedo for the northern latitudes [Anderson et al., 2006].
In Figure 3.3 the orbital parameters and the annual mean insolation for 65^oN is shown for Holocene and the Eemian. The annual mean insolation follows the obliquity, while the seasonal cycle is greatly affected by the precession.

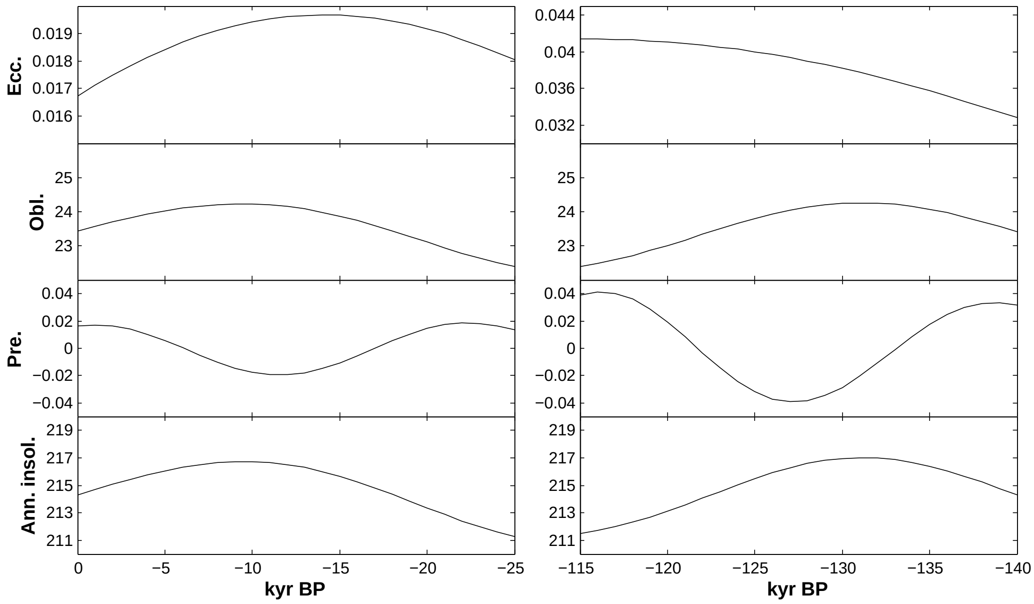

Figure 3.3: Holocene (left) and Eemian (right) eccentricity (Ecc.), obliquity (Obl.), precession (Pre.) and mean annual insolation at 65^oN (Ann. insol.). The calculations were done using the method by Berger [1978].

During the Eemian the Northern Hemisphere summers where shorter and warmer compared to the Holocene. Because of the precession of the vernal equinox the Northern Hemisphere was facing the sun when passing perihelion, as opposed to present where the Northern Hemisphere is facing the sun when passing aphelion. This, modulated by the eccentricity and the obliquity, resulted in the extraordinary strong summer anomaly that caused the onset of the Eemian (see also Figure 3.4).

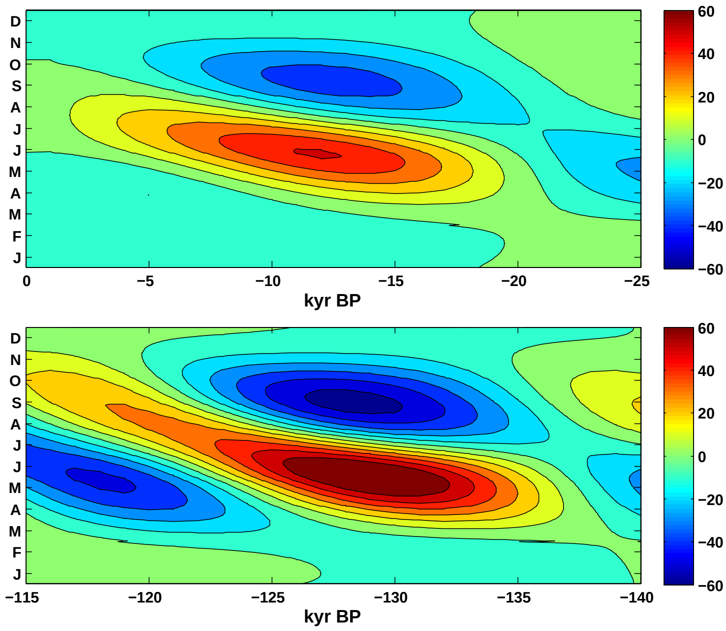

Figure 3.4: Monthly insolation anomaly during the Holocene (upper) and Eemian (lower) at $65^o N$ in Wm^{-2}. The calculations were done using the method by Berger [1978]. The Eemian shows a stronger seasonal amplitude and very strong summer anomalies compared to the anomalies during the Holocene climatic optimum.

3.2 Experiment setup

The SST fields for the preindustrial control run and the three Eemian time slices are from the IPSL_CM4 coupled atmosphere-ocean model [Braconnot et al., 2008]. The IPSL model was run between 300 to 700 years to approach a steady state ocean circulation, and the SSTs used for the ECHAM$_{iso}$ experiments are climatological monthly means calculated from the last 100 years of the simulations. Using these SSTs the ECHAM$_{iso}$ model was run for 12 years for each experiment. The first two years are regarded as spin up period, that is, only the last 10 years of the experiments are used for further analysis.

The SST fields were interpolated from the IPSL regular grid to the ECHAM$_{iso}$ T42 grid. Since the land-sea mask from the IPSL model and the ECHAM$_{iso}$ model does not completely overlap, the IPSL SST data was interpolated to cover land areas as well as to ensure coverage in coastal regions where the land-sea mask might not agree.
Sea ice is treated non-fractional by the ECHAM$_{iso}$ model, that is, all ocean grid points with SSTs below -1.8^oC are sea ice. While the IPSL model does have a realistic annual cycle and coverage of sea ice a few points should be noted [Marti et al., 2005]. In the Northern Hemisphere the sea ice concentration is less than observed all though the coverage is realistic. The sea ice concentration is especially underestimated during summer. For the Southern Hemisphere there is a bias, which means that sea is almost disappears during summer, and also here there is a general underestimation of sea ice concentration. Since sea ice is treated non-fractional by the ECHAM$_{iso}$ model the above mentioned biases will be even more exaggerated in the ECHAM$_{iso}$ interpretation of the sea ice stemming from the IPSL SSTs. This will be discussed further in Section 3.2.1.

3.2.1 Evaluation of control runs

Two control runs has been made for the Eemian experiment, one preindustrial run and one using present day SSTs. The present day control run is forced by climatological AMIP II SSTs [Kanamitsu et al., 2002], present day insolation and uses an atmospheric CO_2 content of 356ppm. The preindustrial control run (IPSL$_{ctrl}$) is based on the IPSL preindustrial experiment SSTs, present day insolation and uses an atmospheric CO_2 content of 280ppm.
The focus of this section is mainly on the differences between the two runs in performance for the polar regions. There are three things that dominate the anomalies for the IPSL$_{ctrl}$ experiment. Compared to the AMIP II run the IPSL$_{ctrl}$ run, the lower CO_2 level, biases in the IPSL_CM4 model, and the non-fractional sea ice of the ECHAM$_{iso}$ model will cause differences in climate. With the lower CO_2 levels for the IPSL$_{ctrl}$ a general colder climate is to be expected, and the IPSL$_{ctrl}$ run does in fact have a global mean surface temperature 0.7^oC lower than the AMIP II run.
The SST biases of the IPSL_CM4 model have been shown to be minor, in general reproducing the climatological mean within 2^oC, except for the 45-50^{o}N region of the North Atlantic, where the model has a major cold bias [Swingedouw et al., 2007]. This bias can also be seen in Figure 3.5.
As discussed above is there some biases in the the IPSL_CM4 models representation of sea ice, this together with the non-fractional sea ice of ECHAM$_{iso}$ causes IPSL$_{ctrl}$ run to have about a factor 2 less sea ice area than the AMIP

II run. It is likely that it is the sea ice deficit that causes the wide spread warm anomaly of up to 5^oC over the Canadian Arctic during DJF, along with warmer temperatures near the coasts around the Arctic ocean, as well as east and west of Greenland.

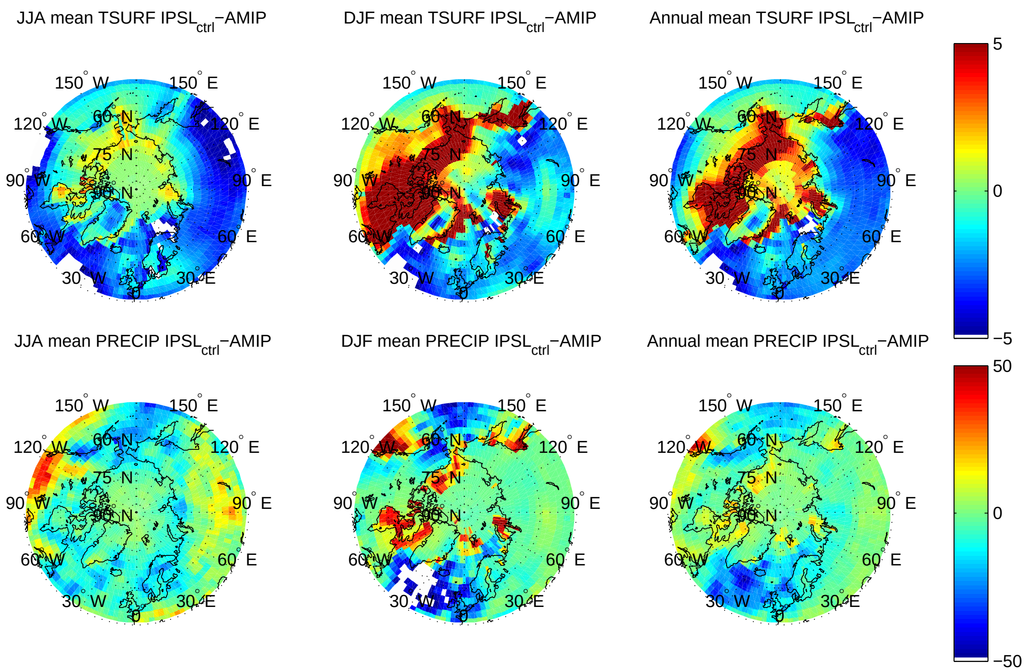

Figure 3.5: Comparison of Northern Hemisphere temperature $[^oC]$ (upper panels) and precipitation [mm/month] (lower panel) for the control run forced by AMIP II SSTs and the preindustrial control run using IPSL SSTs. The data plotted is the IPSL$_{ctrl}$ data subtracted by data from the AMIP II run.

One example of misrepresentation of sea ice is the warm anomaly along the Greenland east coast most prominent during DJF. The East Greenland Current (EGC) is presently transporting Arctic water to the south along with massive amounts of ice [Foldvik et al., 1988, Rudels et al., 1999]. The presence of the EGC cools the climate in the eastern part of Greenland. Since features such as these are missing in the IPSL$_{ctrl}$ one should be careful when analysing regional differences in the Eemian model experiments.
The precipitation anomalies can both be related to the regional temperature patterns and the general change in storm tracks. In the Canadian Arctic there is an increase in precipitation that can be related to the positive temperature anomaly in the same area. The increase in precipitation and the temperature have the same seasonality, and from a thermodynamic view point it is

expected to see an increase of precipitation with an increase in temperature. In the areas well known for high precipitation such as the Greenland south-eastern coast and the west coast of North America, there is an increase in precipitation, which can be explained by a general increased storminess in the colder preindustrial climate.

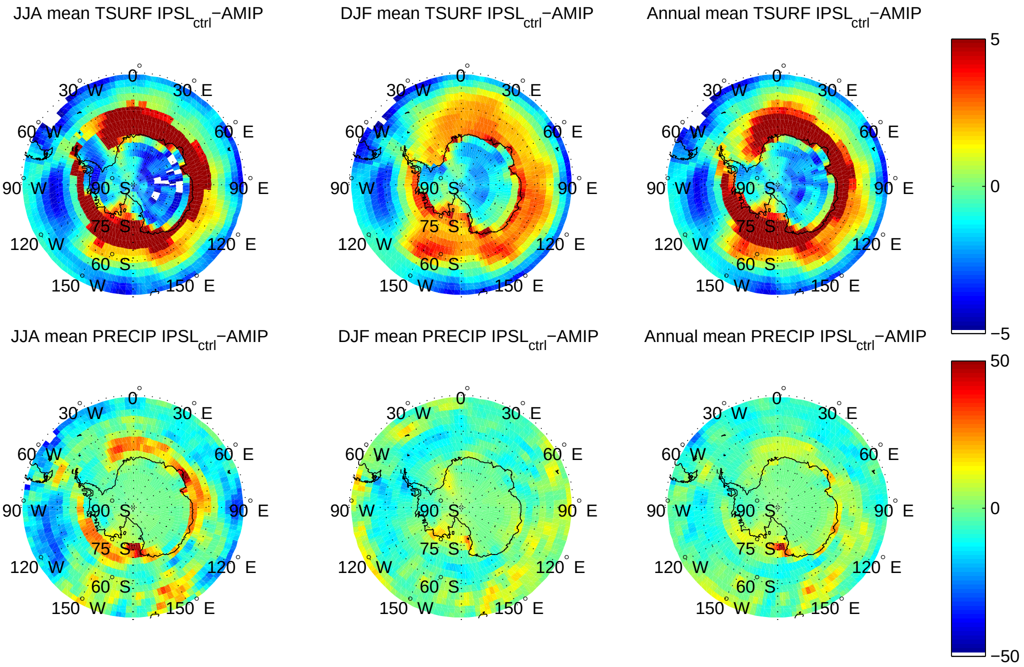

Figure 3.6: Comparison of Southern Hemisphere temperature $[^oC]$ (upper panels) and precipitation [mm/month] (lower panel) for the control run forced by AMIP II SSTs and the preindustrial control run using IPSL SSTs. The data plotted is the IPSL$_{ctrl}$ data subtracted by data from the AMIP II run.

For the southern hemisphere there are similar differences between the AMIP II and IPSL$_{ctrl}$ run as for the northern hemisphere. Again, large local differences in temperature are due to the sea ice representation in the IPSL$_{ctrl}$ run. The anomalies are seen as an circum arctic warm anomaly, of locally more than 5^oC. As for the northern hemisphere the anomaly is most pronounced during winter.

3.2.2 The Eemian experiments

Three Eemian time slice experiments were done along with the two control runs already described. The three Eemian time slices are 115kyr, 122kyr and 126kyr. The first time slice at 115kyr is during the inception of the previous glacial, the second time slice is at 122kyr during the last half of the Eemian and the last time slice is at 126kyr, which is close to the climatic optimum of the Eemian for the Dome C data show in Figure 3.2.
Originally the three Eemian time slices were chosen in order to represent different seasonal timing compared to the insolation for Holocene and present [Braconnot et al., 2008]. For example are the equinoxes rotated by 180^o for 9.5kyr and for 126kyr, which contributes to the very large summer insolation anomalies during the Eemian compare to Holocene (see also Section 3.1.2). For the 122kyr time slice the equinoxes are rotated by 90^o compared to present, and the Holocene analogy for this time slice is the period around 6kyr. Finally does the 115kyr time slice have comparable orbital parameters to to present, with the main difference being the eccentricity.
The model runs are setup as simple as possible, and could be regarded as preliminary investigations into modeling of the Eemian stable water isotopes. The only changes made compared to the preindustrial control experiment, $IPSL_{ctrl}$, are the SST fields and the insolation. The $ECHAM_{iso}$ model, as well as the IPSL model, was run using preindustrial greenhouse gas levels, that is CO_2 levels at 280ppm for all Eemian runs, which is close to the CO_2 levels for the Eemian according to ice core measurements [Fischer et al., 1999]. In these experiments the glacier mask, background albedo and sea level was kept as for present day. No attempts were made to imitate the increased runoff from glaciers and ice sheets during the warm periods.

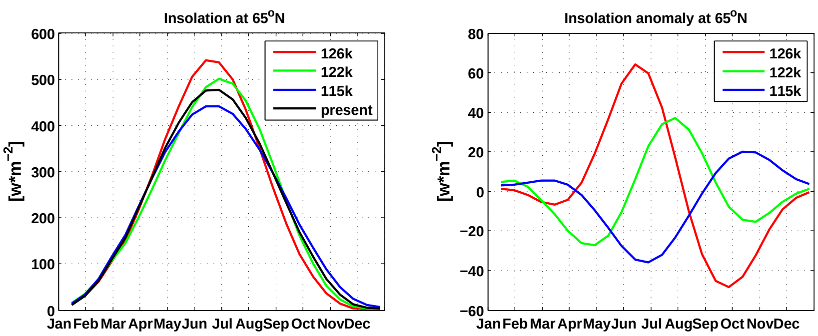

Figure 3.7: Monthly insolation (left) and insolation anomaly (right) for the three Eemian time slices at 65^oN. Calculated using method by Berger [1978].

As discussed in Section 3.1.2 the insolation for the Northern Hemisphere was notably higher in summer during the Eemian. This is again shown in Figure 3.7, where the insolation for each Eemian time slice is plotted for $65^o N$. It should be noted that the phasing of the insolation summer peaks do not coincide. In the simulations a present 360 day calendar was used and the vernal equinox was fixed at the 21st of March. This was also done in the original IPSL experiments. Due to the changes in the orbital parameters the length of the present day seasons no longer apply to the seasons during the Eemian. Alternatively one could apply a calender with angular definitions of the length of the months as suggested by Joussaume and Braconnot [1997]. However, as the simulations are depending on the SSTs from the IPSL runs the same calendar was chosen. The differences caused by the definition of the calendar are minor, but should be kept in mind when comparing annual cycles, seasonal means or individual months.
Since the 21st of March is fixed the greatest error is made during autumn. For the 115kyr and the 126kyr run the differences in phase are minor, but for the 122kyr run the summer peak in insolation is shifted about 15 days towards the end of the year. The different phase of the 122kyr insolation can also be seen in the anomaly as a pronounced double dip.

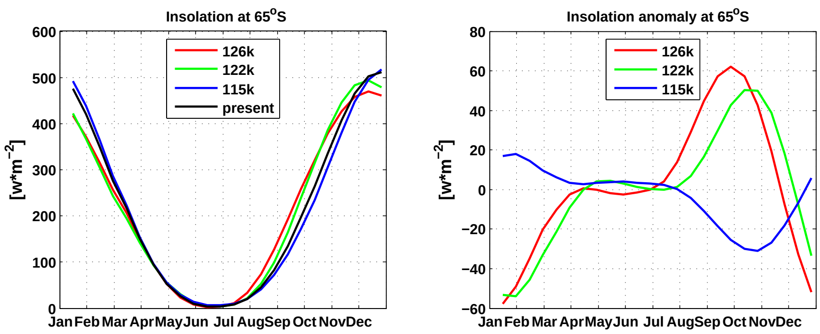

Figure 3.8: Monthly insolation (left) and insolation anomaly (right) for the three Eemian time slices at $65^o S$. Calculated using method by Berger [1978].

The peak insolation anomalies for the Southern Hemisphere are not as large as for the Northern Hemisphere, and the positive anomalies seen for August to December are mainly because of seasonal phase differences (see Figure 3.8). Because the large positive insolation anomaly for the Northern Hemisphere summer is a result of a redistribution of insolation, there will be the opposite effect in the Southern Hemisphere. For example the differences in the maximum of the insolation summer peak for present day and 126kyr is only about -30Wm^{-2}, while it is more than 60Wm^{-2} for the Northern Hemisphere.

3.3 Eemian temperature, precipitation, δ^{18}O and d-excess

This section will give an overview of the seasonal and annual mean changes between the preindustrial climate and the three Eemian time slices for the northern and southern hemisphere. The maps in this section show anomaly data calculated using the IPSL$_{ctrl}$ run as reference.
The analysis of the model output will be restricted to the surface parameters temperature, precipitation and the isotopic composition of precipitation in relation to Eemian proxy data.

3.3.1 Northern Hemisphere anomalies.

In Figure 3.9 the Northern Hemisphere surface temperature anomalies are shown for the Eemian time slices. In some areas very large anomalies exist from one grid box to the next. This is because of the differences in configuration of sea ice, which influence the local heat budget greatly. Both during summer and winter the sea ice will have a cooling effect on the surface air. During the summer the high albedo affects the radiation budget negatively, and during winter the sea ice insulates the air from the warmer ocean temperatures.
The JJA anomalies for the IPSL$_{115k}$ run show temperatures of 1 to 3^oC lower than present. This is in agreement with lower summer insolation during the inception of the glacial period. The greatest anomalies are over the continental areas and there are no significant changes in the temperatures over the Arctic Ocean during summer. The warm anomalies during DJF are partly related to the phase difference of the seasons between the IPSL$_{ctrl}$ and the IPSL$_{115k}$ run, but also due to a difference in the sea ice configuration. This can also be seen in the annual mean temperature anomaly.
For the next time slice, the IPSL$_{122k}$ run, the JJA anomalies show a 1-2^oC warming over continental areas, and up to 1^oC in the Northern Atlantic, the Norwegian sea and off the Greenland east coast. Since the summer peak in insolation for the IPSL$_{122k}$ run is about 15 day later compared to the IPSL$_{115k}$ run, the actual difference in peak summer warmth is probably even higher than depicted in Figure 3.9. The warm anomalies during DJF, especially for the Arctic Ocean, are probably also related to the phase shift of the seasons,

but also that that there is a significant decrease in sea ice cover during winter. This is also evident in the annual temperature anomaly.

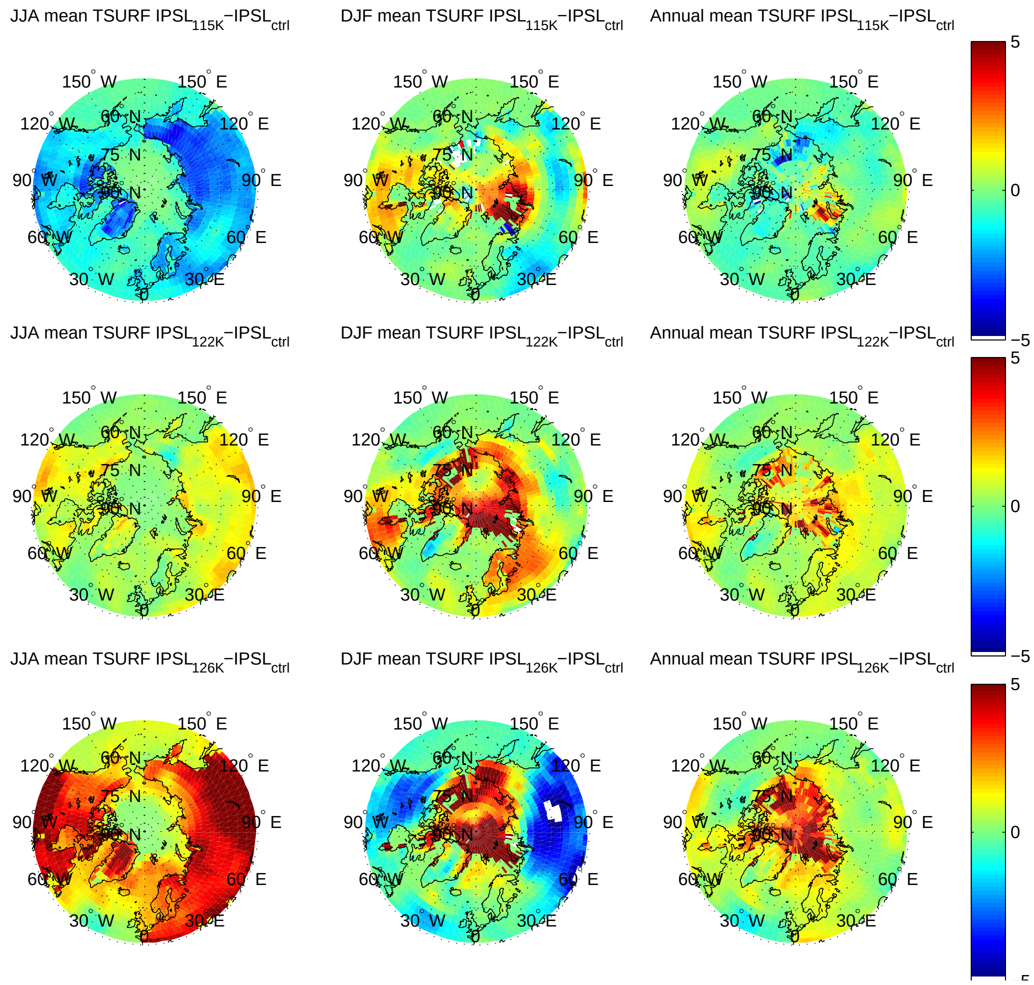

Figure 3.9: ECHAM$_{iso}$ mean surface temperature anomaly [^oC] for June, July and August (JJA), December, January and February (DJF) and annual mean anomaly for the Northern Hemisphere for time slices 115kyr (top), 122kyr (middle) and 126kyr (bottom).

Ice core data from Dome C and Vostok shows that the peak Eemian warmth was between 125kyr and 130kyr for East Antarctica [Augustin et al., 2004, Petit et al., 1999]. With the timing issues for the climatic optimum mentioned in Section 3.1.1 it is not certain that the peak warmth for other regions was in this period as well. However, for this evaluation of the model experiments, it will be assumed that the IPSL$_{126k}$ run represents the period around the Eemian climatic optimum, as this time slice coincides with the Eemian optimum found in the ice cores mentioned above. This also means that the maximum summer temperatures from proxy records shown in Figure 3.1 should be reproduced in the IPSL$_{126k}$ run.

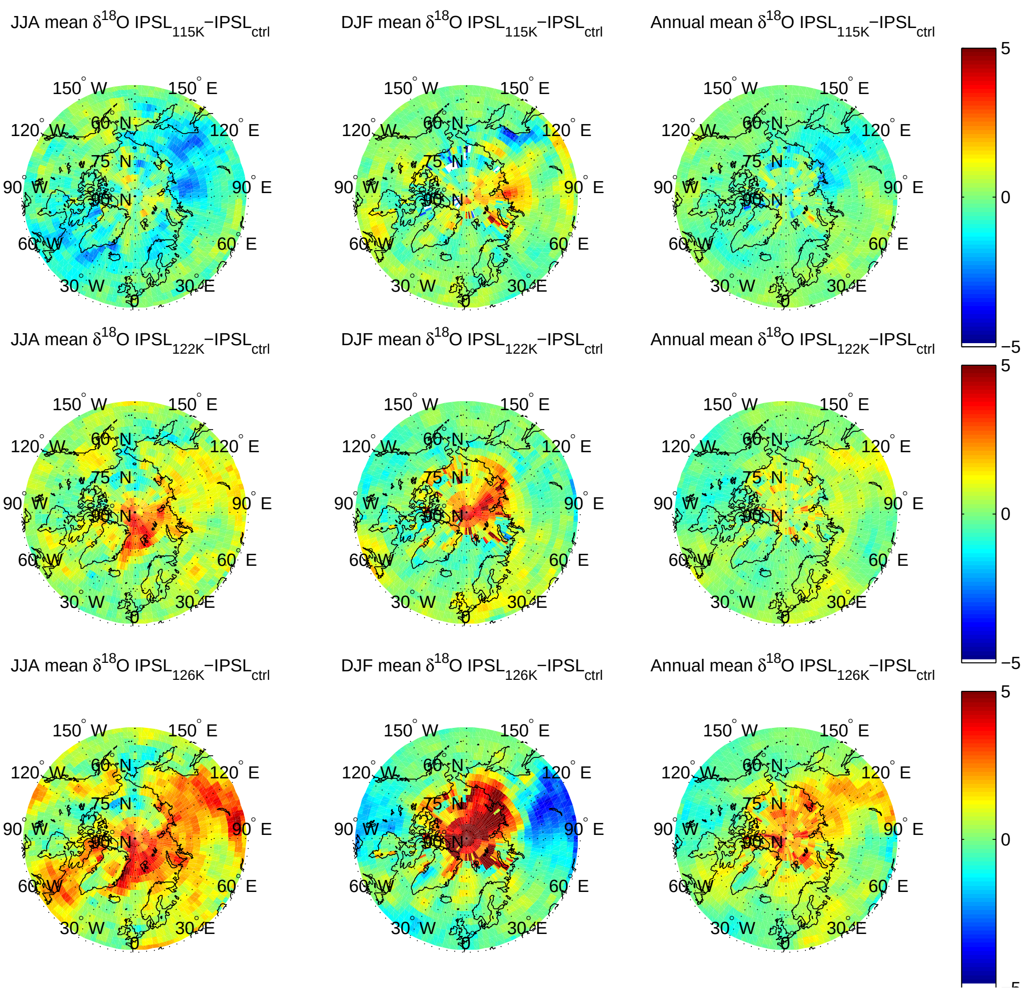

Figure 3.10: ECHAM$_{iso}$ mean precipitation weighted δ^{18}O anomaly [‰] for June, July and August (JJA), December, January and February (DJF) and annual mean anomaly for the Northern Hemisphere for time slices 115kyr (top), 122kyr (middle) and 126kyr (bottom).

The JJA anomaly shows up to $+5^oC$ over continental areas and up to $+3^oC$ Norwegian, Greenland and Labrador Sea, as well as up to $+1^oC$ in the North Atlantic. The magnitude and geographical distribution of the modeled JJA anomaly is in agreement with what what found in the CAPE interglacial study [Anderson et al., 2006] (see Figure 3.1). Because of the decrease in winter insolation there is cold anomaly down to -5^oC over North America and Siberia, while where is a clear warm anomaly of $+5^oC$ over the Arctic Ocean caused by a large deficit in sea ice cover compared to the IPSL$_{ctrl}$ run. For the annual mean the positive anomaly over the Arctic Ocean is the most notable. This means that apart from an increase in the amplitude of the annual cycle, there is a persistent effect of the positive summer insolation anomaly that lasts all year round due to the sea ice feedbacks.

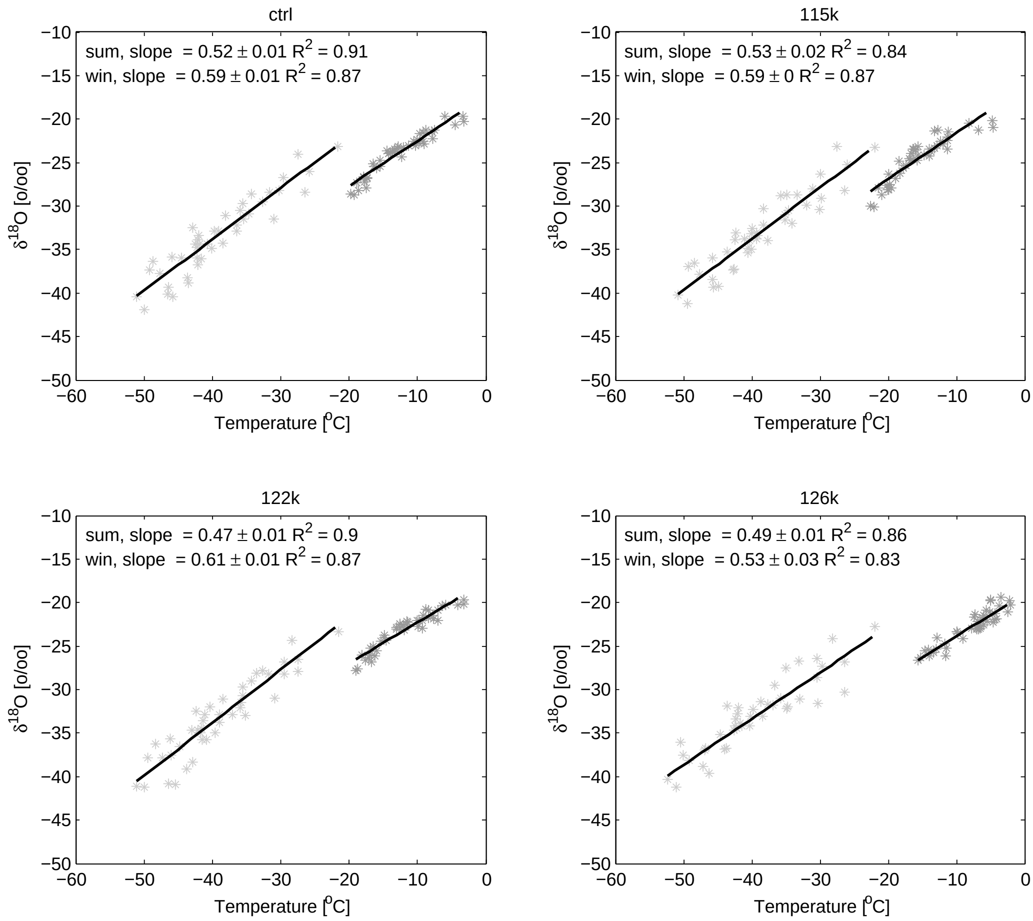

Figure 3.11: The ECHAM$_{iso}$ spatial temperature-δ^{18}O slope during summer (Jun-Aug) and winter (Dec-Feb) for Greenland above 1500m elevation.

Figure 3.10 shows the seasonal and annual anomaly for δ^{18}O. Looking at the spatial pattern of the DJF mean anomaly for all three time slices, the pattern corresponds very well to the temperature anomaly shown in Figure 3.9.

This is not the case for the JJA δ^{18}O anomalies. While the JJA δ^{18}O in general is more and more depleted, going from the IPSL$_{126k}$, to the IPSL$_{115k}$ run, there is less coherence between the δ^{18}O and temperature anomaly patterns for JJA than for DJF. This is in agreement with the temperature dependence of δ^{18}O in general being a winter signal.
The temporal relation between temperature and δ^{18}O for ECHAM$_{iso}$ is discussed further in Section 3.3.4, while for the time being the spatial temperature-δ^{18}O relation is shown in Figure 3.11 for Greenland. The spatial slopes show that the dependence of δ^{18}O on temperature is indeed smaller during summer, although the data actually show more scatter during winter. Moreover is there a tendency for the IPSL$_{122k}$ and IPSL$_{126k}$ to have lower slopes than the two other runs.
Since the main effect of the insolation anomalies for the Northern Hemisphere is during summer, and thus the largest impact on the temperatures also during summer, the relative insensitivity of the δ^{18}O to summer temperatures limits the signature of the warmer summer temperatures in the annual δ^{18}O anomaly.
The annual mean change in the δ^{18}O anomaly for Greenland is thus very limited with very little amplitude between the three Eemian time slices and the IPSL$_{ctrl}$ run. For the IPSL$_{115k}$ run there is a negative anomaly of around -1‰ in central eastern Greenland, with no change for the rest of Greenland. A positive anomaly of +1‰ for Northern Greenland is seen for the IPSL$_{122k}$ run, with no change for the rest of Greenland. In the last time slice, the IPSL$_{126k}$, there is a positive δ^{18}O anomaly of 1-2‰ in northeastern Greenland, with even slightly negative anomalies is seen in western Greenland, because of the lower δ^{18}O during winter. Maps of Eemian anomalies for Greenland, Figures B.1 to B.4, are placed in Appendix B.1. The Greenland δ^{18}O anomalies will be discussed further in relation to ice core data in Section 3.3.5.

3.3.2 Southern Hemisphere anomalies

Opposed to the Northern Hemisphere the Southern Hemisphere did not experience any increase in summer insolation during the Eemian. This is also shown in Figure 3.8. For the IPSL$_{115k}$ run the insolation is actually very close to the IPSL$_{ctrl}$ run. Despite the similar insolation there are significant temperature anomalies for the IPSL$_{115k}$ run (see Figure 3.12). Most noticeable is the warm anomaly of up to $+5^oC$ in the Ross Sea and the cold anomaly down to -5^oC in the Weddell Sea during the austral winter (JJA). This is due to a different sea ice configuration during the IPSL$_{115k}$ run. Also seen is a warm anomaly for West Antarctica, mostly present during JJA, which is

probably connected to the decrease in sea ice seen for the Ross Sea. Over all there is a slight negative anomaly for East Antarctica.
The temperature anomalies during winter (JJA) for the IPSL_{122k} run show positive values for both the Weddell and Ross Sea, which is again connected with sea ice anomalies. The temperature anomaly for West Antarctica is less pronounced compared to the IPSL_{115k} run, and there is a general cooling over Antarctica during summer (DJF) of up to 2^oC.

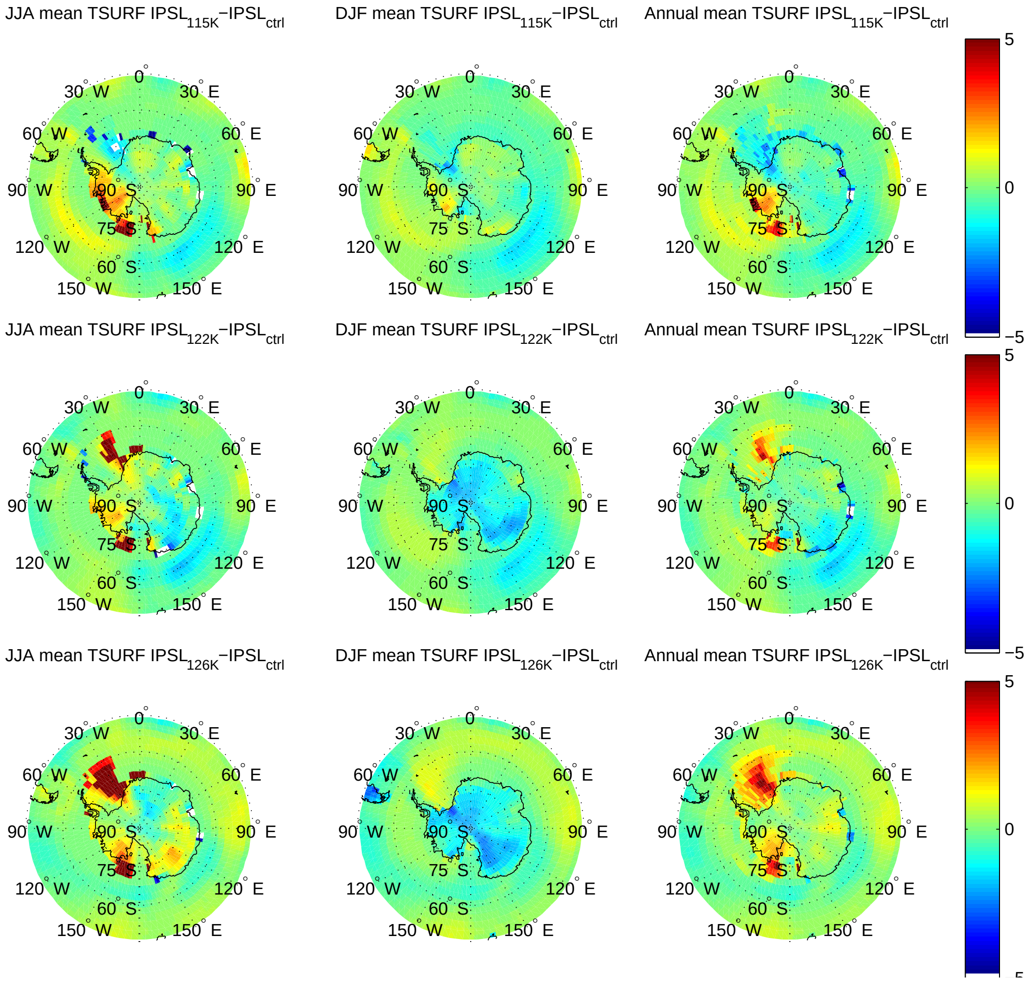

Figure 3.12: ECHAM_{iso} mean surface temperature anomaly $[^oC]$ for June, July and August (JJA), December, January and February (DJF) and annual mean anomaly for the Southern Hemisphere for time slices 115kyr (top), 122kyr (middle) and 126kyr (bottom).

For the IPSL_{126k} run the positive JJA anomaly over the Ross Sea is even more widespread, as well as a positive JJA anomaly over East Antarctica towards the coast of up to 2^oC. Even with a general cooling for Antarctica during summer (DJF) this leads positive annual anomalies for the Antarctic continent of up to 1^oC in East Antarctica and up to 2^oC in West Antarctica.

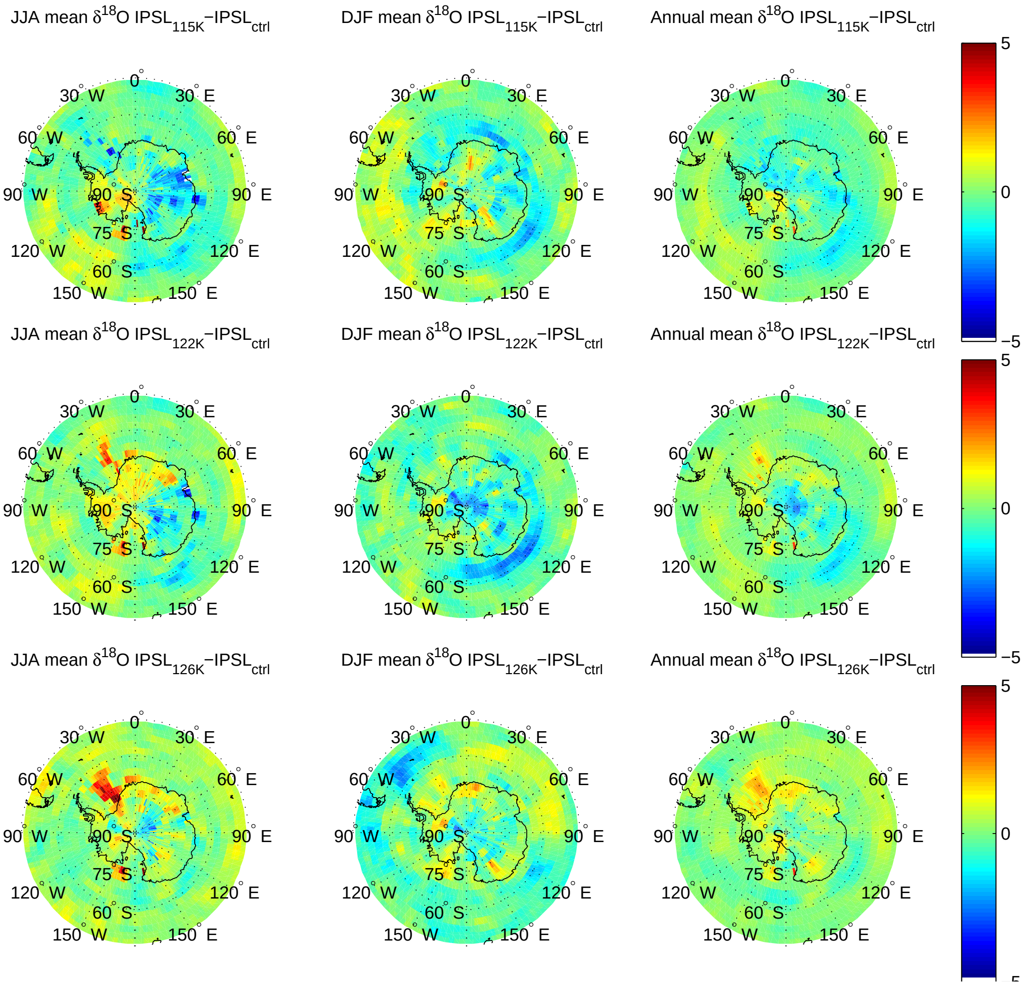

Figure 3.13: ECHAM$_{iso}$ mean precipitation weighted δ^{18}O anomaly [‰] for June, July and August (JJA), December, January and February (DJF) and annual mean anomaly for the Southern Hemisphere for time slices 115kyr (top), 122kyr (middle) and 126kyr (bottom).

In general for all the three Eemian time slices the JJA temperatures over the Ross Sea seem to be linked to the JJA temperatures of the Northern Hemisphere. That is, the IPSL$_{115k}$ run has negative anomalies for the boreal summer, with progressively larger anomalies for the IPSL$_{122k}$ and IPSL$_{126k}$

run. This pattern is also seen for the temperatures over the Ross Sea. This could be explained by the increased insolation of the Northern Hemisphere not only making the Northern Hemisphere summers warmer, but also heating up regions in the Southern Hemisphere through heat exchange by the atmosphere and the Atlantic Ocean.
Compared to the cold regions in Northern Hemisphere the δ^{18}O anomalies of central Antarctica are noisy with a large scatter in values for adjacent grid points. This is because of the very low accumulation in central Antarctica, where individual precipitation events can make large difference in the mean values.

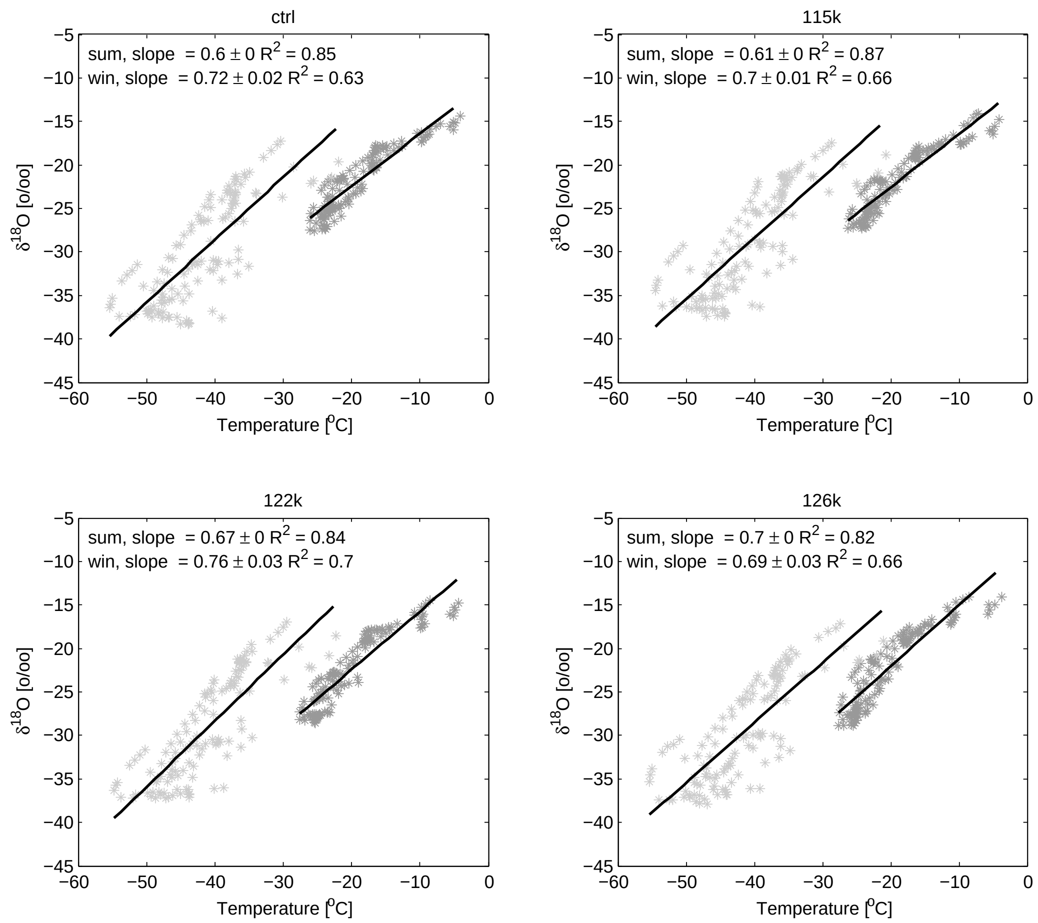

Figure 3.14: The ECHAM$_{iso}$ spatial temperature-δ^{18}O slope during summer (Dec-Feb) and winter (Jun-Aug) for West Antarctica above 500m elevation.

The climate response for Antarctica in the δ^{18}O during the Eemian is as for Greenland rather limited. For all tree time slices there is a positive annual anomaly for West Antarctica in the +1‰ range, which can be related to the decrease in sea ice for the Weddell Sea in case of the IPSL$_{115k}$ run, and a decrease in sea ice for both the Ross Sea and Weddell sea for the IPSL$_{122k}$ run and IPSL$_{126k}$ run. The IPSL$_{126k}$ run show general positive δ^{18}O anomalies in the 1-2‰ range towards coastal regions in East Antarctica and for West Antarctica, while the IPSL$_{122k}$ run has scattered positive anomalies along the coast and a negative anomaly of -2‰ near the south pole. These anomalies will be discussed further in relation to ice core data in Section 3.3.5.

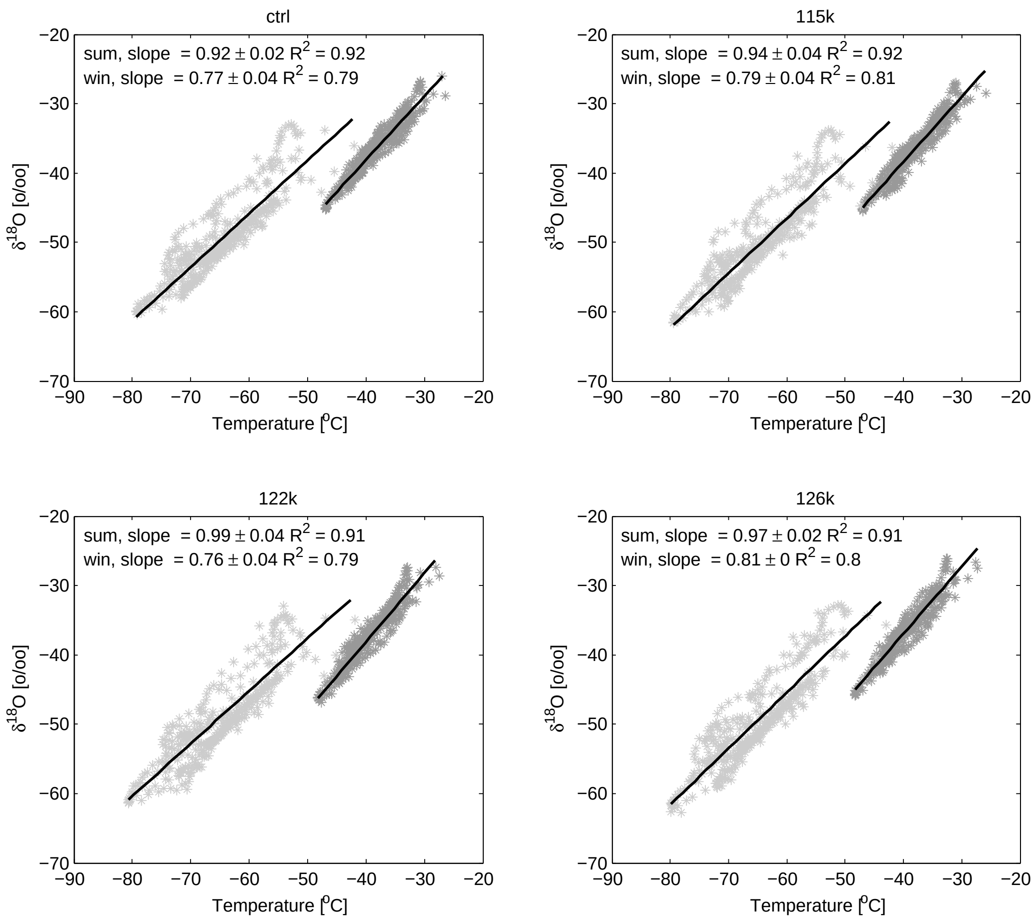

Figure 3.15: The ECHAM$_{iso}$ spatial temperature-δ^{18}O slope during summer (Dec-Feb) and winter (Jun-Aug) for East Antarctica above 2500m elevation.

The temperature-δ^{18}O spatial slopes were also calculated for Antarctica. Because of the different climate, and climate response, of East and West Antarctica the slopes were calculated separately for these two regions. Compared to Greenland there is less coherency (smaller R^2) during winter between temperature and δ^{18}O (see Figure 3.15 and 3.14).
As for Greenland the slopes for West Antarctica are smaller during summer than during winter, with the exception of the slope for the $IPSL_{126k}$ run where the slopes basically are equal. Opposed to Greenland the slopes are steeper for the $IPSL_{122k}$ and $IPSL_{126k}$ runs.
The East Antarctic slopes differ from the slopes of Greenland and West Antarctica by consequently having higher summer slopes than winter. The slope is also steeper for the $IPSL_{122k}$ and $IPSL_{126k}$ runs, however only significantly during summer.

3.3.3 The sea ice annual cycle

The representation of sea ice in the $ECHAM_{iso}$ experiments was discussed in Section 3.2 and 3.2.1. Since only ocean areas of 100% sea ice coverage are represented in the Eemian experiments, the anomalies discussed here also only concern the changes in the areas of 100% sea ice coverage. The general under estimation of the sea ice cover, originating from the bias in the IPSL_CM4 and the adaptation of SSTs in $ECHAM_{iso}$, does without a doubt lead to physical inconsistencies in the experiments. However, even with these problems important information can be drawn from analyzing the differences in sea ice cover between the Eemian time slices.
The Arctic Ocean becomes ice free in August for all of the experiments, even in the $IPSL_{115k}$ run which overall has more sea ice than the $IPSL_{ctrl}$ run (see Figure 3.16). This is of course caused by the sea ice representation discussed above. Generally the sea ice extend of the time slices agrees well with the overall climate differences between the runs. That is, the increased summer insolation of the $IPSL_{122k}$ run and $IPSL_{126k}$ run yield less total sea ice cover. In case of these two runs the decrease in maximum winter ice extend is about 10% and 20%, respectively. So, the winter sea ice is not able to recover from the negative summer sea ice anomalies.
For the Eemian climatic optimum, as simulated in the $IPSL_{126k}$ experiment, the Arctic Ocean is ice free from June til September. Again because of the sea ice representation, this means that there are no grid points with 100% sea ice cover during these months. According to Anderson et al. [2006] the Arctic sea ice was indeed significantly reduced during the Eemian, with the permanent sea ice margins far from the coastal boundaries of the Arctic Ocean, but the central Arctic Ocean was not ice free during the Eemian.

As mentioned in Section 3.2.1 the sea ice around Antarctica is underestimated both in extend and concentration by the IPSL_CM4 model. Together with the adaptation to the ECHAM$_{iso}$ this means, that for the IPSL$_{ctrl}$ and the Eemian runs, sea ice is only present in the Weddell and Ross Sea, which in turn means that sea ice anomalies are confined to these regions. This produced the large local temperature anomalies seen in Figure 3.12.

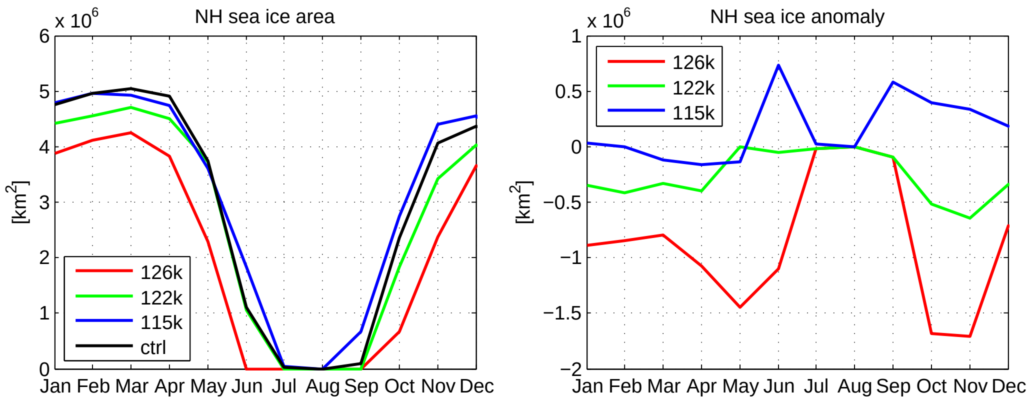

Figure 3.16: The Northern Hemisphere sea ice annual cycle for the IPSL$_{ctrl}$ run and the three Eemian time slices (left). Also plotted is the annual cycle of the Eemian sea ice anomalies (right).

In contrast to the Northern Hemisphere the IPSL$_{115k}$ run also shows a general negative anomaly in sea ice. Although there is an increase of sea ice in the Weddell Sea the decrease in sea ice in the Ross Sea more than compensates for this, giving the over all negative anomaly. In the IPSL$_{115k}$ run there is a positive temperature anomaly of 1^oC in the southern Pacific and the Southern Ocean between 90^oW and 150^oW, which could be part of a regional warm anomaly including the negative sea ice anomaly in the Ross Sea as well as the warming of West Antarctica (see also Figure 3.12).
The Southern Hemisphere did not experience positive insolation anomalies during summer (see Figure 3.8). However, the mean annual insolation was increased for 65^{o}S (in the same manner as 65^{o}N) due to the higher obliquity (see Figure 3.3). Slightly higher ocean temperatures in the waters around Antarctica are probably responsible for the general decrease in sea ice. Also, heat exchange with the Northern hemisphere could provide additional energy to decrease the Southern Hemisphere sea ice cover in the IPSL$_{122k}$ and IPSL$_{126k}$ run. This of course does not explain the negative sea ice anomaly for the IPSL$_{115k}$ run. This would require a more in depth analysis of the of the ocean component of the IPSL_CM4 model, which is beyond the scope

of this study.

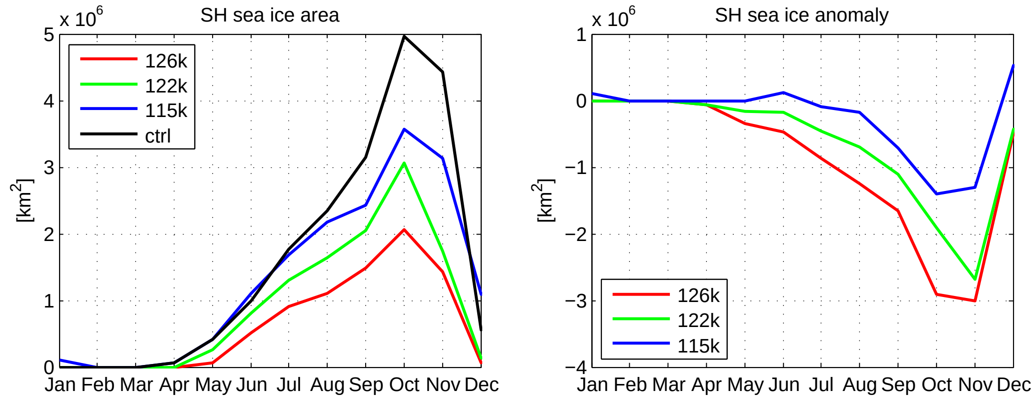

Figure 3.17: The Southern Hemisphere sea ice annual cycle for the IPSL$_{ctrl}$ run and the three Eemian time slices (left). Also plotted is the annual cycle of the Eemian sea ice anomalies (right).

3.3.4 The annual cycle of temperature, precipitation, δ^{18}O and d-excess

In this section we take a closer look at the changes in the mean annual cycle over Greenland and Antarctica. The analysis is limited to three areas, namely, Greenland above 1500m elevation, West Antarctica above 500m elevation and East Antarctica above 2500m elevation. These three areas are interesting both in relation to comparison to ice core records and to the mass balance of the ice sheets.

The temperature annual cycle for Greenland largely mimics the insolation anomaly of the Northern Hemisphere, where the amplitude is decreased for the IPSL$_{115k}$ run, and increased in the IPSL$_{122k}$ and IPSL$_{126k}$ run (see Figure 3.18). The anomaly of the summer peak for the three runs are -3^oC, 3.5^oC and 6^oC, respectively.

The temperature anomalies for Antarctica are less significant. However, there are some interesting differences between East and West Antarctica. West Antarctica has generally more positive anomalies, and during the austral winter West Antarctica has warm anomalies for the IPSL$_{122k}$ and IPSL$_{126k}$ run, which in the annual cycle precede the anomalies in the insolation for the Southern Hemisphere. This can be attributed to the negative anomalies in the Southern Hemisphere sea ice cover, which in Section 3.3.3 were found to be connected to the positive annual mean insolation anomalies, as well as possibly connected to the positive boreal summer anomalies.

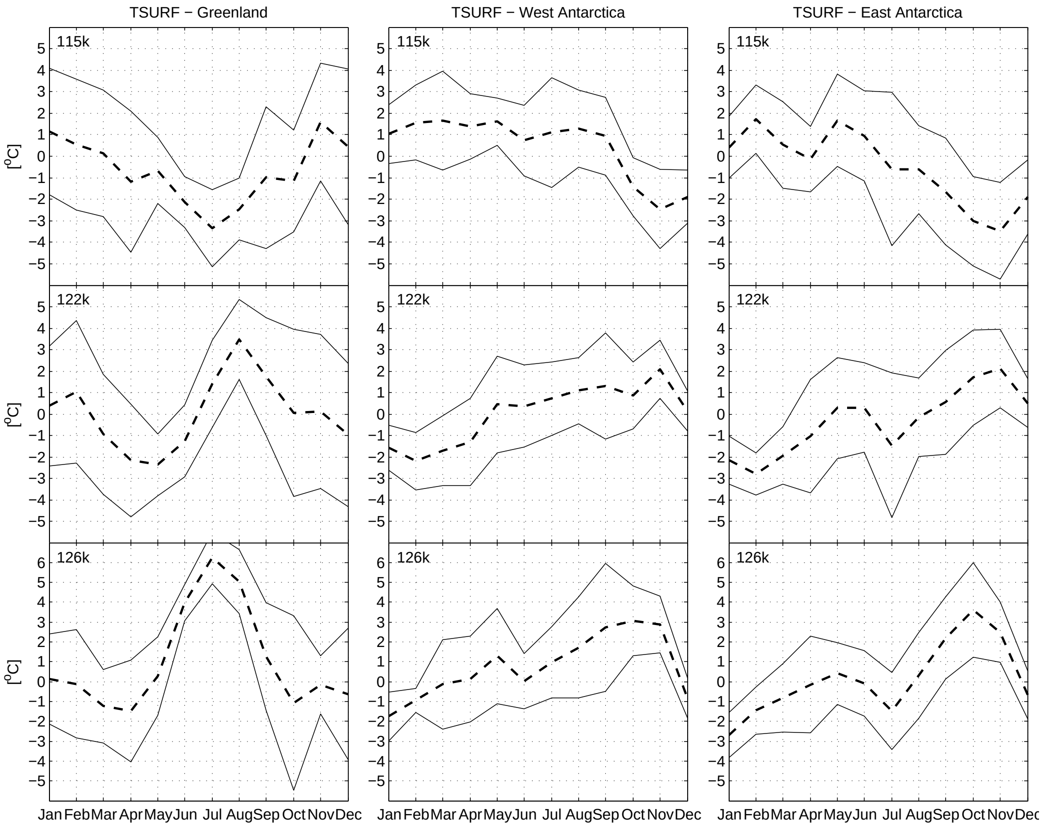

Figure 3.18: The annual cycle of the ECHAM$_{iso}$ surface temperature anomaly for Greenland above 1500m elevation, West Antarctica above 500m elevation and East Antarctica above 2500m elevation for time slices 115kyr (top), 122kyr (middle) and 126kyr (bottom). The dashed line is the mean monthly values and the full lines are $\pm$ one standard deviation based on 10 years of simulation.

The summer anomalies for Greenland in the IPSL$_{122k}$ run and in particular the IPSL$_{126k}$ run are large enough to cause additional melting during summer, affecting the mass balance of the Greenland Ice Sheet (GIS) negatively [Gregory et al., 2004]. Also, in a recent publication by Vinther et al. [2009] a significant thinning of GIS during the Holocene climatic optimum was found based on several ice core δ^{18}O records. With the even greater Northern Hemisphere summer insolation anomalies of the early Eemian compared to the Holocene, this supports the idea that GIS was significantly reduced dur-

ing the Eemian compared to present.
The heating of West Antarctica contrasts that of GIS as the heating occurs during austral winter, which does not result in any additional melting as the temperature is well below the freezing point. However, the decrease in sea ice around Antarctica and the associated warmer ocean temperatures could lead to a break down of the large ice shelves and subsequently to instability of the West Antarctic Ice Sheet [Rignot and Jacobs, 2002].

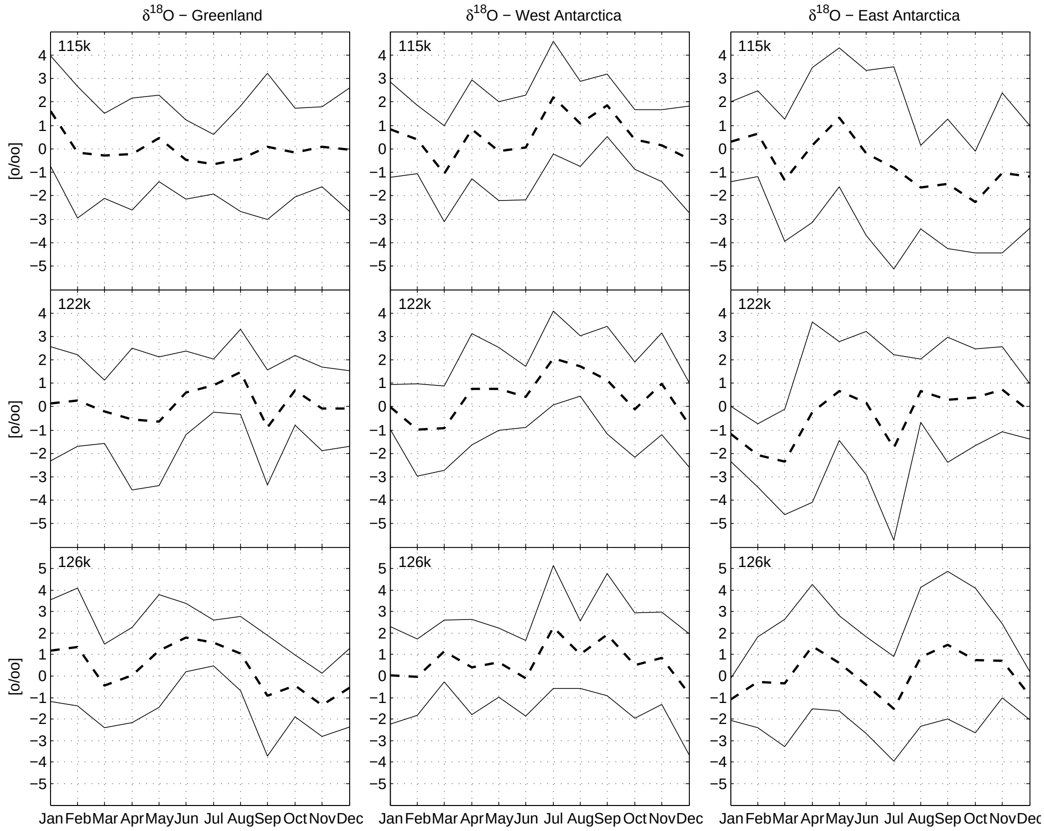

Figure 3.19: The annual cycle of the ECHAM$_{iso}$ δ^{18}O anomaly for Greenland above 1500m elevation, West Antarctica above 500m elevation and East Antarctica above 2500m elevation for time slices 115kyr (top), 122kyr (middle) and 126kyr (bottom). The dashed line is the mean monthly values and the full lines are $\pm$ one standard deviation based on 10 years of simulation.

The δ^{18}O response to the temperature anomalies are in general relative weak for all of the areas, if seen in relation to the observed Greenland spatial temperature-δ^{18}O slope of $0.67‰/^oC$ [Johnsen et al., 1989]. However, the spatial relationship is thought not to hold when dealing with temporal changes in climate [Johnsen et al., 2001]. Therefore the temporal slope for monthly model out put was calculated seasonally for each of the three regions, and for each time slice (see Table 3.1). The temporal ECHAM$_{iso}$ slopes for Greenland agree fairly well with the present day slope of $0.46‰/^oC$ found by Shuman et al. [1995] based on observations.

Area	Temporal slope summer/winter			
	ctrl	115k	122k	126k
Greenland	0.34/0.56	0.34/0.61	0.30/0.59	0.28/0.52
West Antarctica	0.34/0.60	0.36/0.40	0.33/0.45	0.33/0.49
East Antarctica	0.51/0.80	0.52/0.72	0.51/0.62	0.45/0.63

Table 3.1: The seasonal temporal δ^{18}O-temperature slope [$‰/^oC$] calculated from monthly ECHAM$_{iso}$ output averaged for the same three polar regions as in Figure 3.18 and 3.19. Summer and winter is defined as May-Oct and Nov-Apr, respectively, for Greenland and vice versa for Antarctica.

The slopes found here for Greenland and West Antarctica are generally of similar magnitude, while steeper slopes are found for East Antarctica. A clear seasonal difference for all regions and time slices is that the summer slope always is somewhat smaller than the winter slope, which corresponds to a weaker temperature control on δ^{18}O during summer. Additionally, there is a tendency for the slopes to be lower for the IPSL$_{122k}$ and IPSL$_{126k}$ run, which is strongest during summer in Greenland and during winter for Antarctica.
For Greenland the δ^{18}O anomaly for the IPSL$_{115k}$ run is very flat and only show slightly elevated values in January (see Figure 3.19). The January anomaly could be associated with the warmer winter temperatures, but compared with the standard deviation these features are hardly significant. In the IPSL$_{122k}$ and IPSL$_{126k}$ run there is a positive anomaly in the boreal summer δ^{18}O. The magnitude of these anomalies are in approximate agreement with the temporal temperature-δ^{18}O slopes listed in Table 3.1. For example does the $+6^oC$ temperature anomaly for the IPSL$_{126k}$ run translate into a $+2‰$ δ^{18}O anomaly, which corresponds to a temporal slope of $0.33‰/^oC$.
The West Antarctic δ^{18}O only show minor positive anomalies during austral winter, also in agreement with the seasonal temporal slopes. However, the 126kyr temperature anomaly is not reflected clearly in the δ^{18}O. This could be due to moisture source effects caused by the negative anomalies in Southern sea ice cover giving more open water with cold temperatures.
For East Antarctica the δ^{18}O anomalies seem to reflect the temperatures fairly well, which can be attributed to better temperature control of the isotopes because of general lower temperatures over the high elevation East

Antarctic plateau. This is also reflected in the steeper temporal slopes calculated for East Antarctica. However, the noise level is quite high, which can be seen from the larger standard deviation for East Antarctica compared to $\delta^{18}O$ anomalies for West Antarctica and Greenland. The signal is more noisy from East Antarctica because of very low precipitation.

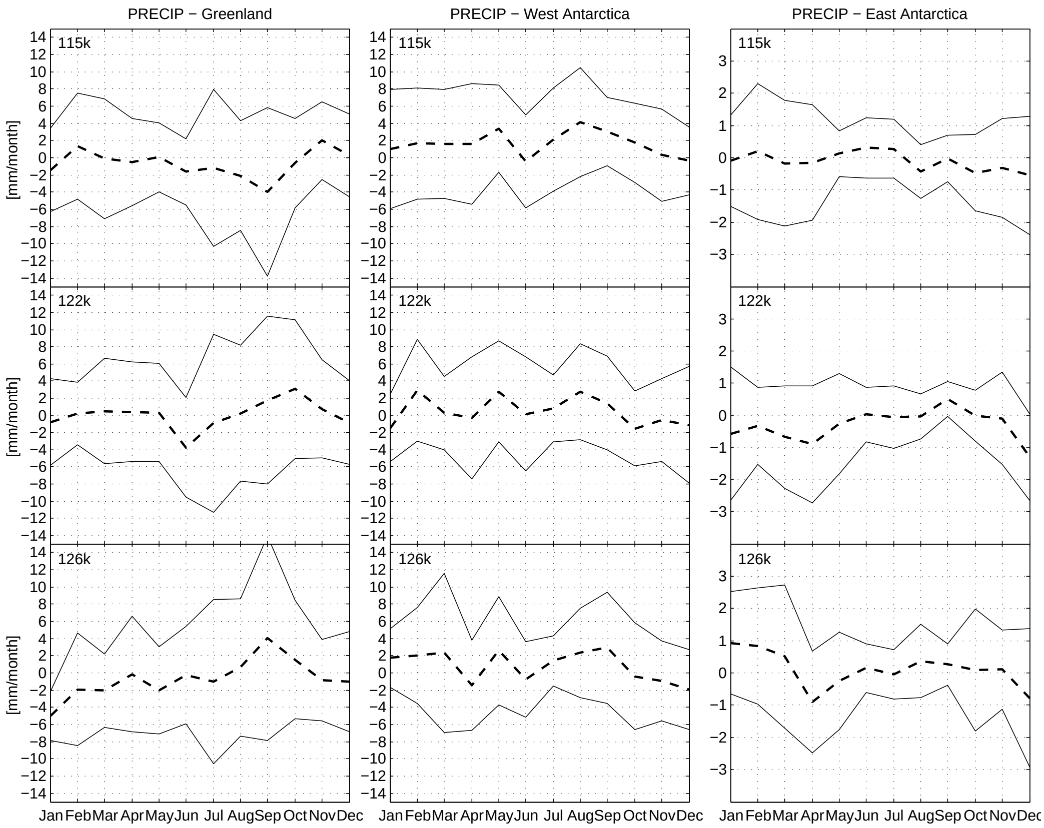

Figure 3.20: The annual cycle of the ECHAM$_{iso}$ precipitation anomaly for Greenland above 1500m elevation, West Antarctica above 500m elevation and East Antarctica above 2500m elevation for time slices 115kyr (top), 122kyr (middle) and 126kyr (bottom). The dashed line is the mean monthly values and the full lines are ± one standard deviation based on 10 years of simulation. Note that the scale on the ordinate of the plots for East Antarctica is different from the scale used in the plots for Greenland and West Antarctica.

The precipitation signal is in general a more noisy signal than for example temperature and the anomalies for the Eemian experiments do not exceed the standard deviation (see Figure 3.20). Overall the Greenland precipitation follows the temperature, in that the time slices with higher temperature have more precipitation. However, it is not a simple relation. For the IPSL_{126k} run there is negative anomalies during boreal winter and positive anomalies for the late summer/autumn. The decrease in winter precipitation could be caused by less storminess due to a reduction of the meridional gradient, while the increased summer/autumn precipitation could be due to thermodynamics as the temperatures are higher in the IPSL_{126k} run.

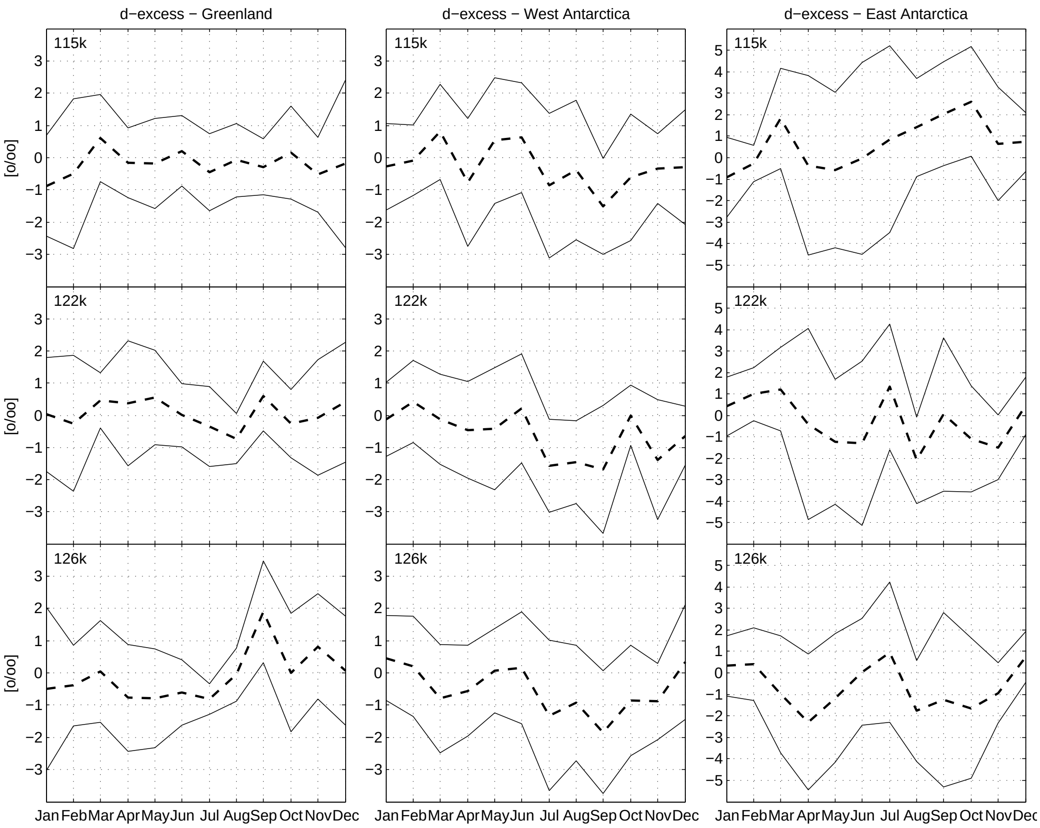

Figure 3.21: The annual cycle of the ECHAM_{iso} d-excess anomaly for Greenland above 1500m elevation, West Antarctica above 500m elevation and East Antarctica above 2500m elevation for time slices 115kyr (top), 122kyr (middle) and 126kyr (bottom). The dashed line is the mean monthly values and the full lines are $\pm$ one standard deviation based on 10 years of simulation. Note that the scale on the ordinate of the plots for East Antarctica is different from the scale used in the plots for Greenland and West Antarctica.

The West Antarctic precipitation anomalies are generally positive, and do not seem to be connected to the anomalies in the temperature annual cycle.

Also for East Antarctica the anomalies have no clear pattern. The anomalies for East Antarctica are much smaller in magnitude due to the smaller precipitation in inland Antarctica.
The d-excess anomalies to a large extend mirror the δ^{18}O anomalies (see Figure 3.21). As discussed in Section 2.3.2 the d-excess increases when the precipitation gets more depleted in ^{18}O, and this relation gets stronger for very low δ^{18}O values. This explains why the most clear anticorrelation between δ^{18}O and d-excess is seen for East Antarctica.
One thing stands out when looking over the d-excess anomalies, namely the IPSL_{126k} run. Most of the year the anomalies are fairly flat except for September, which has a 2‰ peak. This peak coincides with the peak found in the precipitation anomalies, while no large response is seen in δ^{18}O. Moisture source effects could explain this, if either the source temperature increased while having no change in distillation path or the relative humidity decreased due to a more northern source area.

3.3.5 Eemian stable water isotopes: ECHAM_{iso} compared with ice core data

In this section a direct comparison between stable water isotope ice core data from NorthGRIP, Dome C and Vostok, and ECHAM_{iso} output is presented [Andersen et al., 2004, Jouzel et al., 2007, Petit et al., 1999]. The ECHAM_{iso} has been weighted with precipitation, so with a perfect simulation the model data should in principle show the same as the ice core data. At a first glance it is evident that these model experiments are not perfect (see Figure 3.22). The amplitude of the modeled anomalies are not of the same magnitude as in the ice core data. For NorthGRIP the δ^{18}O anomalies do seem to tell the same story as the ice core data, with the IPSL_{115k} time slice having the lowest δ^{18}O, but the amplitude is off by about a factor of 5. For the Antarctic ice cores the model shows the IPSL_{115k} time slice as having the lowest δD, and taking the size of the errorbars in to account the anomalies are hardly significant.
Given the shifts of δD in the ice core data the temperature anomalies for Antarctica should be of similar magnitude as the changes seen for Greenland [Jouzel et al., 2007]. The results shown in Section 3.3.2 and 3.3.4 for Antarctica give a different story. This shows that the simplistic setup of the experiments lack significant parts of what made up the climate during the Eemian interglacial, assuming that ECHAM_{iso} would provide correct results given the right boundary conditions. Even though there are signs of links between the changes seen in the Northern Hemisphere and in the Southern

Hemisphere for the model results, for example in the Southern Hemisphere sea ice cover, the climate anomalies seen for Antarctica are far from significant. Major feedbacks and teleconnections are therefore not accounted for. This of course not only questions the setup of the ECHAM$_{iso}$ experiments, but also the setup of the IPSL_CM4 coupled model. This subject will be discussed further in Section 3.6.

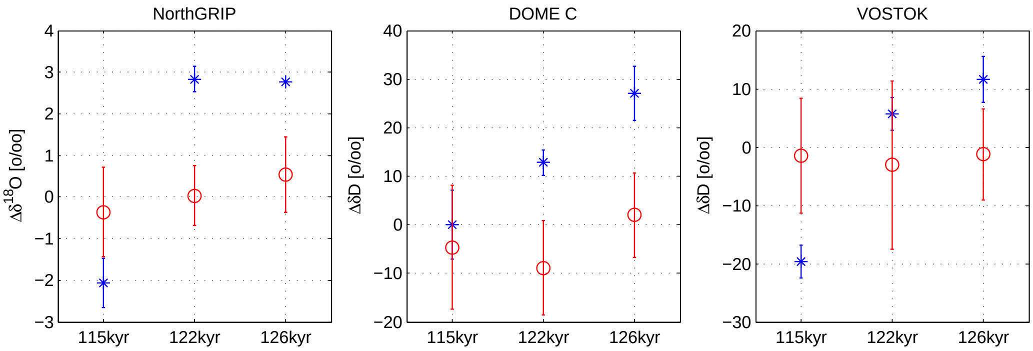

Figure 3.22: Precipitation weighted annual mean ECHAM$_{iso}$ stable water isotope anomalies (red) compared with NorthGRIP δ^{18}O, DOME C δD and VOSTOK δD anomalies (blue) for the three Eemian time slices. The errorbars on the model data are one standard deviation calculated from 10 years of simulation, and the errorbars on the ice core data is one standard deviation for $\pm$ 1000 years of data to accommodate dating uncertainties. There are no errorbars on the NorthGRIP 126kyr ice core data, as this is data from the very bottom of the core.

3.3.6 The sensitivity of the isotopic signal relative to temperature and precipitation

From the results presented in Section 3.3.1, 3.3.2 and 3.3.4 it is clear that the relation between the modeled δ^{18}O and temperature is not constant in neither space nor time. This goes for both seasonal changes in the δ^{18}O-temperature relation as well as differences in the δ^{18}O-temperature relation for the Eemian time slices. The pattern seen so far is that in general there is less temperature control on the δ^{18}O during summer than during winter, and that the δ^{18}O anomalies for the cold East Antarctic plateau were closer connected to temperature anomalies than for other regions. This basically sums up to that in the ECHAM$_{iso}$ experiments the δ^{18}O is tied stronger to the temperature when it is cold. This is not a surprising conclusion, as this is also what is seen for winter versus summer data in other model experiments and in ice core data (see Section 2.2.1 and [Vinther et al., 2008]. However, in this section an attempt is made to understand what this means for the interpretation of the isotopic signal during a warmer climate such as the Eemian.

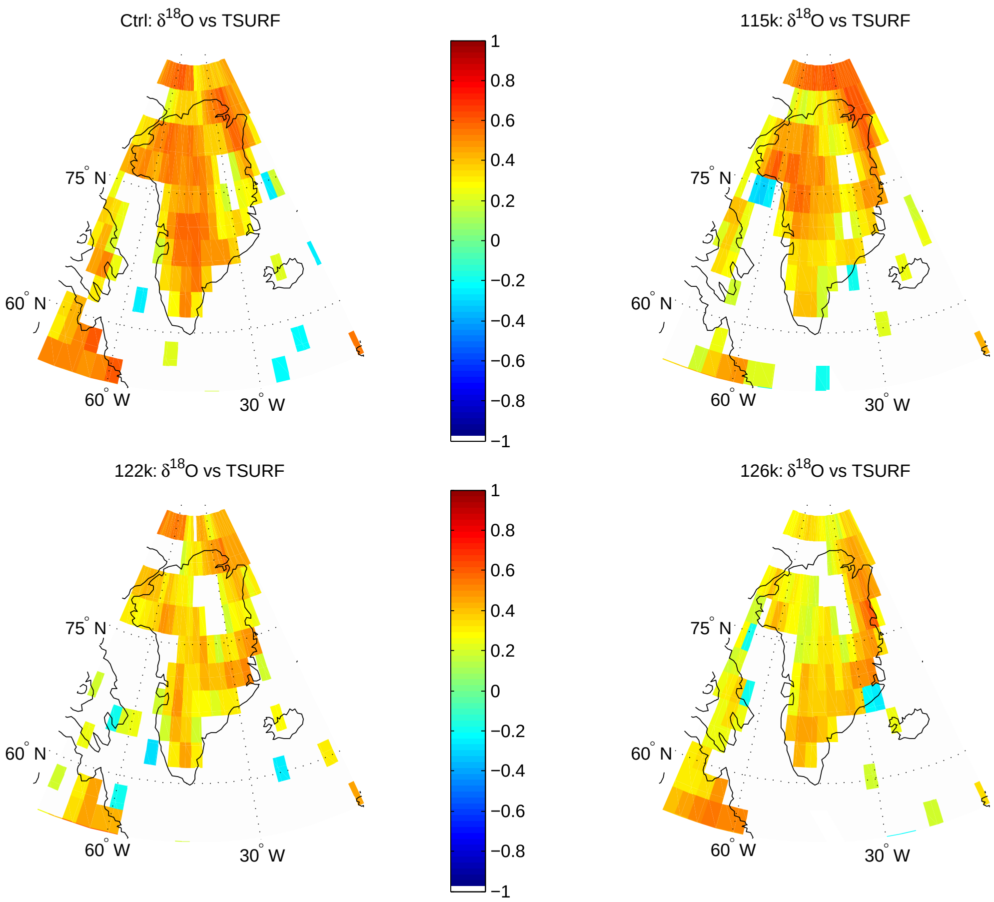

Figure 3.23: The linear correlation between monthly anomalies of surface temperature and δ^{18}O for the IPSL$_{ctrl}$, IPSL$_{115k}$, IPSL$_{122k}$ and IPSL$_{126k}$ run zoomed on Greenland. The correlation map is done by subtracting the mean annual cycle from the monthly data series for each grid point and then calculating the correlation. Data points with non-significant correlation coefficients ($p > 0.05$) have been masked out.

Since the ECHAM$_{iso}$ runs in this study are fairly short as well as using climatological SSTs, the options for investigating the variability are limited. Therefore a study of the correlation between the monthly δ^{18}O and surface

temperature was made, where the mean annual cycle was removed from the data prior to calculating the correlation. This should give an idea of how the δ^{18}O variability behaves in relation to temperature in the Eemian time slices.
In Figure 3.23 correlation maps for the IPSL$_{ctrl}$ run and the Eemian time slices are shown for Greenland. The maps in Figure 3.23 show a significant change in the correlation patterns from the IPSL$_{ctrl}$ run to the Eemian time slices. The pattern for the IPSL$_{ctrl}$ run is quite similar to the results shown for REMO$_{iso}$ in Section 2.2.1, with predominately positive correlations of R=0.4 to R=0.6 except for eastern Greenland, where low or no correlation dominates. The pattern is similar for the IPSL$_{115k}$ run except that the correlations for southern Greenland are significantly lower. For the IPSL$_{122k}$ and IPSL$_{126k}$ run the correlations for the northern and central areas are progressively weaker. However, in southern Greenland the correlation are higher for the IPSL$_{126k}$ run compared to the two other Eemian runs.
One important factor in the correlation of δ^{18}O and temperature is the temperature-precipitation relationship. In Appendix B.2 correlation maps between surface temperature and precipitation as well as correlation maps between δ^{18}O and precipitation can be found. For the IPSL$_{126k}$ run the highest correlation are found towards the southeastern coast, while for all other runs also have high correlations in central and west Greenland.
The conclusions to be drawn so far is that the time slices with the warmer summer temperatures, namely the IPSL$_{122k}$ and IPSL$_{126k}$ run, have less of the temperature signal preserved in the δ^{18}O for Greenland precipitation. This is in agreement with the generally lower temporal temperature-δ^{18}O slopes for found for Greenland in Section 3.3.4.
For Antarctica the changes in correlation between temperature and δ^{18}O are less dramatic, which can be expected since the differences in climate in general are less for Antarctica than for Greenland in the Eemian experiments. However, both the IPSL$_{122k}$ and IPSL$_{126k}$ run show lower correlations than the two other runs. The correlations between temperature and precipitation also show little change between the different time slices, and stronger correlations are found for Antarctica than for Greenland. Again, the correlation maps between surface temperature and precipitation as well as correlation maps between δ^{18}O and precipitation can be found in Appendix B.2. Again this weakened temperature-isotope relation for the IPSL$_{122k}$ and IPSL$_{126k}$ was also found for Antarctica in Section 3.3.4, although not as pronounced as for Greenland.

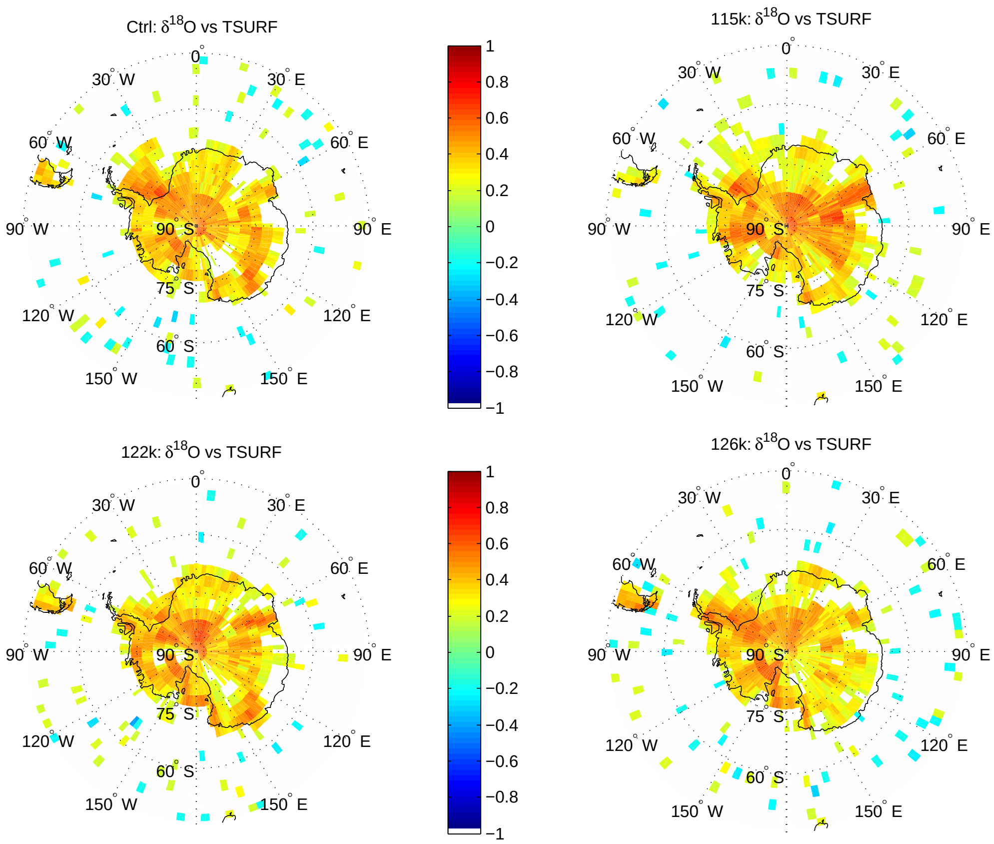

Figure 3.24: The linear correlation between monthly anomalies of surface temperature and δ^{18}O for the IPSL$_{ctrl}$, IPSL$_{115k}$, IPSL$_{122k}$ and IPSL$_{126k}$ run focused on Antarctica. The correlation map is done by subtracting the mean annual cycle from the monthly data series for each grid point and then calculating the correlation. Data points with non-significant correlation coefficients ($p > 0.05$) have been masked out.

3.4 The African and Indian Monsoon system during the Eemian

The extreme seasonality of precipitation in some equatorial areas, referred to as the monsoon, is in broad terms caused by the differential heating of land and ocean areas. Strong heating over land causes convection and inflow of humid air from maritime air masses. This system is modulated by the seasonal changes in the land-ocean temperature gradient. Since the insolation changes during the Eemian caused large seasonal anomalies in insolation, essentially causing a larger seasonal amplitude for the Northern Hemisphere, it is to be expected that the monsoon systems were affected by this. Other studies have shown that this is indeed true when modeling the Eemian using GCMs [Braconnot et al., 2008, Herold and Lohmann, 2009].
The monsoon systems of Africa and India are a major part of the hydrological cycle in these areas, and the focus of this section will be to study changes in the monsoon between the Eemian time slices. There will thus be a good opportunity to compare the results of the monsoon study by Braconnot et al. [2008] to this study, as the ECHAM$_{iso}$ experiments is based on the SSTs from the simulations presented by Braconnot et al. [2008].

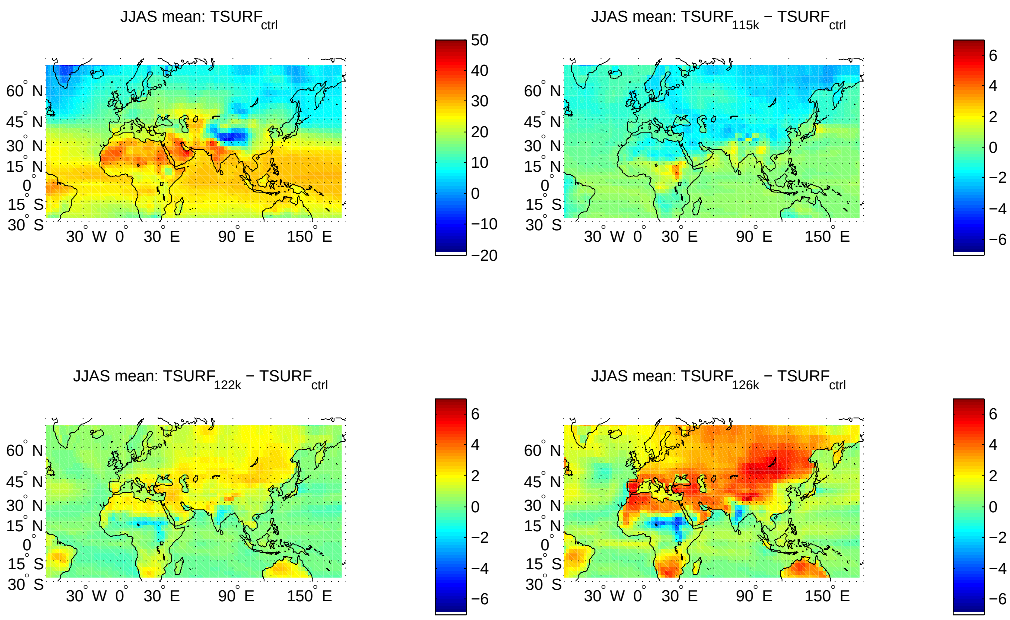

Figure 3.25: The mean JJAS IPSL$_{ctrl}$ surface temperature [^oC] and anomalies for the IPSL$_{115k}$, IPSL$_{122k}$ and IPSL$_{126k}$ run.

The maps presented in this section are July to September (JJAS) means, as this is the main period of the monsoon maximum, and enables a direct comparison with the results of Braconnot et al. [2008]. It should be noted that apart from differences in model physics, differences from running an atmospheric GCM with fixed SSTs to running a coupled atmosphere-ocean is to be expected. Since running with fixed SSTs greatly affects the variability of the monsoon no further study will be done into this.

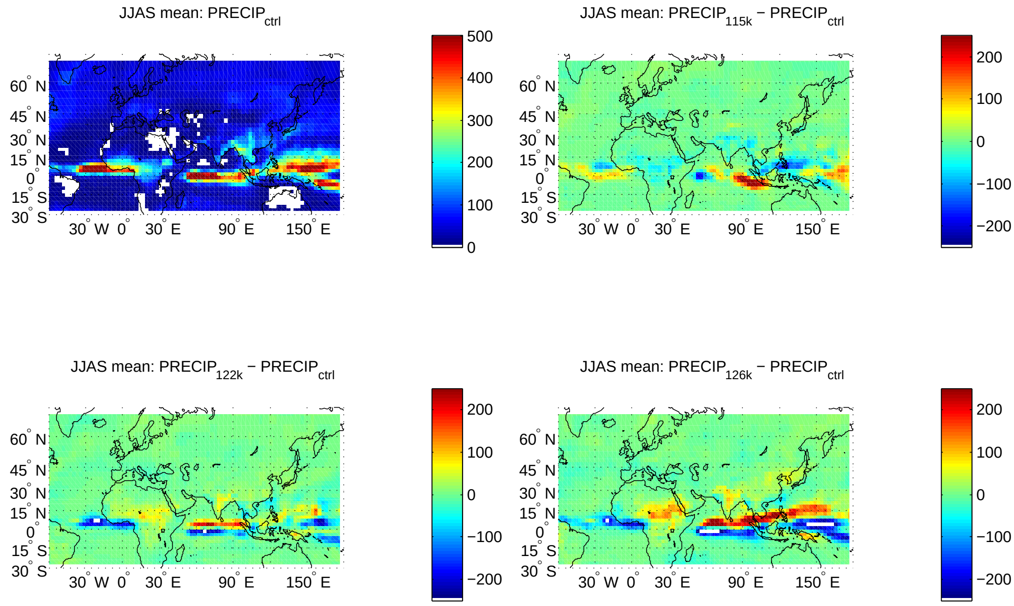

Figure 3.26: The mean JJAS IPSL$_{ctrl}$ precipitation [mm/month] and anomalies for the IPSL$_{115k}$, IPSL$_{122k}$ and IPSL$_{126k}$ run.

In Figure 3.26 the precipitation anomalies for JJAS are shown for the three Eemian time slices. The first thing to notice is the clear shift in the tropical rainbelt in connection with the Intertropical Convergence Zone (ITCZ) for all of the time slices. For the IPSL$_{115k}$ run there is a movement of the rainbelt to the south, while a progressive movement to the north can be seen for the IPSL$_{122k}$ and IPSL$_{126k}$ run. This movement corresponds to changes in the intrahemispheric temperature gradient, as the Northern Hemisphere is cooler for the IPSL$_{115k}$ run and progressively warmer for the IPSL$_{122k}$ and IPSL$_{126k}$ run (see temperature maps in Figure 3.25). An analogy can be found in the seasonal changes in the placement of the ITCZ. During summer the continental areas are heated up, strengthening the the thermal lows over the continents. This causes the ITCZ to move north during boreal summer

relative to boreal winter.
For the monsoon systems in the IPSL$_{122k}$ and IPSL$_{126k}$ run increased rain fall can be seen for East Africa and India, while a decrease in rain fall can be seen for West Africa towards the coast. The opposite response can be seen for the IPSL$_{115k}$ run. The overall response is more pronounced for Africa compared to India. These results are similar to the results of Braconnot et al. [2008], but with some differences. In the ECHAM$_{iso}$ simulations there is a dipole pattern in the monsoon response to the different Eemian climates between East and West Africa. Only hints of this pattern is seen in the Braconnot et al. [2008] results. It should also be noted that the general patterns of the tropical rain belts are different in the Braconnot et al. [2008] simulations compared to the ECHAM$_{iso}$ results. The rain belts of ECHAM$_{iso}$ are more narrow and well defined in the meridional direction. This, as well as the differences in monsoon response, can be attributed to differences in model physics.

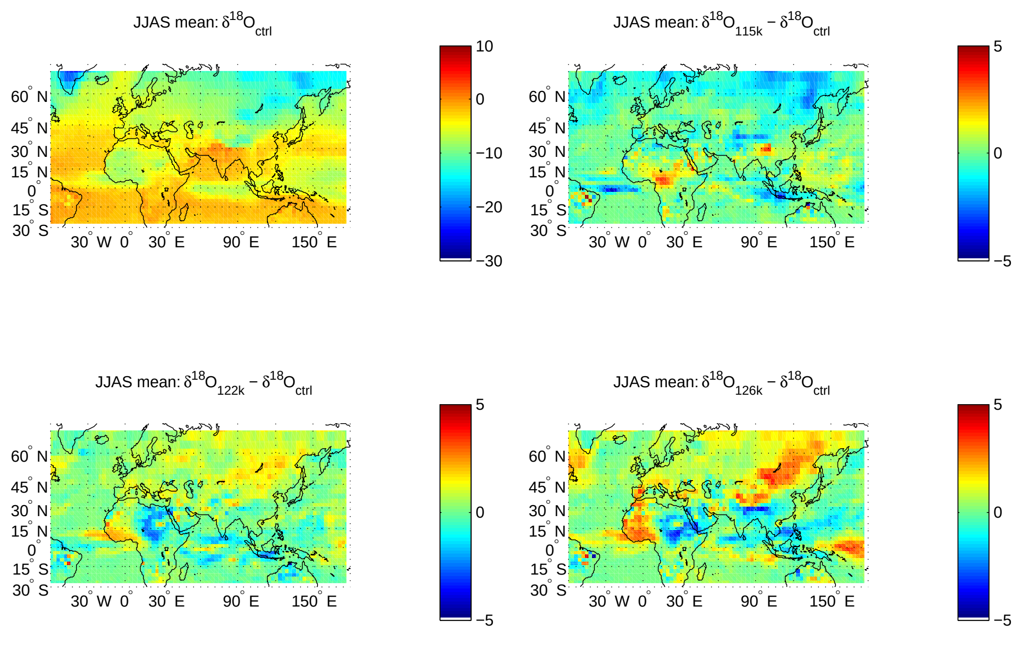

Figure 3.27: The mean JJAS IPSL$_{ctrl}$ δ^{18}O [‰] and anomalies for the IPSL$_{115k}$, IPSL$_{122k}$ and IPSL$_{126k}$ run.

The Eemian simulations done by Herold and Lohmann [2009] were done for 124kyr BP, which is in between two time slices of this study. Even though no direct comparison is then possible, the fact that Herold and Lohmann

[2009] also used the ECHAM$_{iso}$ model makes their study very relevant. The Herold and Lohmann [2009] simulation is using climatological SSTs from the ECHO-G coupled model, in which the atmospheric part is the non-isotope version of ECHAM. For their simulation this ensures a consistency between the model runs producing the SSTs patters and the model using the them. This consistency means that nonlinear effects of running a GCM with SSTs originating from a coupled model, where the atmospheric part have different biases than the GCM in question, are eliminated.

The dipole response in precipitation for the African monsoon seen here for the IPSL$_{122k}$ and IPSL$_{126k}$ run is also present and of same magnitude in the Herold and Lohmann [2009] results, which makes this response fairly robust even with the different SST forcing. Herold and Lohmann [2009] showed that the African monsoon anomalies are caused by increased eastward zonal flow in the lower troposphere and more intense convection in the 10^{o}N to 20^{o}N region of East Africa. This is again caused by a more intense thermal low over the northern part of Africa.

The δ^{18}O has significant anomalies in monsoon during the Eemian. For example are the precipitation anomalies for Africa larger than for India. Two isotopic mechanisms can be used to describe this, namely, the continental effect and the amount effect as defined by Dansgaard [1964]. For Africa there is a similar dipole in the response of δ^{18}O as for the precipitation. For East Africa there are negative anomalies of about -3‰, while West Africa has positive anomalies of 3‰ for the IPSL$_{126k}$ run. The anomalies for the IPSL$_{122k}$ run are similar but of less amplitude. For the IPSL$_{115k}$ run there are positive anomalies for East Africa of 2‰, but shifted more towards the coast. The dipole anomaly in δ^{18}O found for Africa in the IPSL$_{122k}$ and IPSL$_{126k}$ run is quite similar to the results of Herold and Lohmann [2009].

The negative δ^{18}O anomalies seen for East Africa for the IPSL$_{122k}$ and IPSL$_{126k}$ run are related to the increased eastward zonal flow and more vigorous convection mentioned above. Since the additional precipitation falling in East Africa is originating from the Atlantic it will be progressively depleted in ^{18}O as the moisture is traveling across the continent. Furthermore the increased convection in connection with more intense rainfall events will also deplete the ^{18}O. These two effects create the negative δ^{18}O anomalies.

To explain the positive δ^{18}O anomalies of West Africa it is better to turn to an analysis of the mean annual cycle. From the areas of the most pronounced Eemian precipitation anomalies, three regions were selected and the mean annual cycle calculated. The regions are West Africa (coastal), East Africa and India, and the anomalies for the Eemian time slices are shown in Figure 3.28, 3.29 and 3.30. Plots of the absolute values for the annual cycle in these regions can be seen in Appendix B.3.

In Figure 3.28 a peak the δ^{18}O anomaly can be seen during summer. This coincides with a significant negative anomaly in precipitation, and can be interpreted as a reverse amount effect, where less intense precipitation causes less depletion of the ^{18}O.

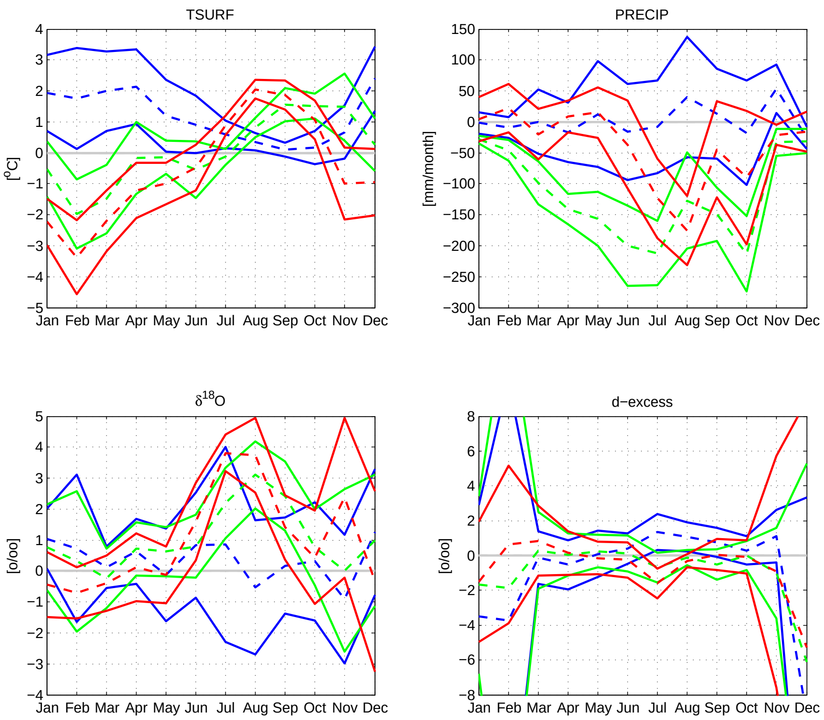

Figure 3.28: Mean annual cycle of the anomalies for surface temperature, precipitation, δ^{18}O and d-excess for the IPSL$_{115k}$ (blue), IPSL$_{122k}$ (green) and IPSL$_{126k}$ (red) run for West Africa. The area is defined as land within 0^oN to 8^oN and 20^oW to 13^oE. The dashed line is the mean value and the full lines represent ± one standard deviation for 10 years of data.

Opposed to West Africa no significant anomaly in δ^{18}O is seen for East Africa in annual cycle for the IPSL$_{122k}$ and IPSL$_{126k}$ run (see Figure 3.29). Hence, there is no signature of the a significant contribution to the negative δ^{18}O anomalies by the amount effect in connection with the positive precipitation anomalies. The conclusion from this is that the negative δ^{18}O anomalies in East Africa mainly are a result of the continental effect. Since there is no contribution of amount effect the reason for the negative JJAS anomalies is that the absolute values for δ^{18}O are most negative in July where the greatest precipitation anomaly is. The negative JJAS anomalies for East Africa is thus a consequence of precipitation weighting.

As mentioned before are the Eemian anomalies for the Indian monsoon of less magnitude compared to Africa. In July and August there is a negative anomaly in the δ^{18}O of -2‰ coinciding with the positive anomaly in precipitation (see Figure 3.30). This points to that the amount effect is causing the negative JJAS anomalies for India in the IPSL$_{122k}$ and IPSL$_{126k}$ run.

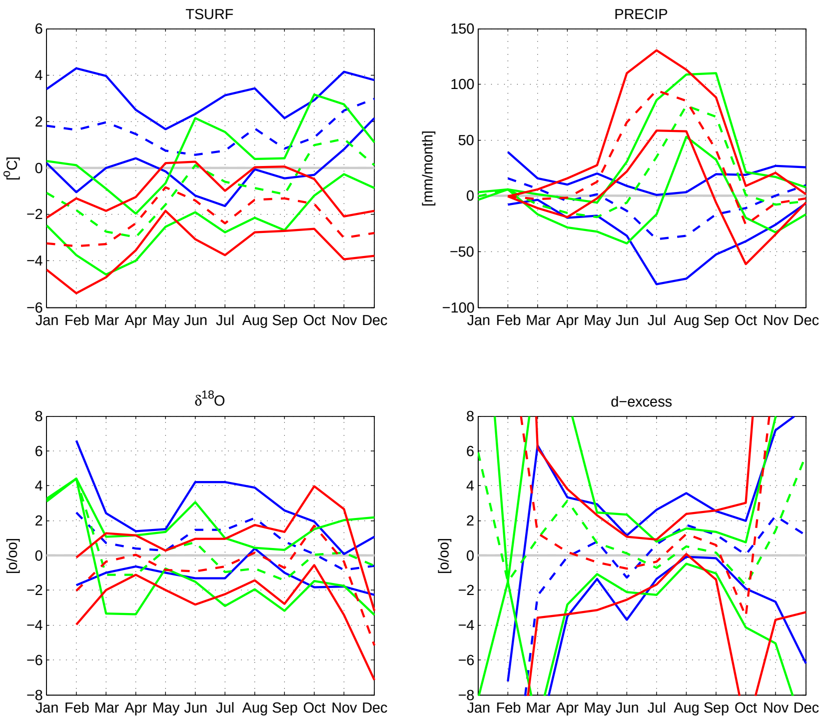

Figure 3.29: Mean annual cycle of the anomalies for surface temperature, precipitation, δ^{18}O and d-excess for the IPSL$_{115k}$ (blue), IPSL$_{122k}$ (green) and IPSL$_{126k}$ (red) run for East Africa. The area is defined as land within 8^oN to 20^oN and 0^oE to 35^oE. The dashed line is the mean value and the full lines represent $\pm$ one standard deviation for 10 years of data.

Due to the massive seasonality of precipitation in the monsoon areas the annual mean weighted δ^{18}O will be dominated by the boreal summer values. In this way shifts in δ^{18}O for the summer peak will translate into a shift in the annual mean δ^{18}O which is approximately 50% of the shift in the summer peak. The shift for the mean annual weighted δ^{18}O is +1.6‰ for West Africa, -1.6‰ for East Africa and -0.4‰ for India in the IPSL$_{126k}$ run. No significant shifts were found in the d-excess for the three monsoon regions. This is seen in Figure 3.28, 3.29 and 3.30. Also seen is the extreme variability in d-excess during boreal winter. This is due to the very low precipitation

rates in this period, which causes the d-excess signal to be very noisy as it only depends on few precipitation events.
The present scarcity of proxy for the Eemian data makes validation difficult. There are however some speleothem data from Oman, where Fleitmann et al. [2003] reports more negative δ^{18}O values for MIS 5e, which is in agreement with the findings in this study. Furthermore, Wang et al. [2008] found a strong negative correlation with the precessional cycle in the 65^{o}N insolation in a 224,000 year long speleothem δ^{18}O record from central China (110^{o}26'E, 31^{o}40'N). This is a signature of the strength of the East Asian monsoon. For the Eemian experiment with the strongest Northern Hemisphere insolation anomaly, the IPSL$_{126k}$ run, negative δ^{18}O anomalies of 2-3‰ are found for the region around 90^{o}E to 110^{o}E and 30^{o}N (see Figure 3.27). These anomalies are in good agreement with the findings of Wang et al. [2008].

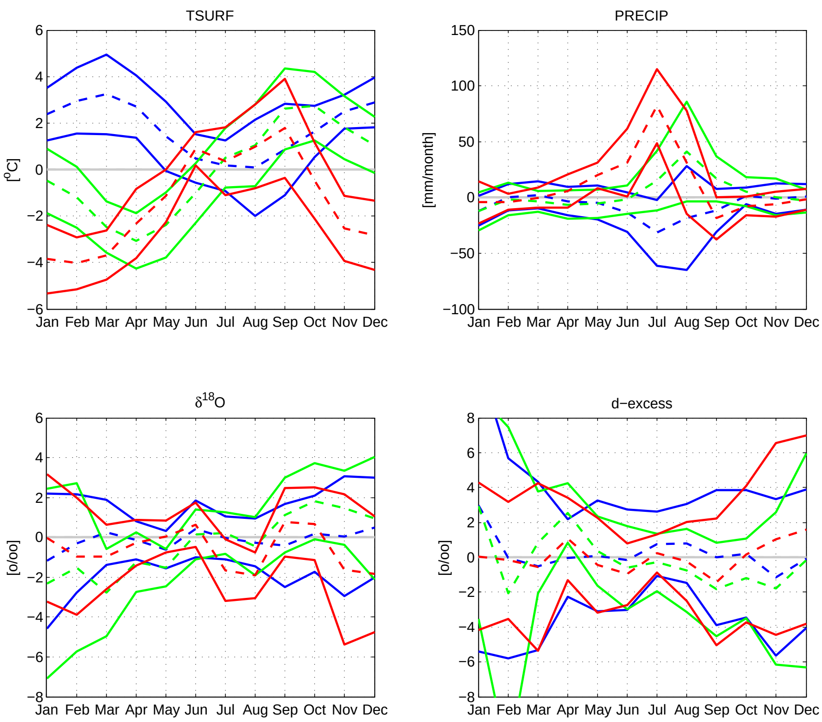

Figure 3.30: Mean annual cycle of the anomalies for surface temperature, precipitation, δ^{18}O and d-excess for the IPSL$_{115k}$ (blue), IPSL$_{122k}$ (green) and IPSL$_{126k}$ (red) run for India. The area is defined as land within 15^oN to 33^oN and 70^oE to 90^oE. The dashed line is the mean value and the full lines represent $\pm$ one standard deviation for 10 years of data.

3.5 Summary

Three Eemian time slice experiments 115kyr, 122kyr and 126kyr where performed with the ECHAM$_{iso}$ model using climatological SST fields from the IPSL_CM4 coupled model. Other than the insolation parameters and SSTs fields boundary conditions for the Eemian time slices were kept the same as for the preindustrial control run. Summer anomalies for the Northern Hemisphere were found to correspond well to proxy data for the IPSL$_{126k}$ run. The summer temperature anomalies where found to be up to $+5^{o}C$ for continental areas, with a summer peak anomaly for central Greenland of $+6^{o}C$. In response to the insolation anomalies some areas in the Northern Hemisphere showed negative winter anomalies, while areas responding to the decrease in arctic sea ice also gave positive anomalies for winter time. Due to the negative winter anomalies the annual mean temperatures for continental areas were on the order of $+1^{o}C$.
For Antarctica the temperature anomalies were found to be of smaller magnitude than for the Northern Hemisphere, and to a large extend to depend on the negative insolation anomalies for the Southern Hemisphere. However, there were some indications of the Antarctic climate following the positive temperature anomalies for the Northern Hemisphere, especially for West Antarctica.
A direct comparison with Greenland and Antarctic isotopic ice core data was carried out. In general the amplitude of the modeled isotope anomalies were underestimated. For Greenland (NorthGRIP) the modeled δ^{18}O was shown to follow the tendency for of negative anomalies for the IPSL$_{115k}$ run and positive anomalies for the IPSL$_{126k}$ run, while little isotopic response was found for the IPSL$_{122k}$ run. However, it should be underlined that the amplitude of the modeled isotope signal did not show the same magnitude as the ice core data. The modeled Antarctic isotopes (Dome C and Vostok) did not show the same agreement in tendency with the ice core data as found for Greenland. The modeled Vostok values was found to have very small anomalies for all time slices, while the modeled Dome C data showed an anomaly of similar magnitude but of opposite sign for the IPSL$_{122k}$ run compared to the ice core data.
The disagreement between ice core data and modeled isotopic values points to that significant elements of the Eemian climate was not captured in these experiments.
A study of the connection of variability between temperature, δ^{18}O and precipitation was performed on the monthly anomalies. The results for the control run was similar to that of REMO$_{iso}$ (Section 2.2.1), namely that the correlation of temperature and δ^{18}O was strongest where temperature and

precipitation also was correlated. For the Eemian experiments it was found that for the 'warm' time slices (122kyr and 126kyr), the correlation between temperature and δ^{18}O was weaker than for the 'cold' time slices (preindustrial and 115kyr). This could be seen as an analogue to the fact that during winter the temperature exerts greater control on δ^{18}O than during summer.
As a final part of the analysis of the Eemian experiments, changes in the monsoon system was studied. Significant shifts in the meridional placement of the tropical rainbelts were found for the Eemian times slices, with the rainbelts progressively moving further north with increasing summer insolation, that is, the IPSL$_{126k}$ run had the most northern placement of the rainbelts. Although the precipitation patterns and the the absolute response in monsoon for the Eemian is different in the ECHAM$_{iso}$ model compared to the IPSL_CM4, the over all effect of an intensification of the monsoon with warmer summer temperatures is seen in both models.
In terms of δ^{18}O a significant amount effect was seen for the African monsoon, which further more displayed a distinct dipole pattern in anomalies with positive anomalies in the west and negative anomalies in the east for the IPSL$_{122k}$ and IPSL$_{126k}$ run. This is in agreement with earlier Eemian monsoon studies with ECHAM$_{iso}$. Only minor changes in the δ^{18}O was found for the Indian monsoon during the Eemian, with the dominant mechanism for the δ^{18}O anomalies being the continental effect.
Isotopic monsoon model studies are relevant for interpretation of isotopic data from speleothems. The changes in modeled Eemian δ^{18}O was for example found to be in agreement with speleothem data from Oman and central China.

3.6 Discussion of the ECHAM$_{iso}$ Eemian experiments

This section elaborates further on some of the issues regarding the ECHAM$_{iso}$ Eemian experiments that have already been touched upon, such as for example the sea ice representation. Also discussed here is suggestions on how to improve the setup of the experiments to make them more realistic, and a comparison is made for the performance of IPSL_CM4 and ECHAM$_{iso}$ in the polar regions.

3.6.1 Boundary conditions and feedbacks.

As presented in Section 3.2.1 the adaption to ECHAM$_{iso}$ of sea ice from the IPSL_CM4 is less than optimal, especially for a study focusing on the polar regions. Here to ways of improving the adaptation of SSTs and sea ice are discussed.
The first suggestion is merely dealing with how to cope with the problem of transferring the information of SSTs and fractional sea ice data to a single input SST field with a sea ice threshold of -1.8^{o}C. The fractional sea ice data of the IPSL_CM4 model should be used as a mask on the SST field so that all grid points with a sea ice fraction of more than 50% is set to a temperature of -1.8^{o}C. In this way the sea ice field is not going to be as grossly underestimated as if only using the unmasked SSTs with the sea ice threshold of -1.8^{o}C.
The second way of dealing with the adaptation of the input SSTs also deals with another issue than the question of sea ice only. As the ECHAM$_{iso}$ experiments of this Eemian study are getting the input SSTs from the IPSL_CM4 model some nonlinear effects might occur because of model differences. In the coupled IPSL_CM4 experiment the oceanic part of the model receives the response of the atmospheric part of the model and vice versa, and at some point this system reaches a steady state climate. At this point the specific state of the climate depends of the interaction and biases of the combined atmosphere-ocean model. Now, when using the SSTs fields from the IPSL_CM4 model to run ECHAM$_{iso}$ the steady state climate reached by the coupled model will most certainly, because of differences in model physics, contain biases that the ECHAM$_{iso}$ would not produce if it where to be coupled with an ocean model. This could produce a nonlinear response of ECHAM$_{iso}$ to the input SSTs.
A way around this problem is to use the SST anomalies between the control run and a given time slice of the IPSL_CM4 runs and add them to a con-

trol SST field which has been validated for use with the ECHAM$_{iso}$ model. The anomalies are less likely to be affected by model biases compared to the absolute SST field.
When using the anomalies the sea ice representation must be adapted in a physical sensible way. Anomalies from the coupled model could be positive in areas where the model does not become ice free from one experiment to the other. This could cause the SST field, which should be used for the experiment, to become ice free if the temperature difference between the control SST field and the sea ice threshold is less than the anomaly from the coupled model. To prevent this from happening the rule should be made that grid boxes in the control SST field added with the anomalies only become ice free, when grid boxes in the coupled model change from being ice covered in the control experiment to being ice free in the time slice experiment.

Vegetation feedbacks.

During the Eemian the vegetation belts were most likely shifted compared to present. There is for example evidence of boreal forests extending further north in Siberia than presently [Anderson et al., 2006]. To account for this an active vegetation model component could be added in the Eemian experiments. If forests were allowed to grow further north in Siberia the albedo would decrease creating a positive feedback, which eventually could affect the Arctic sea ice giving way to even further rise in temperature. This would of cause mean that the active vegetation would have to be included in the coupled run for the vegetation feedback effect on sea ice to take place.

Eemian ice sheet configurations.

The Eemian ECHAM$_{iso}$ experiments were run with the present ice sheet configuration. This is not compatible with the geologic evidence of up 5m higher Eemian sea level than present [Anderson et al., 2006], which requires a significant reduction of the major ice sheets. Based on Greenland ice core data it is proposed by Johnsen and Vinther [2007] that the summit of the southern dome of the Greenland Ice Sheet (GIS) was reduced with about 400m. This could affect the atmospheric flow around Greenland enough to give an additional positive shift in the δ^{18}O anomaly during for the IPSL$_{122k}$ and IPSL$_{126k}$ run, and in this way explain the discrepancies found between model data and the NorthGRIP ice core data in Section 3.3.5.
A reduction of 400m of the southern dome of GIS is not enough to account for 5m of sea level rise. The main contribution for the sea level rise must then have originated from Antarctica. It is most likely that it was the West

Antarctic Ice Sheet (WAIS) that was reduced, since collapse of the major ice shelves around WAIS could destabilize the ice sheet [Oppenheimer, 1998]. Increased melting of the ice sheets would lead to an additional freshwater flux into the polar oceans. This would decrease the salinity of the surface water, which in turn would affect the deep water formation in polar areas. The deep water formation is a major driver of ocean circulation and this would change the oceanic heat transport. The additional freshwater fluxes could be included a coupled model experiment to account for the melting ice sheets.

3.6.2 Comparison of Eemian response in the polar regions between the IPSL_CM4 and the ECHAM$_{iso}$ model.

In Section 3.4 the monsoon response of the ECHAM$_{iso}$ model during the Eemian was presented. The monsoon response was found to have some differences compared to the monsoon response of the IPSL_CM4 model as presented by Braconnot et al. [2008]. Here the differences in response of temperature and precipitation are investigated for Greenland and Antarctica.
The horizontal resolution of the two models are similar, with the ECHAM$_{iso}$ being run at T42 resolution ($\sim$2.8^o) and the atmospheric part of the IPSL_CM4, the LMDz model, being run at 3.75^o longitudinal and 2.5^o latitudinal resolution. The fact that the ECHAM$_{iso}$ is a spectral model and the LMDz is a gridded model is more of technical importance than of scientific importance, as it concerns the specific way the differential equations are being integrated. The differences in model response presented in this section is more likely to be caused by the different subgrid parametrizations used by the models, the model orography and that the LMDz is a part of a coupled model, while ECHAM$_{iso}$ is being run with prescribed SSTs.
For Greenland and Antarctica some significant differences exits in orography between LMDz and ECHAM$_{iso}$. In general the LMDz is about 200m lower than ECHAM$_{iso}$ for both Greenland and Antarctica, but the differences are up to 500m in central areas of the ice sheets. Following the mean lapse rate of the atmosphere the 200m lower ice sheet should give about 1.5^oC warmer temperatures for the LMDz compared to ECHAM$_{iso}$. This should through thermodynamics in turn give higher precipitation values.
The differences in mean annual cycle between the LMDz and the ECHAM$_{iso}$ model are shown in Figure 3.31 (Greenland) and Figure 3.32 (Antarctica) for the control run and the Eemian time slices. The Greenland temperatures are

4^oC warmer during boreal winter in the LMDz model, while the difference goes close to 0^oC in July. This offset is very constant for all of the time slices. For Greenland precipitation the differences show an complementary pattern to the temperature differences. During boreal winter, for the control, 115kyr and 122kyr run, the LMDz has 5mm more precipitation a month. This difference increases to July where the difference peaks at about 15mm. The difference for the 126kyr run is almost twice that of the other runs.

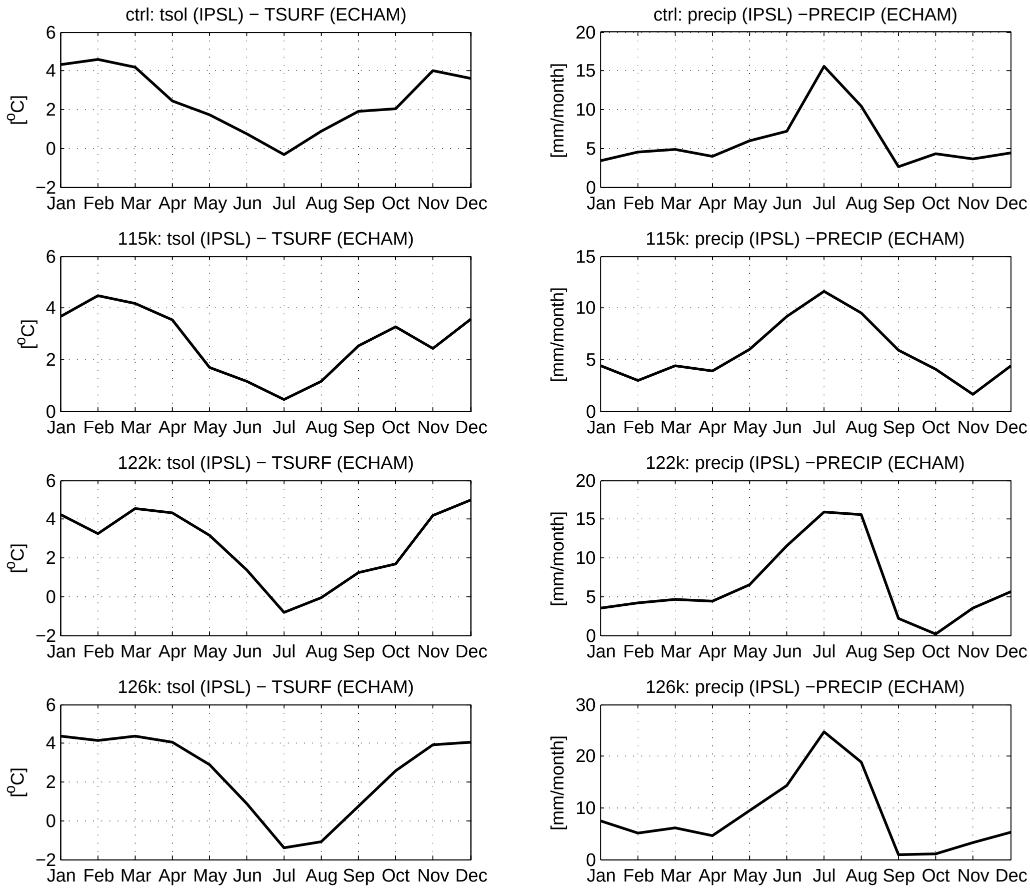

Figure 3.31: Differences in Greenland mean annual cycle between the IPSL_CM4 surface temperature (tsol) and precipitation (precip), and the ECHAM$_{iso}$ surface temperature (TSURF) and precipitation (PRECIP) for the preindustrial control, 115kyr, 122kyr and 126kyr time slice.

The same type of differences in temperature is seen for Antarctica as for Greenland only the offset during austral winter is 9^oC, and the difference diminishes to about 5^oC in February. The pattern for the temperature differences for Antarctica is not as constant as for Greenland, but the overall off set is still the same. For the precipitation the differences for Antarctica looks to be tied to temperature differently than for Greenland. As opposed to Greenland the differences in precipitation seem to follow the temperature differences, if not one-to-one, then at least in phase.

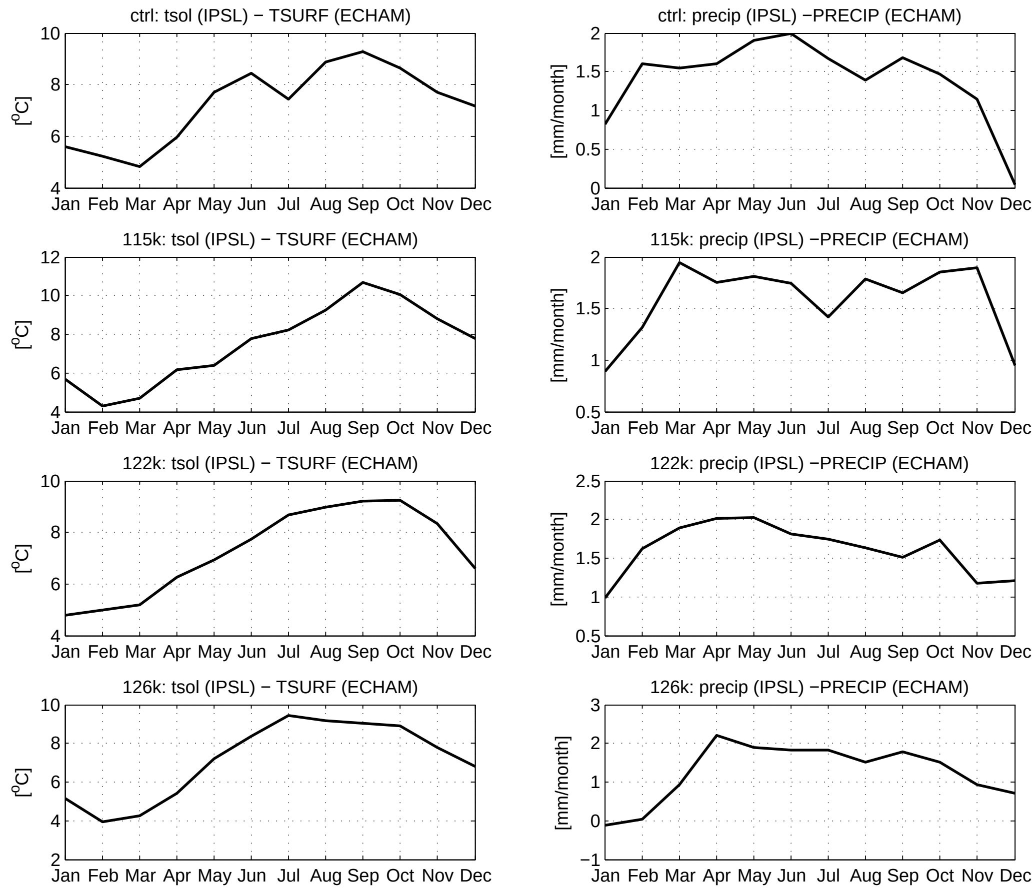

Figure 3.32: Same as Figure 3.31, but for East Antarctica.

The differences in the annual cycle of precipitation in relation to the differences in annual cycle of temperature speaks of a difference in the link between precipitation and temperature in the two models. This can be illustrated by looking at the correlation between changes in temperature and changes in precipitation in the two models for all the Eemian time slices. From Table 3.2 it is clear that changes in temperature is strongly dictating changes in precipitation in the LMDz model, while a connection is only seen for the ECHAM_{iso} model in the 115kyr time slice. An explanation could be that a more simple thermodynamic mechanism is predominant in the LMDz model compared to ECHAM$_{iso}$.

Time Slice	IPSL	ECHAM
	R^2 GRN/ANT	R^2 GRN/ANT
115kyr	0.54/0.34	0.32/0.46
122kyr	0.46/0.41	0.04/0.09
126kyr	0.85/0.28	0.03/0.05

Table 3.2: The square of the linear correlation, R^2, between mean monthly anomalies in precipitation and anomalies in surface temperature for the IPSL_CM4 and the ECHAM$_{iso}$ model for Greenland (GRN) and Antarctica (ANT). Only R^2 values above 0.4 are significant as the calculation is based on a set of 12 monthly mean values.

The Eemian experiment

Chapter 4

Outlook and conclusions

4.1 Conclusions

This thesis consists of two main parts presenting the bulk work of this PhD project: a present day experiment for Greenland using the regional model REMO_{iso}, and a palaeoexperiment for the Eemian interglacial using the global model ECHAM_{iso}.

The REMO_{iso} experiment

The REMO_{iso} experiment for Greenland was carried out using a nudging technique in order to reproduce the actual weather patterns for the period 1959 to 2001. This nudging procedure proved to be successful in capturing the observed seasonal variability for temperature, precipitation and the NAO. A temperature bias of about $+5^oC$ was found for central Greenland. This is thought to be caused by a too low albedo for fresh snow, and the parametrization of the boundary layer.
A positive bias for central Greenland was also found in δ^{18}O. As the spatial slope for temperature versus δ^{18}O is underestimated by REMO_{iso}, the δ^{18}O bias was concluded not only to be caused by temperature, but also by moisture transport. This explanation is in agreement with the dry bias which also was found for inland Greenland, probably caused by a underestimated moisture transport to cold regions. Temporally REMO_{iso} captures the winter variability well for the GRIP and Site G ice core sites, as well as for observations from Reykjavik and Ny Ålesund, while less agreement between model and observations is found for DYE3 and Danmarkshavn. A strong imprint of the NAO was found for the main variability pattern of δ^{18}O. However, as also found for the δ^{18}O of ice cores, this correlation is not constant in time,

since some periods of decoupling between the NAO and δ^{18}O is seen.
The annual cycle and mean levels of d-excess for coastal cites is well reproduced by the model, especially for Reykjavik where the winter variability also is in good agreement with observations (R^2=0.50). For inland Greenland a bias in d-excess is found when the δ^{18}O is below $\sim$ -30‰. This is most likely caused by the tuning of the supersaturation parametrization, and a solution is thought to be at hand by revising this tuning.
In this study the performance and biases of REMO$_{iso}$ have been mapped specifically for Greenland, and insights have been gained regarding the temporal and spatial variability of temperature, δ^{18}O and precipitation.

The Eemian experiment

For the Eemian interglacial three time slice experiments (115kyr, 122kyr and 126kyr) were carried out with ECHAM$_{iso}$, using climatological SSTs from a coupled model. All other parameters except insolation and SSTs were kept constant. For the 126kyr experiment, which presumably represents the time around the Eemian climatic optimum, the modeled Northern Hemisphere summer temperatures are in good agreement with proxy data collected from many regions. However, the mean annual temperature response for Greenland is limited. For Antarctica the temperature anomalies are marginal compared to temperature anomalies inferred by proxy data, even with significant negative Southern Hemisphere sea ice anomalies.
Compared to ice core data the modeled δ^{18}O for Greenland follows the trend of lower δ^{18}O values for 115kyr and higher δ^{18}O values for 126kyr, but with a underestimated amplitude. The modeled δ^{18}O response for a $+6^oC$ peak summer anomaly gives a δ^{18}O anomaly of +2‰, in agreement with a modeled temperature-δ^{18}O temporal slope for summer of $\sim$0.3‰$/^oC$. This suggests that the Greenland temperature for the Eemian was even even higher than depicted by the model output, as the NorthGRIP ice core show mean annual δ^{18}O values 3‰ higher than present. This discrepancy could possibly be corrected with a reduced Greenland ice sheet.
As expected from the Antarctic temperature anomalies the modeled δD anomalies do not agree with ice core data. This could for example be caused by an oceanic coupling between the Northern and Southern Hemisphere climate not being simulated by the coupled model producing the SST climatology, or because of additional melt from the Greenland and Antarctic ice not being included.
The modeled precipitation anomalies for Greenland and Antarctica are generally minor. However for the 126kyr time slice there is a tendency of less winter/spring precipitation and more summer/autumn precipitation. This is

a nonlinear response in precipitation in relation to the temperature anomalies.
For the Eemian monsoon response a strong connection between precipitation amount and the Northern Hemisphere summer temperature is seen. This is in agreement with previous model studies. Also in agreement with a previous model study, also using ECHAM$_{iso}$ but with different SSTs, is the dipole δ^{18}O anomaly seen for west-east Africa, with a clear signature of the isotopic amount effect.
With these experiments the effects of the changes in the orbital parameters during the Eemian have been investigated. Solely changing the orbital parameters does not give a result in agreement with isotope records from Greenland and Antarctica. The conclusion is that ice sheet dynamics, changing the geometry of the ice sheets and affecting the ocean circulation, must be included to gain a higher level of realism.

4.2 Future work

After the analysis of the REMO$_{iso}$ output on time scales down to monthly resolution, many questions are unanswered regarding the processes that take place on the time scale of individual precipitation events. Such an analysis has been initiated, but remains to be carried out in full scale.
The supersaturation parametrization was a recurring subject with respect to the analysis of the d-excess simulation for inland Greenland. A sensitivity study for the supersaturation parametrization with REMO$_{iso}$ is likely to be an important step towards a better simulation of the d-excess annual cycle and mean values for cold regions.
Since the implementation of the isotopes in REMO version 5.0 (2002) has REMO been updated in 2008. The updates include parametrizations for sea ice, land-surface schemes, cloud-microphysics and high latitude convection schemes (Hagemann et al. [2009] and *C. Sturm*, personal communication). Furthermore is it possible to run the new version of REMO using parallel processing, which significantly decreases computing time. These updates are most relevant for isotopic studies and an update of REMO$_{iso}$ is a logical next step. At the same time would a review of the surface albedo parameters be relevant in connection with resolving the temperature bias over Greenland.
The performance of REMO$_{iso}$ for present day Greenland climate has now been evaluated, which means that it can be considered using REMO$_{iso}$ for palaeostudies. Taking advantage of the high resolution of REMO$_{iso}$ would be obvious when studying the effect of changes of the ice sheet geometry during past climates. This would be relevant both for the Holocene, Eemian and

LGM.
Regarding the Eemian experiments many of the suggested improvements in Section 3.6 to increase the level of realism involve interactive dynamics that would demand redoing the coupled model runs. This includes the added melt water from ice sheets, and the online calculation of vegetation feedbacks. Although doing an offline experiment with a vegetation model would probably also be useful even though this would exclude the albedo feedback on the fully coupled model.
A sensitivity study of the Greenland isotopic composition with respect to the height of the southern dome of the GIS, could also be performed. Even with the courser resolution of the global model compared to REMO$_{iso}$, this could serve as a preliminary study on the effect of the shape of the ice sheet.
The analysis of the 10 years of model output from ECHAM$_{iso}$ showed a very noisy signal in the δ^{18}O and even more so in the d-excess. This was especially the case for inland Antarctica. An extension of the model runs with 10-20 years would improve the signal to noisy ratio. However, before extending the existing runs one might consider to replace the original runs and improve the adaptation of the SST fields from the coupled model, as described in Section 3.6.

Appendix A

A.1 Monthly temperature, δ^{18}O and precipitation from Reykjavik

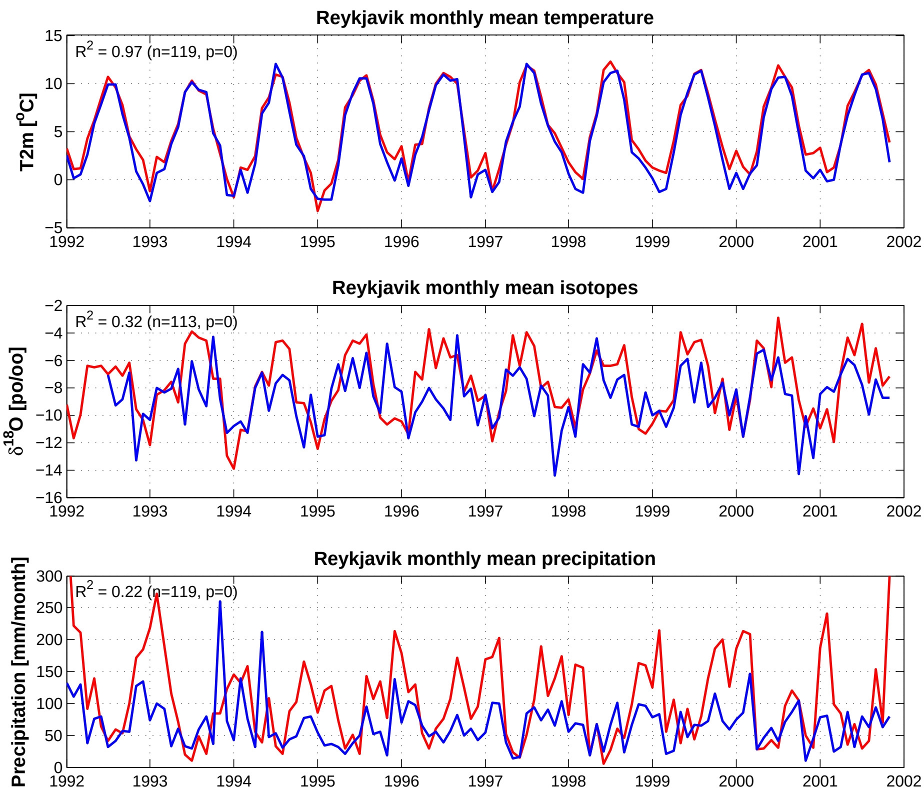

Figure A.1: Modeled (red) and observed (blue) monthly mean temperature, δ^{18}O and precipitation for Reykjavik.

A.2 Principal Component Analysis

A Principal Component Analysis (PCA) is a coordinate transformation done to find the modes of maximum variability for a given vector. The vector can be whatever set of observed or modeled data of interest. While a short overview is given here, the method is described in details by Storch and Navarra [1995]. The method of PCA is also referred to as Empirical Orthogonal Functions (EOFs).
The procedure starts with finding the covariance matrix of the data vector, and then proceeding to find the eigenvectors of this covariance matrix. The eigenvectors will represent the modes of variability of the data vector, with the largest eigenvector giving the primary mode of variability. As the eigenvectors are orthogonal the different modes of variability (principal components) will be independent of each other.
It is common practice to use the term EOFs about the loadings on the principal components, while the term principal components is used to refer to the temporal development of the principal components. The EOFs can often represent spatial patterns of variability, depending on the nature of the original data vector.

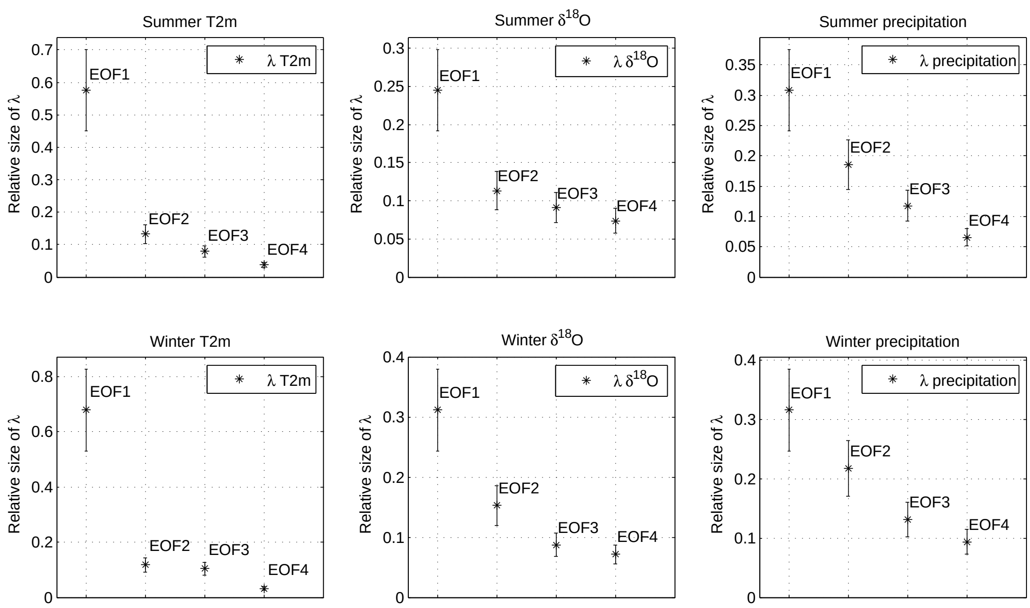

Figure A.2: The size and estimated uncertainty of the first four eigenvalues for the PCA of seasonal temperature, δ^{18}O and precipitation (see Section 2.1.5).

It was mentioned above that the principal components represent unique modes of variability. However, this is only the case if the eigenvectors are properly separated. Sometimes the eignevalues will be of very similar size, and thus possibly having degenerated eigenvectors, that is, the principal components will represent a mixed variability state. North et al. [1982] suggested a method to estimate the uncertainty of the eigenvalues, based on the number of degrees of freedom in the data vector. This is shown in Figure A.2, where the relative size of the eigenvalues are displayed along with the uncertainties for the PCA presented in Section 2.1.5. If the size of an eigenvalue overlaps with the uncertainty of a neighboring eigenvalue, then the eigenvectors are possibly *effectively degenerated* and should be left out of further analysis. An example of possibly effectively degenerated eigenvectors is the EOF1 and EOF2 of winter temperature.

A.3 The bootstrap method

The bootstrap method was introduced by Efron [1983] as a way of empirically calculating the statistical distribution function for a given data set. In this way one can avoid making any assumptions about the statistical properties of the data set, since they are calculated based on the data set itself.
The method involves resampling *with replacement*, where the property in question, be it mean, standard deviation or correlation coefficient, is calculated for each resampled set. By resampling, say 1000 times, the result will be an empirical distribution function based on the original data.
In Figure 2.11 the bootstrap method is used in connection with the calculation of a running correlation. The window of the correlation only has 11 data points, which makes it difficult to estimate the significance of the correlation. With the bootstrap method this can be calculated.

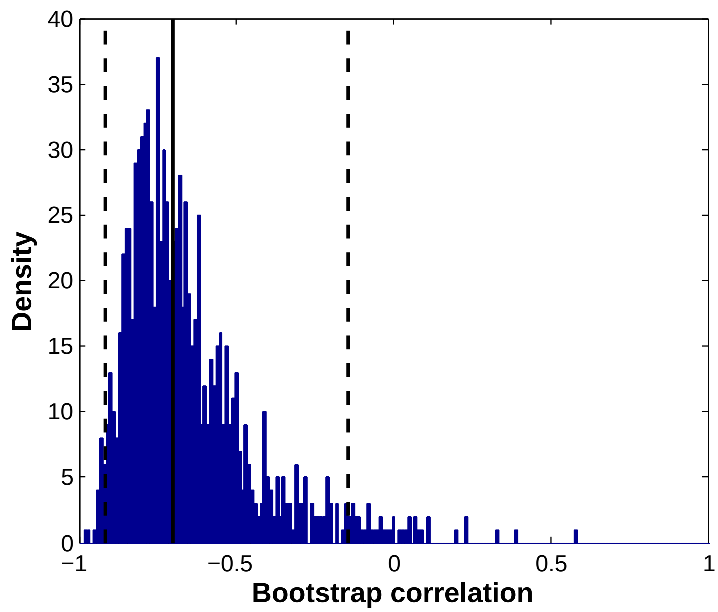

Figure A.3: Example of a correlation calculated by bootstrapping. The histogram shows the density function for the bootstrap correlation. The 95% confidence interval is shown with the dashed lines, and the full line is the correlation calculated via the density function. The data is from one of the 11 year windows for the running correlation between the PC1 of winter temperature and NAO shown in Figure 2.11.

Imagine a die with 11 sides. Each side has a pair of numbers, one from each data set we wish to calculate the correlation for. The die is then thrown

11 times, which is the same as resampling with replacement. Then the correlation for the resampled set is calculated. The resampling and correlation calculation is then repeated 1000 times, and the resulting histogram of correlations is an empirical distribution function for the correlation (see Figure A.3). By the shape of the histogram the correlation coefficient and significance of the correlation can be estimated.

A.4 The connection between temperature and precipitation

This is a simple example of how the correlation between temperature and precipitation can be linked to the variance of the temperature. The assumption is that the precipitation anomalies P are proportional to temperature anomalies T, and that there is some noise in the system η, which is independent of T. This can be described in the following equation, where α is a constant

$$P = \alpha T + \eta \tag{A.1}$$

The correlation coefficient R between T and P can be written as

$$R_{T,P} = \frac{cov_{T,P}}{\sigma_T \sigma_P} \tag{A.2}$$

or written in terms of the expected value E, where $E(TP) = cov_{T,P}$, $E(T^2) = (\sigma_T)^2$ and $E(P^2) = (\sigma_P)^2$

$$R_{T,P} = \frac{E(TP)}{\sqrt{E(T^2)E(P^2)}} \tag{A.3}$$

Inserting P using Equation A.1 gives

$$R_{T,P} = \frac{E(T(\alpha T + \eta))}{\sqrt{E(T^2)E((\alpha T + \eta)^2)}} \tag{A.4}$$

Expanding the parenthesis and using that E is a linear operator yields

$$R_{T,P} = \frac{E(\alpha T^2 + \eta T)}{\sqrt{E(T^2)E(\alpha^2 T^2 + \eta^2 + 2\alpha\eta T)}} = \frac{\alpha E(T^2) + E(\eta T)}{\sqrt{E(T^2)(\alpha^2 E(T^2) + E(\eta^2) + 2\alpha E(\eta T))}} \tag{A.5}$$

Since η is independent of T the covariance of η and T, $E(\eta T)$, will be zero. This leaves

$$R_{T,P} = \frac{\alpha E(T^2))}{\sqrt{E(T^2)(\alpha^2 E(T^2) + E(\eta^2))}} \tag{A.6}$$

After a few more manipulations the final expression becomes

$$R_{T,P} = \frac{1}{\sqrt{1 + \frac{1}{\alpha^2}\frac{E(\eta^2)}{E(T^2)}}} \tag{A.7}$$

Basically the correlation will depend on the ratio between the noise level and the temperature signal. In the limit of $T \rightarrow \infty$ $R_{T,P}$ will become 1.

A.5 The effect of changing S_i in a Rayleigh-type model including kinetic effects.

Here the effect of changing the supersaturation parametrization during snow formation in a Rayleigh-type model including kinetic effects is explored. As pointed out by Jouzel and Merlivat [1984] increasing the supersaturation will give a δ^{18}O - δD slope closer to the slope of 8 as for the Global Meteoric Water Line.

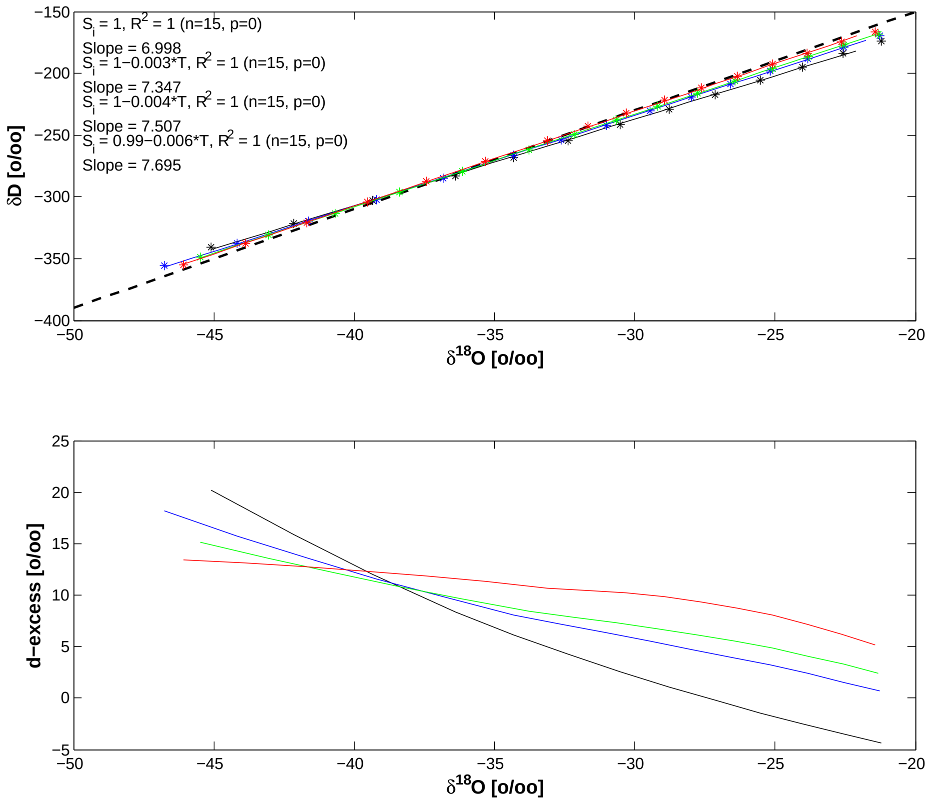

Figure A.4: Results of running a Rayleigh-type model including kinetic effects with different supersaturation parametrizations. The top panel shows the δ^{18}O - δD slope for the different supersaturation parametrizations compared to the Global Meteoric Water Line (dashed). The different supersaturation parametrizations used are $S_i = 1$ (black), $S_i =$ 1-0.003*T (blue), $S_i =$ 1-0.004*T (green) and $S_i =$ 0.99-0.006*T (red). The bottom panel shows the d-excess plotted against the δ^{18}O for the same model data and displayed using same color coding. A moisture source with a relative humidity of 0.8 and a temperature of 20^oC was used for all model runs.

This can also be seen in the top panel of Figure A.4. The since there is a difference in slope for the different supersaturation parametrizations the d-excess will also be different. The relation between the supersaturation and the d-excess is not as simple, as for example saying that higher supersaturation gives higher d-excess. This can be seen in the lower panel of Figure A.4, higher supersaturation (red curve) will yield a flatter curve of d-excess in relation to δ^{18}O compared to a lower supersaturation (blue curve) or no supersaturation (black curve).

Appendix B

B.1 Eemian temperature, precipitation, and isotopes for Greenland.

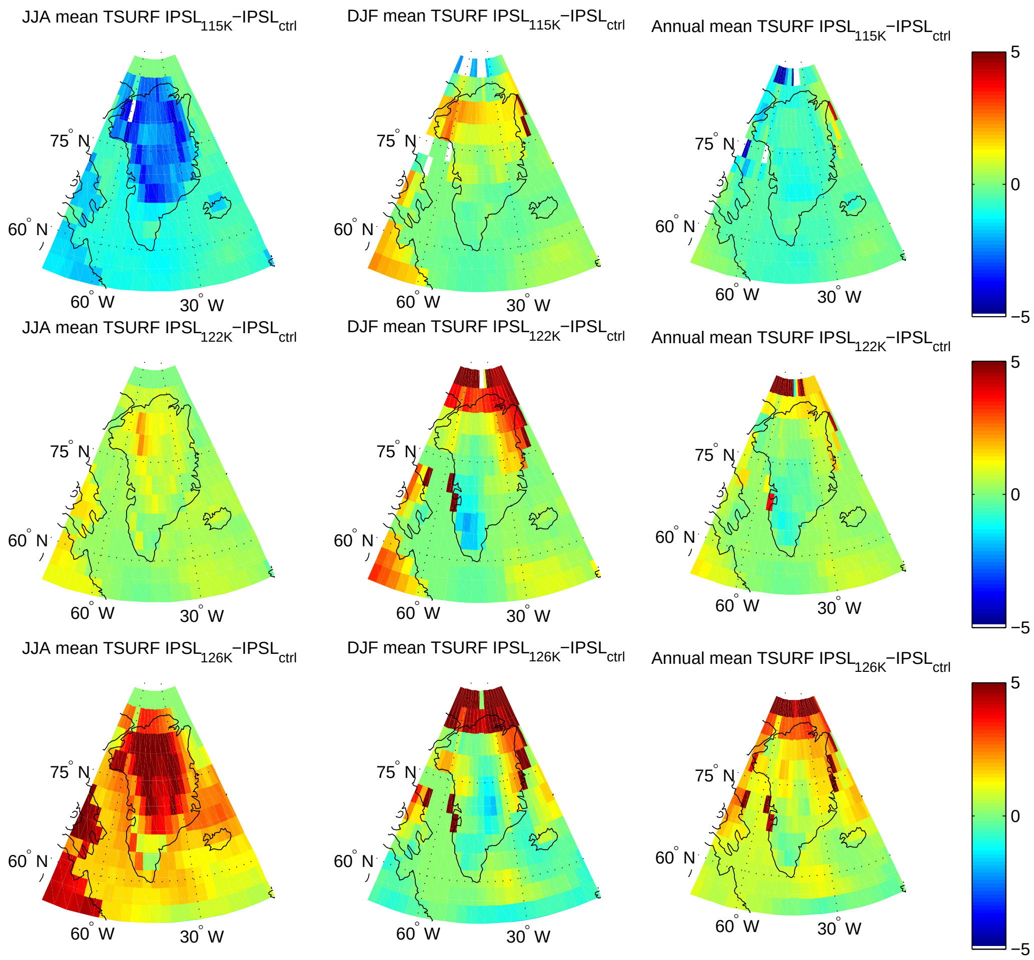

Figure B.1: ECHAM$_{iso}$ mean surface temperature anomaly [^oC] for June, July and August (JJA), December, January and February (DJF) and annual mean anomaly for Greenland for time slices 115kyr (top), 122kyr (middle) and 126kyr (bottom).

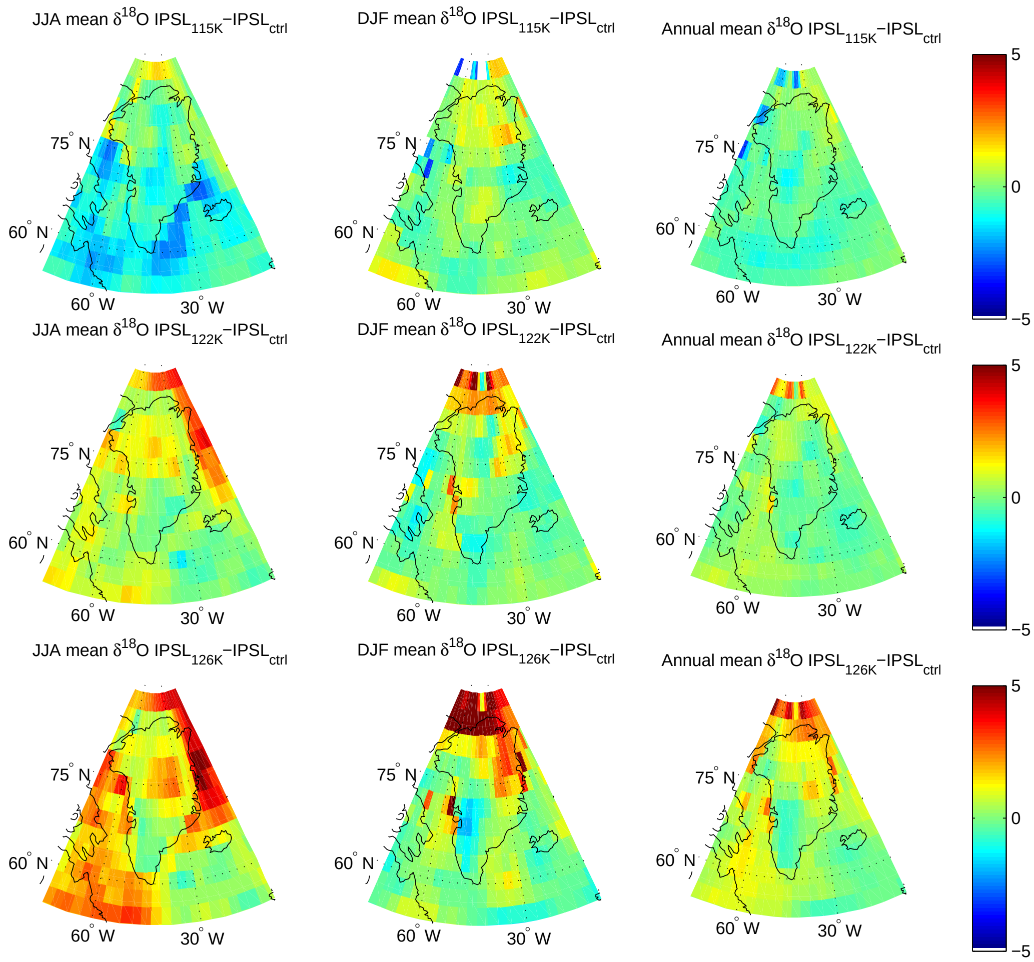

Figure B.2: ECHAM$_{iso}$ mean precipitation weighted δ^{18}O anomaly [o/oo] for June, July and August (JJA), December, January and February (DJF) and annual mean anomaly for Greenland for time slices 115kyr (top), 122kyr (middle) and 126kyr (bottom).

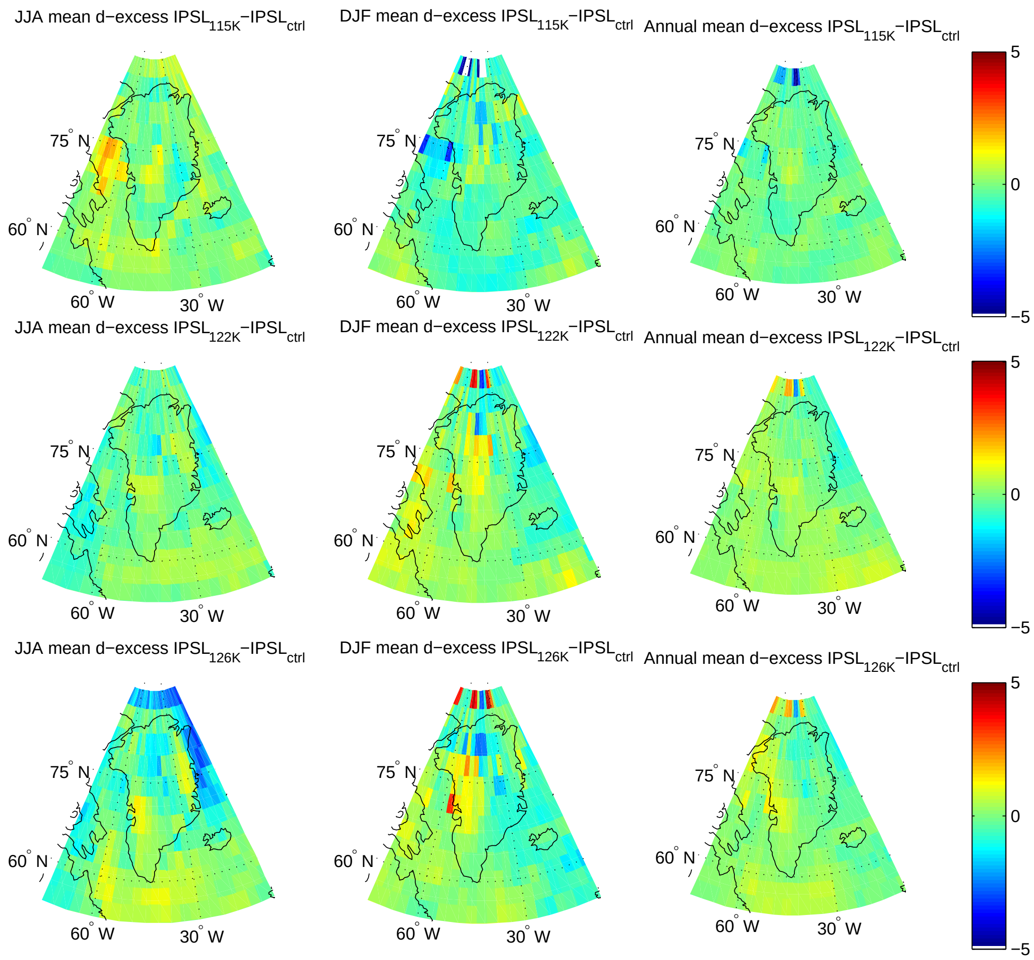

Figure B.3: ECHAM$_{iso}$ mean precipitation weighted d-excess anomaly [o/oo] for June, July and August (JJA), December, January and February (DJF) and annual mean anomaly for Greenland for time slices 115kyr (top), 122kyr (middle) and 126kyr (bottom).

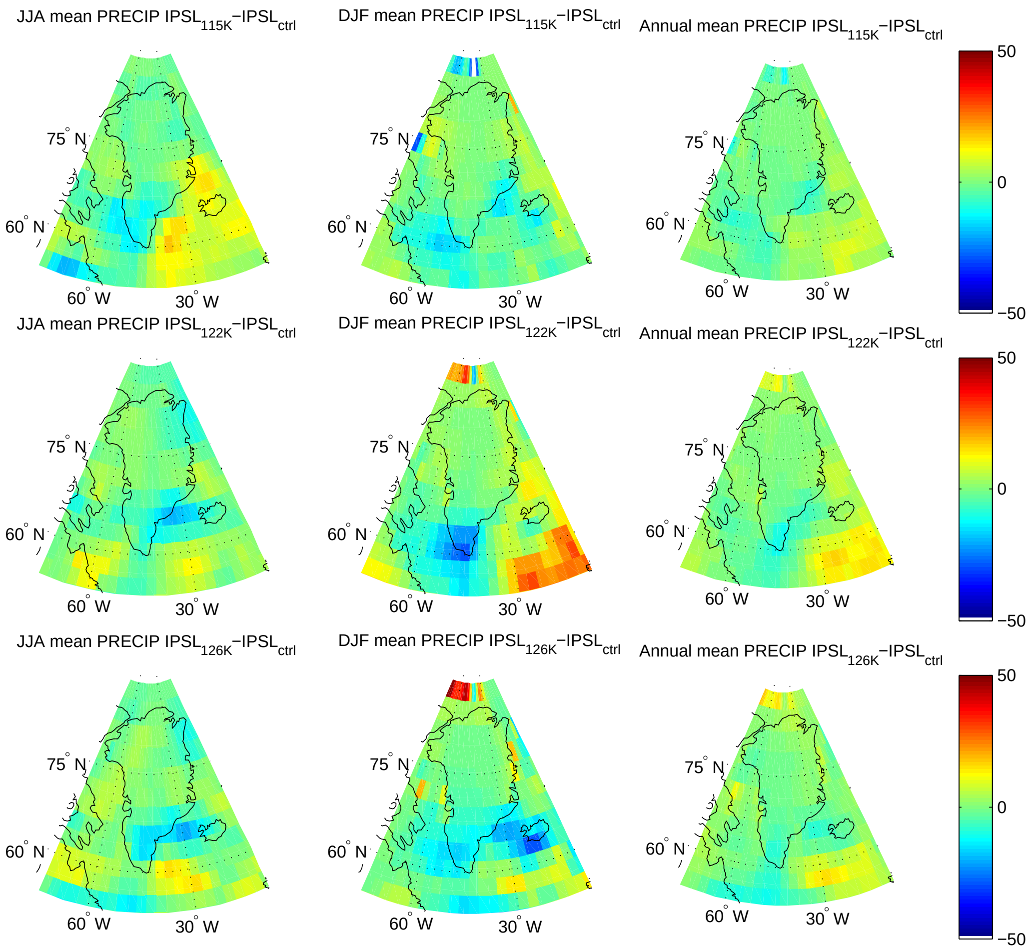

Figure B.4: ECHAM$_{iso}$ precipitation anomaly $[mm/month]$ for June, July and August (JJA), December, January and February (DJF) and annual mean anomaly for Greenland for time slices 115kyr (top), 122kyr (middle) and 126kyr (bottom).

B.2 Correlation maps of temperature, precipitation and δ^{18}O.

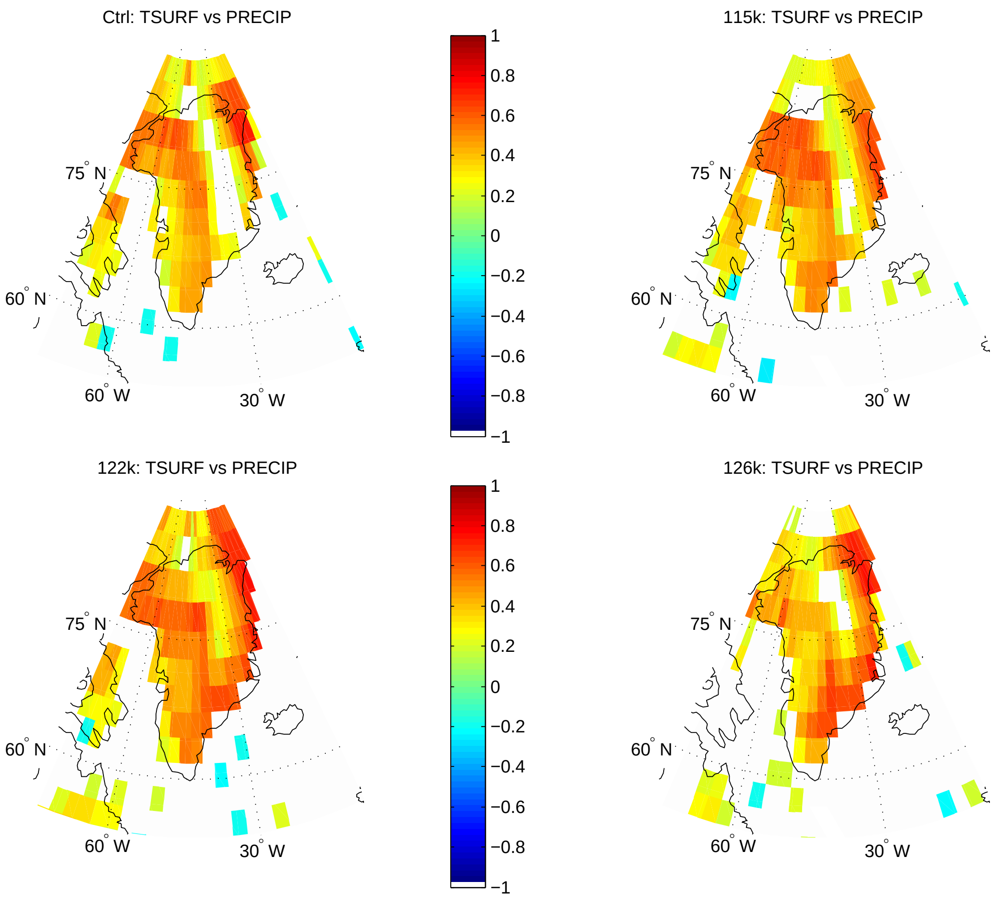

Figure B.5: The linear correlation between monthly anomalies of surface temperature and precipitation for the IPSL$_{ctrl}$, IPSL$_{115k}$, IPSL$_{122k}$ and IPSL$_{126k}$ run zoomed on Greenland. The correlation map is done by subtracting the mean annual cycle from the monthly data series for each grid point and then calculating the correlation. Data points with non-significant correlation coefficients ($p > 0.05$) have been masked out.

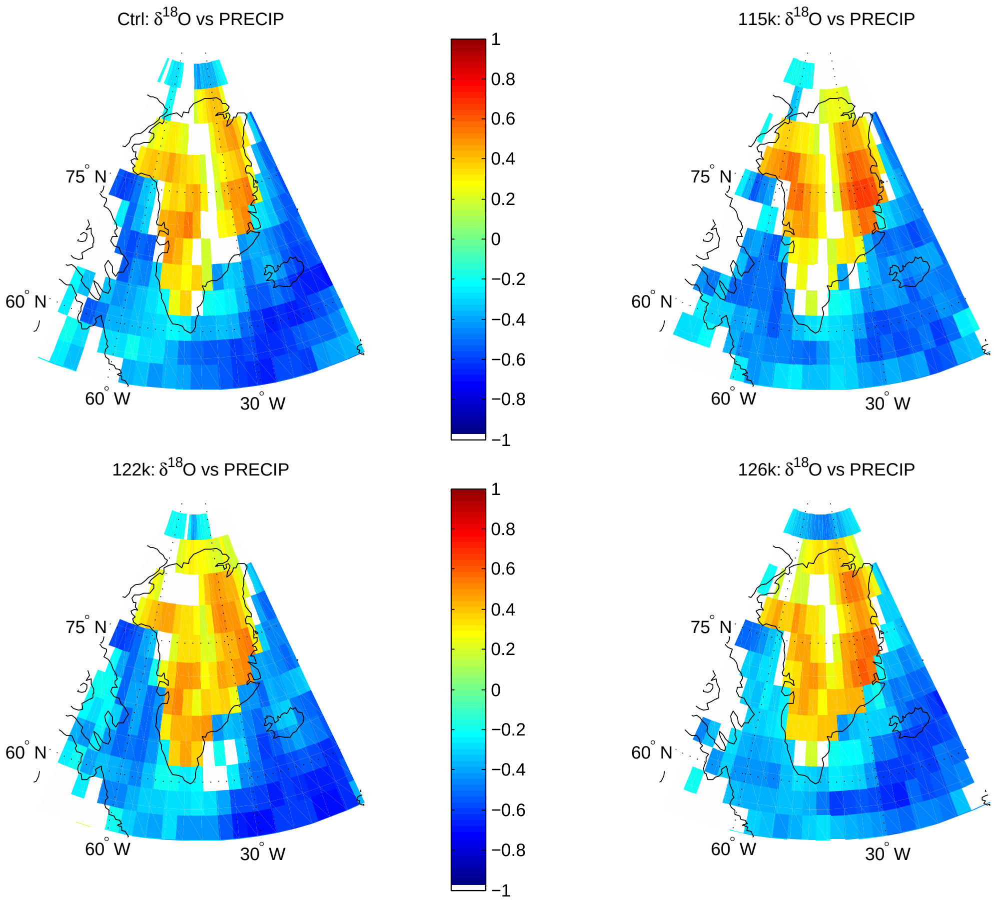

Figure B.6: The linear correlation between monthly anomalies of δ^{18}O and precipitation for the IPSL$_{ctrl}$, IPSL$_{115k}$, IPSL$_{122k}$ and IPSL$_{126k}$ run zoomed on Greenland. The correlation map is done by subtracting the mean annual cycle from the monthly data series for each grid point and then calculating the correlation. Data points with non-significant correlation coefficients (p $>$ 0.05) have been masked out.

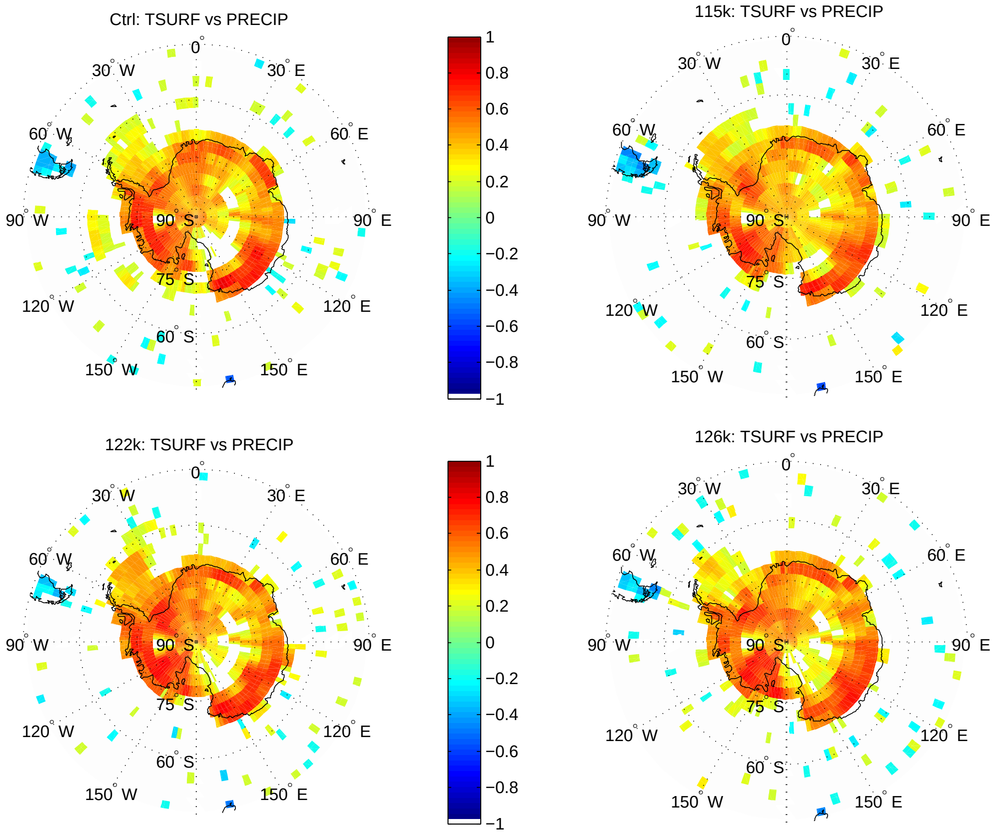

Figure B.7: The linear correlation between monthly anomalies of surface temperature and precipitation for the IPSL$_{ctrl}$, IPSL$_{115k}$, IPSL$_{122k}$ and IPSL$_{126k}$ run focused on Antarctica. The correlation map is done by subtracting the mean annual cycle from the monthly data series for each grid point and then calculating the correlation. Data points with non-significant correlation coefficients ($p > 0.05$) have been masked out.

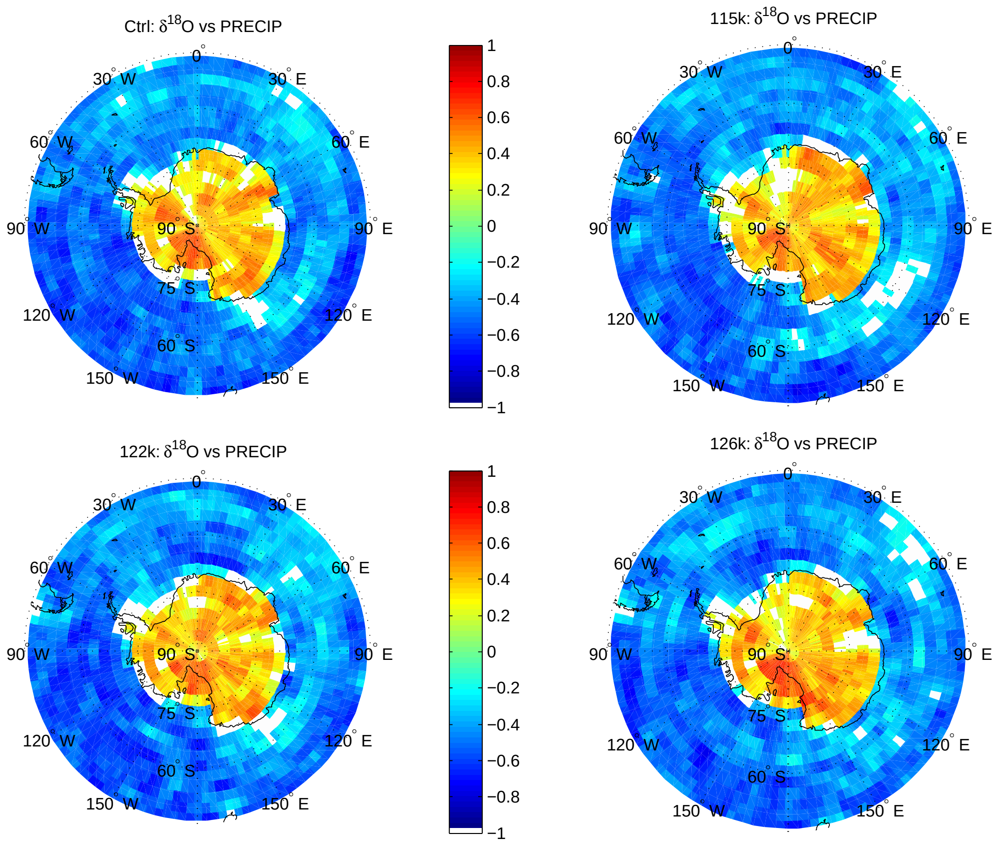

Figure B.8: The linear correlation between monthly anomalies of δ^{18}O and precipitation for the IPSL$_{ctrl}$, IPSL$_{115k}$, IPSL$_{122k}$ and IPSL$_{126k}$ run focused on Antarctica. The correlation map is done by subtracting the mean annual cycle from the monthly data series for each grid point and then calculating the correlation. Data points with non-significant correlation coefficients ($p > 0.05$) have been masked out.

B.3 The African and Indian Monsoon system during the Eemian

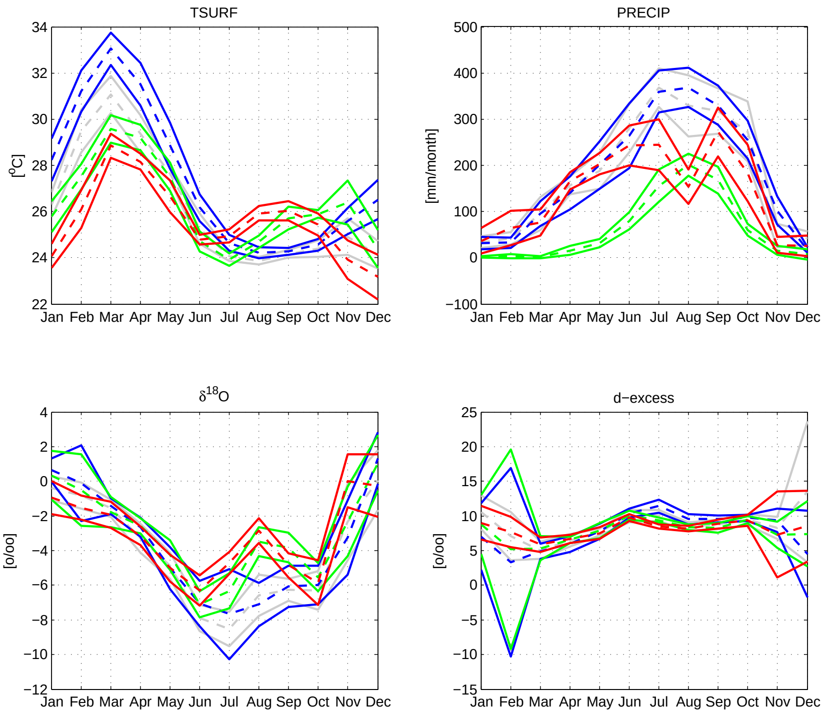

Figure B.9: Mean annual cycle of surface temperature, precipitation, δ^{18}O and d-excess for the IPSL$_{ctrl}$ (gray), IPSL$_{115k}$ (blue), IPSL$_{122k}$ (green) and IPSL$_{126k}$ (red) run for West Africa. The area is defined as land within 0^oN to 8^oN and 20^oW to 13^oE. The dashed line is the mean value and the full lines represent $\pm$ one standard deviation for 10 years of data.

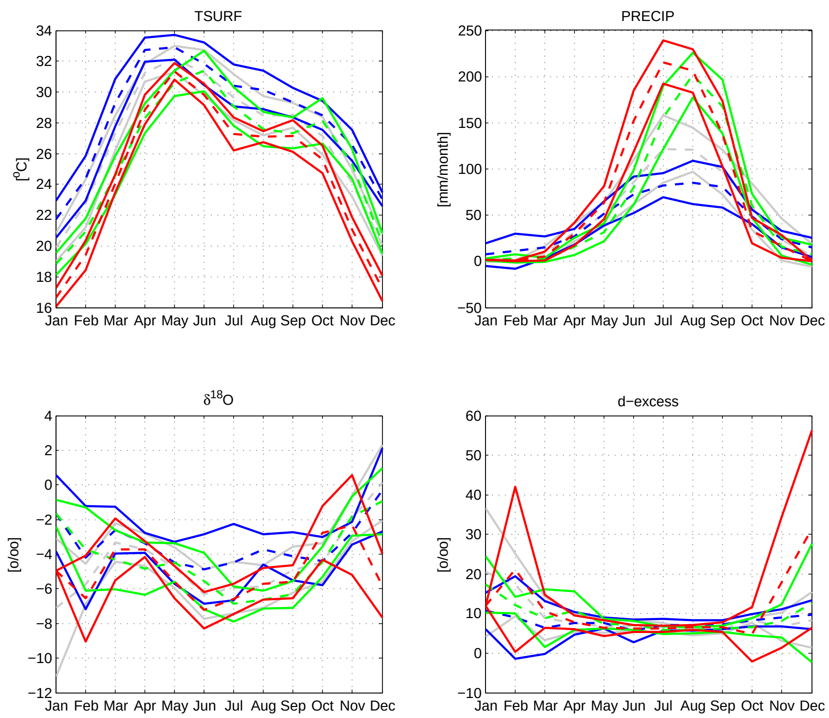

Figure B.10: Mean annual cycle of surface temperature, precipitation, $\delta^{18}O$ and d-excess for the $IPSL_{ctrl}$ (gray), $IPSL_{115k}$ (blue), $IPSL_{122k}$ (green) and $IPSL_{126k}$ (red) run for East Africa. The area is defined as land within 8^oN to 20^oN and 0^oE to 35^oE. The dashed line is the mean value and the full lines represent ± one standard deviation for 10 years of data.

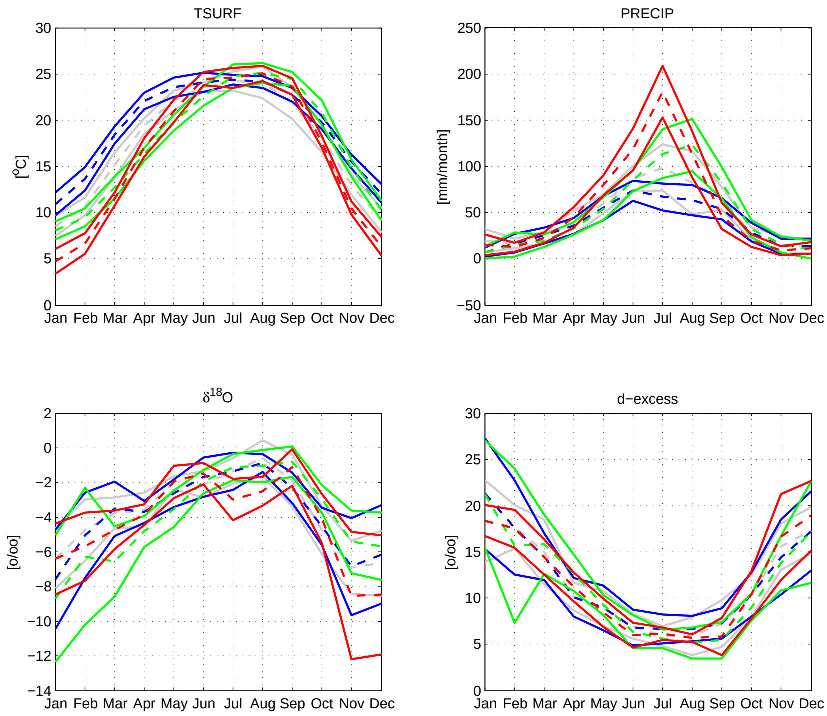

Figure B.11: Mean annual cycle of surface temperature, precipitation, δ^{18}O and d-excess for the IPSL$_{ctrl}$ (gray), IPSL$_{115k}$ (blue), IPSL$_{122k}$ (green) and IPSL$_{126k}$ (red) run for India. The area is defined as land within 15^oN to 33^oN and 70^oE to 90^oE. The dashed line is the mean value and the full lines represent $\pm$ one standard deviation for 10 years of data.

Bibliography

KK Andersen, N Azuma, JM Barnola, M Bigler, P Biscaye, N Caillon, J Chappellaz, HB Clausen, D DahlJensen, H Fischer, J Fluckiger, D Fritzsche, Y Fujii, K Goto-Azuma, K Gronvold, NS Gundestrup, M Hansson, C Huber, CS Hvidberg, SJ Johnsen, U Jonsell, J Jouzel, S Kipfstuhl, A Landais, M Leuenberger, R Lorrain, V Masson-Delmotte, H Miller, H Motoyama, H Narita, T Popp, SO Rasmussen, D Raynaud, R Rothlisberger, U Ruth, D Samyn, J Schwander, H Shoji, ML Siggard-Andersen, JP Steffensen, T Stocker, AE Sveinbjornsdottir, A Svensson, M Takata, JL Tison, T Thorsteinsson, O Watanabe, F Wilhelms, JWC White, and N Greenland Ice Core Project. High-resolution record of Northern Hemisphere climate extending into the last interglacial period. *NATURE*, 431(7005):147–151, SEP 9 2004. ISSN 0028-0836. doi: 10.1038/nature02805.

Pat Anderson, Ole Bermike, Nancy Bigelow, Julie Brigham-Grette, Matt Duvall, Mary Edwards, Bianca Frechette, Svend Funder, Sigfus Johnsen, Jochen Knies, Roy Koerner, Anatoly Lozhkin, Shawn Marshall, Jens Matthiessen, Glen Macdonald, Gifford Miller, Marisa Montoya, Daniel Muhs, Bette Otto-Bliesner, Jonathan Overpeck, Niels Reeh, Hans Petter Sejrup, Robert Spielhagen, Charles Turner, Andrei Velichko, and CAPE-Last Interglacial Project Mem. Last Interglacial Arctic warmth confirms polar amplification of climate change. *QUATERNARY SCIENCE REVIEWS*, 25(13-14):1383–1400, JUL 2006. ISSN 0277-3791. doi: 10.1016/j.quascirev.2006.01.033.

A Arakawa. Computational design for long-term numerical integration of the equations of fluid motion: Two-dimensional incompressible flow .1. (Reprinted from the Journal of Computational Physics, vol 1, pg 119-143, 1966). *JOURNAL OF COMPUTATIONAL PHYSICS*, 135(2):103–114, AUG 1997. ISSN 0021-9991.

A. Armengaud, R.D. Koster, J. Jouzel, and P. Ciais. Deuterium excess in greenland snow: Analysis with simple and complex models. *J. Geophys. Res.*, 103:8947–8953, 1998.

L Augustin, C Barbante, PRF Barnes, JM Barnola, M Bigler, E Castellano, O Cattani, J Chappellaz, D DahlJensen, B Delmonte, G Dreyfus, G Durand, S Falourd, H Fischer, J Fluckiger, ME Hansson, P Huybrechts, R Jugie, SJ Johnsen, J Jouzel, P Kaufmann, J Kipfstuhl, F Lambert, VY Lipenkov, GVC Littot, A Longinelli, R Lorrain, V Maggi, V Masson-Delmotte, H Miller, R Mulvaney, J Oerlemans, H Oerter, G Orombelli, F Parrenin, DA Peel, JR Petit, D Raynaud, C Ritz, U Ruth, J Schwander, U Siegenthaler, R Souchez, B Stauffer, JP Steffensen, B Stenni, TF Stocker, IE Tabacco, R Udisti, RSW van de Wal, M van den Broeke, J Weiss, F Wilhelms, JG Winther, EW Wolff, M Zucchelli, and EPICA Community Members. Eight glacial cycles from an Antarctic ice core. *NATURE*, 429(6992):623–628, JUN 10 2004. ISSN 0028-0836. doi: 10.1038/nature02599.

RC Bales, JR McConnell, E Mosley-Thompson, and G Lamorey. Accumulation map for the Greenland Ice Sheet: 1971-1990. *GEOPHYSICAL RESEARCH LETTERS*, 28(15):2967–2970, AUG 1 2001. ISSN 0094-8276.

A Berger. MILANKOVITCH THEORY AND CLIMATE. *REVIEWS OF GEOPHYSICS*, 26(4):624–657, NOV 1988. ISSN 8755-1209.

AL Berger. LONG-TERM VARIATIONS OF CALORIC INSOLATION RESULTING FROM EARTHS ORBITAL ELEMENTS. *QUATERNARY RESEARCH*, 9(2):139–167, 1978. ISSN 0033-5894.

P. Bergthorsson, B. Döös, S. Fryklund, O. Haug, and R. Lindquist. Routine forecasting with the barotropic model. *Tellus*, 7:274–276, 1955.

Paul Blanchon, Anton Eisenhauer, Jan Fietzke, and Volker Liebetrau. Rapid sea-level rise and reef back-stepping at the close of the last interglacial highstand. *NATURE*, 458(7240):881–U6, APR 16 2009. ISSN 0028-0836. doi: 10.1038/nature07933.

T Blunier and EJ Brook. Timing of millennial-scale climate change in Antarctica and Greenland during the last glacial period. *SCIENCE*, 291(5501): 109–112, JAN 5 2001. ISSN 0036-8075.

Jason E. Box, David H. Bromwich, Bruce A. Veenhuis, Le-Sheng Bai, Julienne C. Stroeve, Jeffrey C. Rogers, Konrad Steffen, T. Haran, and Sheng-Hung Wang. Greenland ice sheet surface mass balance variability (1988-

2004) from calibrated polar MM5 output. *JOURNAL OF CLIMATE*, 19 (12):2783–2800, JUN 15 2006. ISSN 0894-8755.

JE Box and A Rinke. Evaluation of Greenland ice sheet surface climate in the HIRHAM regional climate model using automatic weather station data. *JOURNAL OF CLIMATE*, 16(9):1302–1319, MAY 2003. ISSN 0894-8755.

JE Box, DH Bromwich, and LS Bai. Greenland ice sheet surface mass balance 1991-2000: Application of Polar MM5 mesoscale model and in situ data. *JOURNAL OF GEOPHYSICAL RESEARCH-ATMOSPHERES*, 109(D16), AUG 26 2004. ISSN 0148-0227. doi: 10.1029/2003JD004451.

P. Braconnot, C. Marzin, L. Gregoire, E. Mosquet, and O. Marti. Monsoon response to changes in Earth's orbital parameters: comparisons between simulations of the Eemian and of the Holocene. *CLIMATE OF THE PAST*, 4(4):281–294, 2008. ISSN 1814-9324.

DH Bromwich, JJ Cassano, T Klein, G Heinemann, KM Hines, K Steffen, and JE Box. Mesoscale modeling of katabatic winds over Greenland with the Polar MM5. *MONTHLY WEATHER REVIEW*, 129(9):2290–2309, 2001. ISSN 0027-0644.

Roberto Buizza, Jean-Raymond Bidlot, Nils Wedi, Manuel Fuentes, Mats Hamrud, Graham Holt, and Frederic Vitart. The new ECMWF VAREPS (Variable Resolution Ensemble Prediction System). *QUARTERLY JOURNAL OF THE ROYAL METEOROLOGICAL SOCIETY*, 133(624, Part A):681–695, APR 2007. ISSN 0035-9009. doi: 10.1002/qj.75.

J Cappelen, BV Jørgensen, EV Laursen, LS Stannius, and RS Thomsen. The observed climate of greenland, 1958-99 - with climatological standard normals, 1961-90. Technical Report 00-18, DMI, 2001.

J.G. Charney, Fjörtoft R., and J.v. Neumann. Numerical integration of the barotropic vorticity equation. *Tellus*, 2:237–254, 1950.

et al. Church, J. A. *Changes in Sea Level. , in Climate Change 2001: The Scientific Basis*, chapter Chapter 11. Cambridge University Press, 2001.

H. Craig. Isotopic variations in meteoric waters. *Science*, 133:1702–1703, 1961.

H. Craig and L. I. Gordon. Deuterium and oxygen 18 variations in the ocean and marine atmosphere. In E. Tongiogi, editor, *proc. Stable Isotopes in Oceanographic Studies and Paleotemperatures*, pages 9–130. V. Lishi e F., Pisa, 1965.

J Crank and P Nicolson. A PRACTICAL METHOD FOR NUMERICAL EVALUATION OF SOLUTIONS OF PARTIAL DIFFERENTIAL EQUATIONS OF THE HEAT-CONDUCTION TYPE. *PROCEEDINGS OF THE CAMBRIDGE PHILOSOPHICAL SOCIETY*, 43(1):50–67, 1947.

KM Cuffey and SJ Marshall. Substantial contribution to sea-level rise during the last interglacial from the Greenland ice sheet. *NATURE*, 404(6778): 591–594, APR 6 2000. ISSN 0028-0836.

R Daley and Y Bourassa. Rhomboidal versus triangular spherical harmonie truncation: Some verification statistics. *ATMOSPHERE-OCEAN*, 16((2)): 187–196, 1978.

W. Dansgaard. The abundance of ^{18}o in atmospheric water and water vapor. *Tellus*, 5:461–469, 1953.

W. Dansgaard. Stable isotopes in precipitation. *Tellus*, 16:436–468, 1964.

W. Dansgaard, S. J. Johnsen, J. Möller, and C.C. Langway. Oxygen isotope analysis of an ice core representing a complete vertical profile of a polar ice sheet. In *ISAGE Symposium*, pages 93–94, Hannover, USA, 1968.

H.C. Davies. LATERAL BOUNDARY FORMULATION FOR MULTILEVEL PREDICTION MODELS. *QUARTERLY JOURNAL OF THE ROYAL METEOROLOGICAL SOCIETY*, 102(432):405–418, 1976. ISSN 0035-9009.

A. E. Dessler, Z. Zhang, and P. Yang. Water-vapor climate feedback inferred from climate fluctuations, 2003-2008. *GEOPHYSICAL RESEARCH LETTERS*, 35(20), OCT 23 2008. ISSN 0094-8276. doi: 10.1029/2008GL035333.

B Efron. THE JACKKNIFE, THE BOOTSTRAP AND OTHER RESAMPLING PLANS. *JOURNAL OF THE AMERICAN STATISTICAL ASSOCIATION*, 78(384):987, 1983. ISSN 0162-1459.

X. Fettweis, E. Hanna, H. Gallée, P. Huybrechts, and M. Erpicum. Estimation of the greenland ice sheet surface mass balance for the 20th and 21st centuries. *The Cryosphere*, 2(2):117–129, 2008. ISSN 1994-0416. URL `http://www.the-cryosphere.net/2/117/2008/`.

H Fischer, M Werner, D Wagenbach, M Schwager, T Thorsteinnson, F Wilhelms, J Kipfstuhl, and S Sommer. Little ice age clearly recorded in northern Greenland ice cores. *GEOPHYSICAL RESEARCH LETTERS*, 25(10): 1749–1752, MAY 15 1998. ISSN 0094-8276.

H Fischer, M Wahlen, J Smith, D Mastroianni, and B Deck. Ice core records of atmospheric CO2 around the last three glacial terminations. *SCIENCE*, 283(5408):1712–1714, MAR 12 1999. ISSN 0036-8075.

D Fleitmann, SJ Burns, U Neff, A Mangini, and A Matter. Changing moisture sources over the last 330,000 years in Northern Oman from fluid-inclusion evidence in speleothems. *QUATERNARY RESEARCH*, 60(2): 223–232, SEP 2003. ISSN 0033-5894. doi: 10.1016/S0033-5894(03)00086-3.

A Foldvik, K Aagaard, and T Torresen. ON THE VELOCITY-FIELD OF THE EAST GREENLAND CURRENT. *DEEP-SEA RESEARCH PART A-OCEANOGRAPHIC RESEARCH PAPERS*, 35(8):1335–1354, AUG 1988. ISSN 0198-0149.

Koji Fujita and Osamu Abe. Stable isotopes in daily precipitation at Dome Fuji, East Antarctica. *GEOPHYSICAL RESEARCH LETTERS*, 33(18), SEP 29 2006. ISSN 0094-8276. doi: 10.1029/2006GL026936.

C.T. Gordon and W.F. Stern. A description of the gfdl global spectral model. *Mon. Wea. Rev.*, 110:625–644, 1982.

JM Gregory, P Huybrechts, and SCB Raper. Climatology - Threatened loss of the Greenland ice-sheet. *NATURE*, 428(6983):616, APR 8 2004. ISSN 0028-0836. doi: 10.1038/428616a.

Stefan Hagemann, Holger Goettel, Daniela Jacob, Philip Lorenz, and Erich Roeckner. Improved regional scale processes reflected in projected hydrological changes over large European catchments. *CLIMATE DYNAMICS*, 32(6):767–781, MAY 2009. ISSN 0930-7575. doi: 10.1007/s00382-008-0403-9.

A Hall. The role of surface albedo feedback in climate. *JOURNAL OF CLIMATE*, 17(7):1550–1568, APR 2004. ISSN 0894-8755.

M Herold and G Lohmann. Eemian tropical and subtropical african moisture transport: an isotope modelling study. *Clim. Dyn.*, 2009.

G Hoffmann. *Wasserisotope im allgemeinen Zirkulationsmodell ECHAM.* PhD thesis, Universität Hamburg, 1995.

G Hoffmann and M Heimann. Water isotope modeling in the Asian monsoon region. *QUATERNARY INTERNATIONAL*, 37:115–128, 1997. ISSN 1040-6182.

G Hoffmann, M Werner, and M Heimann. Water isotope module of the ECHAM atmospheric general circulation model: A study on timescales from days to several years. *JOURNAL OF GEOPHYSICAL RESEARCH-ATMOSPHERES*, 103(D14):16871–16896, JUL 27 1998. ISSN 0747-7309.

J.R. Holton. *An Introduction to Dynamic Meteorology*. Academic Press, third edition, 1992.

J. W. Hurrell. An overview of the north atlantic oscillation. In *EGS - AGU - EUG Joint Assembly*, pages 12504–+, April 2003.

IAEA. Isotope hydrology information system. the isohis database. accessible at: http://isohis.iaea.org, 2006.

C Israelson and B Wohlfarth. Timing of the last-interglacial high sea level on the Seychelles Islands, Indian ocean. *QUATERNARY RESEARCH*, 51 (3):306–316, MAY 1999. ISSN 0033-5894.

D Jacob. A note to the simulation of the annual and inter-annual variability of the water budget over the Baltic Sea drainage basin. *METEOROLOGY AND ATMOSPHERIC PHYSICS*, 77(1-4):61–73, 2001. ISSN 0177-7971.

D Jacob and R Podzun. Sensitivity studies with the regional climate model REMO. *METEOROLOGY AND ATMOSPHERIC PHYSICS*, 63(1-2): 119–129, 1997. ISSN 0177-7971.

ABM Jeuken, PC Siegmund, LC Heijboer, J Feichter, and L Bengtsson. On the potential of assimilating meteorological analyses in a global climate model for the purpose of model validation. *JOURNAL OF GEOPHYSICAL RESEARCH-ATMOSPHERES*, 101(D12):16939–16950, JUL 27 1996. ISSN 0148-0227.

S Johnsen and BM Vinther. Stable isotope records from greenland ice core. In *Encyclopedia of Quarternary Sciences*. Elsevier, 2007.

Sigfús J. Johnsen, Henrik B. Clausen, Kurt M. Cuffey, Georg Hoffmann, Jakob Schwander, and Timothy Creyts. Diffusion of stable isotopes in polar firn and ice : the isotope effect in firn diffusion. In *Physics of Ice Core Records*, pages 121–140. Hokkaido University Press, 2000.

S.J. Johnsen. Stable isotope homogenization of polar firn and ice. *Proceedings of a symposium held during the XVI Assembly of the International Union of Geodesy and Geophysics at Grenoble, August/September 1975; Actes du colloque de Grenoble, Août/Septembre 1975*, IAHS-AISH Publ. No. 118: 210–219, 1977.

S.J Johnsen, W. Dansgaard, and J.W.C. White. The origin of arctic precipitation under present and glacial conditions. *Tellus*, 41B:452–468, 1989.

S.J. Johnsen, H.B. Clausen, W. Dansgaard, F. Fuhrer, N. Gundestrup, C.U. Hammer, P. Iversen, J. Jouzel, B. Stauffer, and J.P. Steffensen. Irregular glacial interstadials recorded in a new greenland ice core. *Nature*, 359, 1992.

S.J. Johnsen, D. Dahl-Jensen, N. Gundestrup, J.P. Steffensen, H.B. Clausen, H. Miller, V. Masson-Delmotte, A.E. Sveinbjàrndottir, and J. White. Oxygen isotope and palaeotemperature records from six greenland ice-core stations: Camp century, dye-3, grip, gisp2, renland and northgrip. *J. Quat. Sci.*, 16:299–307, 2001.

S Joussaume and P Braconnot. Sensitivity of paleoclimate simulation results to season definitions. *JOURNAL OF GEOPHYSICAL RESEARCH-ATMOSPHERES*, 102(D2):1943–1956, JAN 27 1997.

S Joussaume, R Sadourny, and J Jouzel. A GENERAL-CIRCULATION MODEL OF WATER ISOTOPE CYCLES IN THE ATMOSPHERE. *NATURE*, 311(5981):24–29, 1984. ISSN 0028-0836.

J Jouzel and RD Koster. A reconsideration of the initial conditions used for stable water isotope models. *JOURNAL OF GEOPHYSICAL RESEARCH-ATMOSPHERES*, 101(D17):22933–22938, OCT 20 1996. ISSN 0148-0227.

J. Jouzel and L. Merlivat. deuterium and oxygen 18 in precipitation: Modeling of the isotopic effects during snow formation. *J. Geophys. Res.*, 89: 11749–11757, 1984.

J. Jouzel, V. Masson-Delmotte, O. Cattani, G. Dreyfus, S. Falourd, G. Hoffmann, B. Minster, J. Nouet, J. M. Barnola, J. Chappellaz, H. Fischer, J. C. Gallet, S. Johnsen, M. Leuenberger, L. Loulergue, D. Luethi, H. Oerter, F. Parrenin, G. Raisbeck, D. Raynaud, A. Schilt, J. Schwander, E. Selmo, R. Souchez, R. Spahni, B. Stauffer, J. P. Steffensen, B. Stenni, T. F.

Stocker, J. L. Tison, M. Werner, and E. W. Wolff. Orbital and Millennial Antarctic Climate Variability over the Past 800,000 Years. *Science*, 317(5839):793–796, 2007. doi: 10.1126/science.1141038. URL `http://www.sciencemag.org/cgi/content/abstract/317/5839/793`.

J Jouzel, GL Russel, RJ Suossu, RD Koster, JWC White, and WS Broecker. SIMULATIONS OF THE HDO AND H2 O-18 ATMOSPHERIC CYCLES USING THE NASA GISS GENERAL-CIRCULATION MODEL - THE SEASONAL CYCLE FOR PRESENT-DAY CONDITIONS. *JOURNAL OF GEOPHYSICAL RESEARCH-ATMOSPHERES*, 92(D12): 14739–14760, DEC 20 1987.

HMH Juang and M Kanamitsu. THE NMC NESTED REGIONAL SPECTRAL MODEL. *MONTHLY WEATHER REVIEW*, 122(1):3–26, JAN 1994. ISSN 0027-0644.

PV Jørgensen and EV Laursen. Dmi monthly climate data collection 1860-2002, denmark, faroe island and greenland. Technical Report 03-26, DMI, 2003.

M Kanamitsu, W Ebisuzaki, J Woollen, SK Yang, JJ Hnilo, M Fiorino, and GL Potter. NCEP-DOE AMIP-II reanalysis (R-2). *BULLETIN OF THE AMERICAN METEOROLOGICAL SOCIETY*, 83(11):1631–1643, NOV 2002. ISSN 0003-0007. doi: 10.1175/BAMS-83-11-1631.

S Kiilsholm, JH Christensen, K Dethloff, and A Rinke. Net accumulation of the Greenland ice sheet: High resolution modeling of climate changes. *GEOPHYSICAL RESEARCH LETTERS*, 30(9), MAY 13 2003. ISSN 0094-8276. doi: 10.1029/2002GL015742.

Peter L. Langen and Vladimir A. Alexeev. Polar amplification as a preferred response in an idealized aquaplanet GCM. *CLIMATE DYNAMICS*, 29(2-3):305–317, AUG 2007. ISSN 0930-7575. doi: 10.1007/s00382-006-0221-x.

E.N. Lorenz. DETERMINISTIC NONPERIODIC FLOW. *JOURNAL OF THE ATMOSPHERIC SCIENCES*, 20(2):130–141, 1963. ISSN 0022-4928.

P Lynch. RICHARDSON BAROTROPIC FORECAST - A REAPPRAISAL. *BULLETIN OF THE AMERICAN METEOROLOGICAL SOCIETY*, 73(1):35–47, JAN 1992. ISSN 0003-0007.

D Majewski. The europa-modell of the deutscher wetterdienst. In *ECMWF Seminar on Numerical methods in atmospheric models*, volume 2, pages 147–191, 1991.

M. Majoube. Oxygen-18 and deuterium fractionation between water and steam. *J. Chim. Phys.*, 10, 1971.

O. Marti, P. Braconnot, J. Bellier, R. Benshila, S. Bony, P. Brock-mann, P. Cadule, A. Caubel, S. Denvil, J. L. Dufresne, L. Fairhead, M. A. Filiberti, M.-A. Foujols, T. Fichefet, P. Friedling-stein, H. Goosse, J. Y. Grandpeix, F. Hourdin, G. Krinner, C. Lévy, G. Madec, I. Musat, N. deNoblet, J. Polcher, and C Talandier. The new ipsl climate system model: Ipsl-cm4. Technical Report 26, Note du Pôle de Modélisation, 2005.

V. Masson-Delmotte, J. Jouzel, A. Landais, M. Stivenard, S.J. Johnsen, J.W.C. White, M. Merner, A. Sveinbjàrndottir, and K. Fuhrer. Grip deuterium excess reveals rapid and orbital-scale changes in greenland moisture origin. *Science*, 309, 2005.

V. Masson-Delmotte, S. Hou, A. Ekaykin, J. Jouzel, A. Aristarain, R. T. Bernardo, D. Bromwich, O. Cattani, M. Delmotte, S. Falourd, M. Frezzotti, H. Gallee, L. Genoni, E. Isaksson, A. Landais, M. M. Helsen, G. Hoffmann, J. Lopez, V. Morgan, H. Motoyama, D. Noone, H. Oerter, J. R. Petit, A. Royer, R. Uemura, G. A. Schmidt, E. Schlosser, J. C. Simoes, E. J. Steig, B. Stenni, M. Stievenard, M. R. van den Broeke, R. S. W. van de Wal, W. J. van de Berg, F. Vimeux, and J. W. C. White. A review of Antarctic surface snow isotopic composition: Observations, atmospheric circulation, and isotopic modeling. *JOURNAL OF CLIMATE*, 21(13): 3359–3387, JUL 2008. ISSN 0894-8755. doi: 10.1175/2007JCLI2139.1.

L. Merlivat. Molecular diffusivities of $h_2^{16}o$, $hd^{16}o$, and $h_2^{18}o$ in gases. *J. Chem. Phys.*, 69:2864–2871, 1978.

L. Merlivat and J. Jouzel. Global climate interpretation of the deuterium-oxygen 18 relationship. *J. Geophys. Res.*, 84:5029–5033, 1979.

Modellbetreuungsgruppe. The echam3 atmospheric general circulation model. Technical Report 6, Deutsches Klimarechenzentrum, 1993.

E Monnin, A Indermuhle, A Dallenbach, J Fluckiger, B Stauffer, TF Stocker, D Raynaud, and JM Barnola. Atmospheric CO2 concentrations over the last glacial termination. *SCIENCE*, 291(5501):112–114, JAN 5 2001. ISSN 0036-8075.

GR North, TL Bell, RF Cahalan, and FJ Moeng. SAMPLING ERRORS IN THE ESTIMATION OF EMPIRICAL ORTHOGONAL FUNCTIONS. *MONTHLY WEATHER REVIEW*, 110(7):699–706, 1982. ISSN 0027-0644.

M Oppenheimer. Global warming and the stability of the West Antarctic Ice Sheet. *NATURE*, 393(6683):325–332, MAY 28 1998. ISSN 0028-0836.

BL Otto-Bliesner, SJ Marsha, JT Overpeck, GH Miller, AX Hu, and CAPE Last Interglacial Project Mem. Simulating arctic climate warmth and icefield retreat in the last interglaciation. *SCIENCE*, 311(5768):1751–1753, MAR 24 2006. ISSN 0036-8075. doi: 10.1126/science.1120808.

J. R. Petit, J. W. C. White, N. W. Young, J. Jouzel, and Y. S. Korotkevich. Deuterium excess in recent antarctic snow. *J. Geophys. Res.*, 96(D3):5113–5122, 1991.

JR Petit, J Jouzel, D Raynaud, NI Barkov, JM Barnola, I Basile, M Bender, J Chappellaz, M Davis, G Delaygue, M Delmotte, VM Kotlyakov, M Legrand, VY Lipenkov, C Lorius, L Pepin, C Ritz, E Saltzman, and M Stievenard. Climate and atmospheric history of the past 420,000 years from the Vostok ice core, Antarctica. *NATURE*, 399(6735):429–436, JUN 3 1999. ISSN 0028-0836.

L.F. Richardson. *Weather Prediction by Numerical Process*. Cambridge University Press, 1922.

E Rignot and SS Jacobs. Rapid bottom melting widespread near Antarctic ice sheet grounding lines. *SCIENCE*, 296(5575):2020–2023, JUN 14 2002. ISSN 0036-8075.

B Rudels, HJ Friedrich, and D Quadfasel. The arctic circumpolar boundary current. *DEEP-SEA RESEARCH PART II-TOPICAL STUDIES IN OCEANOGRAPHY*, 46(6-7):1023–1062, 1999. ISSN 0967-0645.

GA Schmidt, G Hoffmann, DT Shindell, and YY Hu. Modeling atmospheric stable water isotopes and the potential for constraining cloud processes and stratosphere-troposphere water exchange. *JOURNAL OF GEOPHYSICAL RESEARCH-ATMOSPHERES*, 110(D21), NOV 12 2005. ISSN 0148-0227. doi: 10.1029/2005JD005790.

T Semmler. *Der Wasser- und Energiehaushalt der arktischen Atmosphäre*. PhD thesis, Max-Planck-Institut für Meteorologie, 2002.

C.A. Shuman, R.B. Alley, S. Anandakrishnan, J.W.C. White, P.M. Grootes, and C.R. Stearns. Temperature and accumulation at the greenland summit: Comparison of high-resolution isotope profiles and satellite passive microwave brightness temperature trends. *J. Geophys. Res.*, 100:9165–9177, 1995.

J Sjolte. Interpretation of the isotopic composition of the greenland ice cores using simple modeling. Master's thesis, The Niels Bohr Institute, 2005.

VC Slonosky and P Yiou. The North Atlantic Oscillation and its relationship with near surface temperature. *GEOPHYSICAL RESEARCH LETTERS*, 28(5):807–810, MAR 1 2001. ISSN 0094-8276.

H. Sodemann, V. Masson-Delmotte, C. Schwierz, B. M. Vinther, and H. Wernli. Interannual variability of greenland winter precipitation sources: 2. effects of north atlantic oscillation variability on stable isotopes in precipitation. *J. Geophys. Res.*, 113, 2008a.

H. Sodemann, C. Schwierz, and H. Wernli. Interannual variability of greenland winter precipitation sources: Lagrangian moisture diagnostic and north atlantic oscillation influence. *J. Geophys. Res.*, 113, 2008b.

S. Solomon, D. Qin, M. Manning, Z. Chen, M. Marquis, K.B. Averyt, M. Tignor, and H.L. Miller, editors. *Climate Change 2007: The Physical Science Basis. Contribution of Working Group I to the Fourth Assessment Report of the Intergovernmental Panel on Climate Change*. Cambridge University Press, Cambridge, United Kingdom and New York, NY, USA, 2007.

Jorgen Peder Steffensen, Katrine K. Andersen, Matthias Bigler, Henrik B. Clausen, Dorthe Dahl-Jensen, Hubertus Fischer, Kumiko Goto-Azuma, Margareta Hansson, Sigfus J. Johnsen, Jean Jouzel, Valerie Masson-Delmotte, Trevor Popp, Sune O. Rasmussen, Regine Rothlisberger, Urs Ruth, Bernhard Stauffer, Marie-Louise Siggaard-Andersen, Arny E. Sveinbjornsdottir, Anders Svensson, and James W. C. White. High-Resolution Greenland Ice Core Data Show Abrupt Climate Change Happens in Few Years. *Science*, 321(5889):680–684, 2008. doi: 10.1126/science.1157707. URL `http://www.sciencemag.org/cgi/content/abstract/321/5889/680`.

CH Stirling, TM Esat, K Lambeck, and MT McCulloch. Timing and duration of the Last Interglacial: evidence for a restricted interval of widespread coral reef growth. *EARTH AND PLANETARY SCIENCE LETTERS*, 160(3-4):745–762, AUG 1998. ISSN 0012-821X.

H. von Storch and A. Navarra, editors. *Analysis of climate variability: Applications of statistical techniques*. Springer-Verlag, New York, NY (United States), 1995.

H von Storch, H Langenberg, and F Feser. A spectral nudging technique for dynamical downscaling purposes. *MONTHLY WEATHER REVIEW*, 128 (10):3664–3673, OCT 2000. ISSN 0027-0644.

Christophe Sturm, Georg Hoffmann, and Baerbel Langmann. Simulation of the stable water isotopes in precipitation over South America: Comparing regional to global circulation models. *JOURNAL OF CLIMATE*, 20(15): 3730–3750, AUG 1 2007. ISSN 0894-8755.

K Sturm, G Hoffmann, B Langmann, and W Stichler. Simulation of delta O-18 in precipitation by the regional circulation model REMOiso. *HYDROLOGICAL PROCESSES*, 19(17):3425–3444, NOV 15 2005. ISSN 0885-6087. doi: 10.1002/hyp.5979.

Kristof Sturm. *Regional atmospheric modelling of the stable water isotope cycle*. PhD thesis, l'Université Joseph Fourier, 2005.

D. Swingedouw, P. Braconnot, P. Delecluse, E. Guilyardi, and O. Marti. The impact of global freshwater forcing on the thermohaline circulation: adjustment of North Atlantic convection sites in a CGCM. *CLIMATE DYNAMICS*, 28(2-3):291–305, FEB 2007. ISSN 0930-7575. doi: 10.1007/s00382-006-0171-3.

JR Taylor. *An Introduction to Error Analysis*. University Science Books, 1997.

M Tjernstrom, M Zagar, G Svensson, JJ Cassano, S Pfeifer, A Rinke, K Wyser, K Dethloff, C Jones, T Semmler, and M Shaw. Modelling the arctic boundary layer: An evaluation of six arcmip regional-scale models using data from the Sheba project. *BOUNDARY-LAYER METEOROLOGY*, 117(2):337–381, NOV 2005. ISSN 0006-8314. doi: 10.1007/s10546-004-7954-z.

SM Uppala, PW Kallberg, AJ Simmons, U Andrae, VD Bechtold, M Fiorino, JK Gibson, J Haseler, A Hernandez, GA Kelly, X Li, K Onogi, S Saarinen, N Sokka, RP Allan, E Andersson, K Arpe, MA Balmaseda, ACM Beljaars, L Van De Berg, J Bidlot, N Bormann, S Caires, F Chevallier, A Dethof, M Dragosavac, M Fisher, M Fuentes, S Hagemann, E Holm, BJ Hoskins, L Isaksen, PAEM Janssen, R Jenne, AP McNally, JF Mahfouf, JJ Morcrette, NA Rayner, RW Saunders, P Simon, A Sterl, KE Trenberth, A Untch, D Vasiljevic, P Viterbo, and J Woollen. The ERA-40 re-analysis. *QUARTERLY JOURNAL OF THE ROYAL METEOROLOGICAL SOCIETY*, 131(612, Part B):2961–3012, OCT 2005. ISSN 0035-9009. doi: 10.1256/qj.04.176.

MK van Aalst, MMP van den Broek, A Bregman, C Bruhl, B Steil, GC Toon, S Garcelon, GM Hansford, RL Jones, TD Gardiner, GJ Roelofs, J Lelieveld, and PJ Crutzen. Trace gas transport in the 1999/2000 Arctic winter: comparison of nudged GCM runs with observations. *ATMOSPHERIC CHEMISTRY AND PHYSICS*, 4:81–93, JAN 23 2004. ISSN 1680-7324.

MR van den Broeke and NPM van Lipzig. Factors controlling the near-surface wind field in Antarctica. *MONTHLY WEATHER REVIEW*, 131 (4):733–743, APR 2003. ISSN 0027-0644.

B. M. Vinther, P. D. Jones, K. R. Briffa, H. B. Clausen, K. K. Andersen, D. Dahl-Jensen, and S. J. Johnsen. Climatic signals in multiple highly resolved stable isotope records from greenland. *Quat. Sci. Rev.*, 2008. Submitted.

B. M. Vinther, K. K. Andersen, P. D. Jones, K. R. Briffa, and J. Cappelen. Extending Greenland temperature records into the late eighteenth century. *JOURNAL OF GEOPHYSICAL RESEARCH-ATMOSPHERES*, 111(D11), JUN 6 2006. ISSN 0148-0227. doi: 10.1029/2005JD006810.

B. M. Vinther, S. L. Buchardt, H. B. Clausen, D. Dahl-Jensen, S. J. Johnsen, D. A. Fisher, R. M. Koerner, D. Raynaud, V. Lipenkov, K. K. Andersen, T. Blunier, S. O. Rasmussen, J. P. Steffensen, and A. M. Svensson. Holocene thinning of the Greenland ice sheet. *NATURE*, 461(7262):385–388, SEP 17 2009. ISSN 0028-0836. doi: 10.1038/nature08355.

BM Vinther, SJ Johnsen, KK Andersen, HB Clausen, and AW Hansen. NAO signal recorded in the stable isotopes of Greenland ice cores. *GEOPHYSICAL RESEARCH LETTERS*, 30(7), APR 8 2003. ISSN 0094-8276. doi: 10.1029/2002GL016193.

KM Waldron, J Paegle, and JD Horel. Sensitivity of a spectrally filtered and nudged limited-area model to outer model options. *MONTHLY WEATHER REVIEW*, 124(3):529–547, MAR 1996. ISSN 0027-0644.

G Walker. World weather. *MONTHLY WEATHER REVIEW*, 56(5), 1928.

John E. Walsh, William L. Chapman, Vladimir Romanovsky, Jens H. Christensen, and Martin Stendel. Global Climate Model Performance over Alaska and Greenland. *JOURNAL OF CLIMATE*, 21(23):6156–6174, DEC 1 2008. ISSN 0894-8755. doi: 10.1175/2008JCLI2163.1.

Yongjin Wang, Hai Cheng, R. Lawrence Edwards, Xinggong Kong, Xiaohua Shao, Shitao Chen, Jiangyin Wu, Xiouyang Jiang, Xianfeng Wang, and Zhisheng An. Millennial- and orbital-scale changes in the East Asian monsoon over the past 224,000 years. *NATURE*, 451(7182):1090–1093, FEB 28 2008. ISSN 0028-0836. doi: 10.1038/nature06692.

M Werner and M Heimann. Modeling interannual variability of water isotopes in Greenland and Antarctica. *JOURNAL OF GEOPHYSICAL RESEARCH-ATMOSPHERES*, 107(D1-D2), JAN 2002. ISSN 0747-7309. doi: 10.1029/2001JD900253.

M. Werner, U. Mikolajewics, M. Heimann, and G. Hoffmann. Borehole versus isotope temperatures on greenland: Seasonality does matter. *Geophys. Res. Lett.*, 27:723–726, 2000.

M Werner, M Heimann, and G Hoffmann. Isotopic composition and origin of polar precipitation in present and glacial climate simulations. *TELLUS SERIES B-CHEMICAL AND PHYSICAL METEOROLOGY*, 53(1):53–71, FEB 2001. ISSN 0280-6509.

M Wild, L Dumenil, and JP Schulz. Regional climate simulation with a high resolution GCM: Surface hydrology. *CLIMATE DYNAMICS*, 12(11):755–774, OCT 1996. ISSN 0930-7575.

Eske Willerslev, Enrico Cappellini, Wouter Boomsma, Rasmus Nielsen, Martin B. Hebsgaard, Tina B. Brand, Michael Hofreiter, Michael Bunce, Hendrik N. Poinar, Dorthe Dahl-Jensen, Sigfus Johnsen, Jorgen Peder Steffensen, Ole Bennike, Jean-Luc Schwenninger, Roger Nathan, Simon Armitage, Cees-Jan de Hoog, Vasily Alfimov, Marcus Christl, Juerg Beer, Raimund Muscheler, Joel Barker, Martin Sharp, Kirsty E. H. Penkman, James Haile, Pierre Taberlet, M. Thomas P. Gilbert, Antonella Casoli, Elisa Campani, and Matthew J. Collins. Ancient biomolecules from deep ice cores reveal a forested Southern Greenland. *SCIENCE*, 317(5834):111–114, JUL 6 2007. ISSN 0036-8075. doi: 10.1126/science.1141758.

W. H. Zagwijn. An analysis of eemian climate in western and central europe. *Quaternary Science Reviews*, 15(5-6):451 – 469, 1996. ISSN 0277-3791. doi: DOI: 10.1016/0277-3791(96)00011-X. URL `http://www.sciencedirect.com/science/article/B6VBC-3VWK6MV-7/2/b840f1eeede4`

U. Zimmermann, D. Ehhalt, and K.O. Muennich. Soil–water movement and evapotranspiration: changes in the isotopic composition of the water. In

Isotopes in Hydrology, pages 567–85. Vienna, International Atomic Energy Agency, 1967.